TECHNICAL UNIVERSITY BERLIN
FACULTY II: MATHEMATICS AND SCIENCE
INSTITUTE OF SOLID STATE PHYSICS

Diploma Thesis

OPTICAL SPECTROSCOPY OF DEFECTS AND IMPURITIES IN ZNO

by:
Markus Raphael Wagner
matriculation number: 194415

supervisors:
Priv. Doz. Dr. A. Hoffmann
Prof. Dr. I. Broser

Berlin, 18th of August 2005

Contents

List of Figures

Chapter 1

Introduction

ZnO is a highly promising material for a wide variety of next-generation applications due to its unique properties. Although the material system has been studied since about 1940, there is now considerable renewed interest to completely understand the electrical and optical properties of ZnO. As a wide gap semiconductor, ZnO is an ideal candidate for optoelectronic devices such as blue to UV light emitting diodes (LEDs), laser diodes (LDs) and white light emitters by phosphors excitation with important applications in high density data storage systems and solid-state lighting [1–4]. The transparency to visible light provides the opportunity to fabricate transparent electronics, UV opto-electronics and integrated sensors from the same material system and makes ZnO an excellent choice for transparent front electrodes in solar cells and displays.

The fabrication of heterostructures is another driving force for research on ZnO. The lattice constant of ZnO matches InGaN at an In compensation of 22% [5] and the bandgap of ZnO can be tuned by divalent substitution on the cation site. Cd substition reduces the bandgap, alloying with Mg significantly increases the bandgap while still maintaining the wurtzite structure of ZnO [6]. In addition, transparent thin film field effect transistors could exhibit enormous potential on the high power, high frequency electronics market [7,8]. The strong resistance to radiation also makes ZnO particularly promising for electronic devices in strong radiation environments, such as satellites and space probes [9–11]. Relative to the III-V wide gap material GaN, ZnO has advantages because of its availability in bulk single-crystal form and its larger exciton binding energy of 60 meV [12] compared to 25 meV [13] in GaN.

Furthermore, the manipulation of spin in semiconductors (spintronics) offers the intriguing opportunity to create an entire new class of electronic devices by controlling the injection, transfer and detection of the particle spin, rather than the flow of charge as presently used in conventional electronics. Possible applications for spintronic devices are spin transistor with very low power consumption, fast permanent semiconductor memory, ultra high data storage systems and quantum computing. Theoretical predictions suggest that room-temperature ferromagnetism should be possible in ZnO by doping with transition metals [14, 15] and the first experimental results with n-type transition metal doped ZnO are available [16–18].

1.1 Motivation

1.1.1 p-Conductivity: Acceptors in ZnO

The main obstacle for the commercialization of ZnO based semiconductor devices is the very poor carrier density in p-type material. ZnO has an asymmetric doping limitation, it can be easily doped n-type [19], but is difficult to dope p-type. Similar difficulties in achieving bipolar (n-type and p-type) doping is also observed in other wide bandgap semiconductors, such as ZnSe, ZnTe and GaN [19–22]. Nominally undoped ZnO is usually n-type due to zinc interstitials, oxygen vacancies or hydrogen impurities and the n-conductivity can be easily increased further by doping with Al, Ga or In. Consequently, there is significant resistance to the formation of shallow acceptor levels. Several deep acceptors, introduced by copper, lithium, silver and zinc vacancies are known, but do not noticeably contribute to hole conduction. It appears that group V elements like N, P, and As, incorporated on the oxygen lattice site, may act as a shallow acceptor and could lead to p-conductivity. Nevertheless, efficient acceptor compensation mechanisms, high acceptor ionization energies and low solubility thresholds have led to hole concentrations, that are - even in latest high-quality material - far from being sufficient for opto-electronics. In addition, the impact of dopants and residual p-type impurities on the p-type carrier concentration is not completely understood.

1.1.2 Spintronics: Ferromagnetism in ZnO

Several difficulties need to be solved before practical spintronics devices can be developed. Theoretical calculations, based on local density approximation, predict that ferromagnetic ordering in ZnO should occur by doping with the 3d elements V, Cr, Fe, Co and Ni as well as Mn when it is co-doped with Sn [15]. A convergent picture of the fundamental description of ferromagnetism in semiconductors however has not yet emerged. Following the model by Dietl *et. al* [14], the critical Curie temperature T_c is a function of the atomic mass of the constituent elements and the concentration of magnetic dopants as well as the carrier type and carrier density. While experimental results in GaN seem to support these predictions, only few reliable reports for ZnO are available. Ferromagnetic behavior in n-type ZnO has been observed for Ni [16] and Mn doped samples [17] with T_c equal to 2 K and 45 K, respectively. According to Dietl *et. al* [23] a higher T_c should be possible for p-type material. Therefore, the challenge is not only to select the optimal transition metal, concentration and growing conditions in order to maximize the Curie temperature, but also to fabricate high quality p-type material with sufficient carrier concentrations and good optical properties for the fabrication of highly integrated spin- and optoelectronic devices.

1.2 Objective

The general aim of this thesis is to extend the understanding of two key issues in the current research progress of ZnO. These are in particular acceptors in p-type material which contribute to the hole conductivity due to their relatively shallow impurity states, and the influence of deep level impurities introduced by transition metal doping in regard to spintronic applications. For the realization of ZnO based optoelectronic and spintronic devices and the improvement of material quality, it is imperative to identify the chemical origin of shallow and deep impurities, to understand their effect on carrier concentrations and compensation mechanisms and to determine their influence on the optical, magnetic and structural properties of ZnO. In order to address these questions, several methods and techniques, that are described in detail in the specific sections, are applied. The outcome of this work provides new insight into acceptor related impurity centers and may therefore deliver useful information for the production of future high-quality p-conductive material.

1.3 Thesis Structure

Following the general introduction above, the second chapter will present an overview of the relevant properties of ZnO with regard to this thesis, including the characterization of point defects, shallow and deep impurities as well as selected electronic properties. The basics of the experimental techniques, particularly those which are relevant for the interpretation and discussion of the acquired data, such as excitons and the influence of external magnetic field on wurtzite semiconductors, are elucidated in chapter 3. The different types of samples (single crystals, and MOCVD and MSD grown samples), which are investigated in this thesis are presented in chapter 4, together with their individual growing and annealing specifications. Subsequently, chapter 5 describes the experimental techniques and set-ups applied for detailed investigations of the specimens. The presentation of the results and their discussion is dedicated to the following two chapters. The influence of doping on the MOCVD grown and single crystal specimens with designated shallow acceptors is analyzed by magnetic field studies of bound excitons and presented in chapter 6. In addition, the optical and structural properties of transition metal doped ZnO films, grown by RF magnetron sputtering, are discussed in chapter 7. Finally, the results are summarized in chapter 8.

Chapter 2

Characteristics of the Material System ZnO

2.1 Introduction

This chapter provides a condensed description of basic properties of ZnO that are relevant for the discussion of the results, presented within this thesis. The first section summarizes the most important fundamental facts of ZnO followed by a section about the formation and influence of point defects and impurities in ZnO. Within this context, doping and (self-)compensation mechanisms are discussed. The last section in this chapter addresses electronic properties such as the valence-band-ordering and optical transitions from the symmetry perspective, as well as the influence of internal strain. More detailed and comprehensive reviews can be found for example in the following references [24, 25].

2.2 Basic Properties

ZnO is a direct II-VI semiconductor, that crystallizes in the wurtzite structure with lattice constants at 300 K of $a = 3.25$ Å and $c = 5.21$ Å. The energy gap at room temperature is $E_g = 3.37$ eV [26] and the free exciton binding energy equals 60 meV [27, 28]. The Zn atoms are tetrahedrally coordinated to four O atoms and the Zn d-electrons hybridize with O p-electrons. At low temperatures, photoluminescence reveals the bound exciton emissions (chapter 3.2) as the most intense radiative channel with numerous excitonic recombinations (table 3.1), whereas at high temperatures the free exciton emission dominates the spectra.

In addition, ZnO exhibits a significant green luminescence, centered around 2.45 eV. Several candidates for the luminescence band have been suggested. Although a contribution of transitions associated with different luminescence centers can not be excluded, at least one green luminescence band in ZnO could be attributed to deep copper acceptors [29] and is discussed in chapter 2.3.6. Other publications suggest a relation of green emissions bands to different transitions involving intrinsic defects, such as ionized Zn interstitial-vacancy complexes, oxygen vacancies or interstitials, and antisites [30–33].

2.3 Defects and Impurities

Defects in semiconductors can have a significant impact on the optical, magnetic, and electronic properties of crystals. The quantity of defects to modify the properties of semiconductors is often smaller than one defect atom per million host atoms. The control of defect incorporation and a complete understanding of their influence and formation is crucial to fabricate high quality material. By intentional introduction of defects during or after growth (doping) as well as due to residual defects, additional states that work as carrier traps at energies within the band gap are induced. The solubility of dopants, and therefore the equilibrium concentration of point defects and impurities, depends on the formation energy of the defects containing the dopants [34]. This concentration is described by

$$c = N_{Sites} exp\left[-\frac{E_f}{k_B T}\right] \tag{2.1}$$

where N_{Sites} is the number of possible lattice sites for the impurity and E_f the formation energy that depends on the chemical potentials of the host elements (Zn, O) and the dopant element. For several native defects in ZnO, the formation energy as a function of the Fermi level is displayed in Fig. 2.1.

2.3.1 Classification of Defects

Defects, in general, can be divided into three categories: point defects, line defects and defect complexes. Point defects and defect complexes, play the dominant role in altering the material properties, while line defects have only minor influence on the optical and electrical behavior of semiconductors. Impurity atoms that are introduced into the lattice can produce different types of point defects. These are interstitials, vacancies, antisites, substitutionals, and Frenkel defect pairs. Since they are of crucial importance, their definition and notation is shortly listed below:

- Interstitials: The impurity atom A occupies a position in between the usual lattice sites. Interstitials are denoted by $\mathrm{A_i}$ (i.e. $\mathrm{Zn_i}$, $\mathrm{O_i}$)
- Vacancies: A missing atom A in the lattice results in a vacancy and deprives the crystal of one electron per broken bond. Vacancies are denoted by $\mathrm{V_A}$ (i.e. $\mathrm{V_{Zn}}$, $\mathrm{V_O}$)

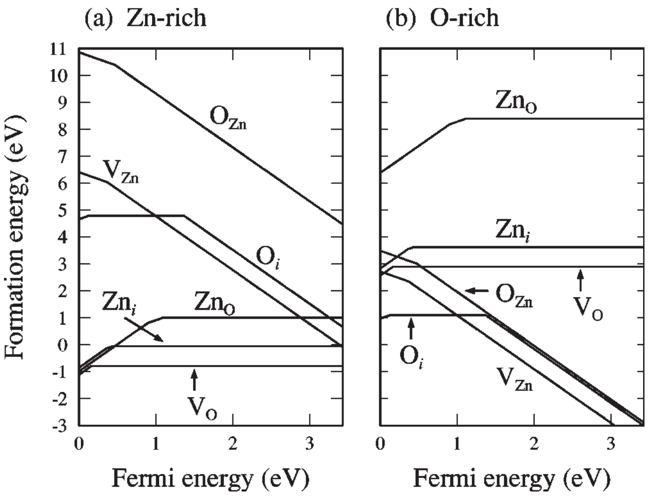

Figure 2.1: Formation energy as a function of the Fermi energy for common intrinsic defects in ZnO for (a) Zn- and (b) O-rich conditions. The zero level of the abscissa refers to the top of the valence band. Taken from Lee *et. al* [35].

- Substitutionals: One of the constituent lattice atoms A is replaced by an impurity atom C. If the impurity atom provides less electrons than the atom it replaces, it will form an acceptor, otherwise a donor. Substitutionals are denoted by $\mathrm{C_A}$ (i.e. $\mathrm{N_O}$, $\mathrm{Ga_{Zn}}$)

- Antisites: A host atom A of one type occupies the lattice site of another host atom B. Antisites are denoted by $\mathrm{A_B}$ (i.e. $\mathrm{Zn_O}$, $\mathrm{O_{Zn}}$)

- Frenkel defect pair: The host atom A is displaced from a lattice site to a nearby interstitial site forming a complex. The defect pair is denoted by $\mathrm{V_A - I_A}$ (i.e. $\mathrm{V_{Zn} - I_{Zn}}$, $\mathrm{V_{Li} - I_{Li}}$)

Both, intrinsic and extrinsic impurities form defect levels that may act as a donor or an acceptor and therefore determine if the material becomes n-type or p-type, respectively. Of particular interest in this context are shallow impurities (chapter 2.3.2) with small activation energies that provide sufficient carrier concentrations at typical device operation temperatures. Deep level impurities on the other hand, play an important role in diluted magnetic semiconductors and their understanding is crucial in order to achieve room temperature ferromagnetism. They will be discussed in chapter 2.3.5.

atom	atomic number	electr. configuration	valence	ionic radius (Å)	acceptor level
Zn	30	[Ar].3d^{10}.4s^2	2+	0.60	
Li	3	[He].2s^1	1+	0.59	0.09 eV
Na	11	[Ne].3s^1	1+	0.99	0.17 eV
K	19	[Ar].4s^1	1+	1.37	0.32 eV
O	8	[He].2s^2.2p^4	2-	1.38	
N	7	[He].2s^2.2p^3	3-	1.46	0.40 eV
P	15	[Ne].3s^2.3p^3	3-	2.12	0.93 eV
As	33	[Ar].3d^{10}.4s^2.4p^3	3-	2.22	1.15 eV

Table 2.1: Electronic configuration, valence and ionic radii of candidate shallow dopant atoms [43]. The acceptor level energy is given relative to the valence-band maximum according to the calculations of Park *et. al* [36].

2.3.2 Shallow Impurities

Impurities that can be calculated within the framework of the effective mass approximation are called shallow. These impurities can strongly contribute to n-type or p-type conductivity. In order to fabricate p-conductive ZnO, the formation of shallow acceptor states is required but proved to be difficult. Possible reasons are a low dopant solubility, which limits the amount of extrinsic carriers that can be introduced, effective acceptor compensation mechanism, and the formation of deep level traps. The solubility for dopants with a large mismatch of the ionic radii (table 2.1) compared to the atoms of the host crystal should be limited, thus leading to a lower extrinsic carrier concentration. In addition, for elements with large ionic radii like P and As substituted on the O lattice site, theoretically only deep acceptors would be expected [36]. Nevertheless, p-type doping with the formation of shallow acceptor levels have been reported for heavier group-V elements [37–42]. The most promising dopants for p-type ZnO are group-I elements substituted for Zn and group-V elements substituted for O, which will be discussed in detail.

2.3.3 Group I Elements

Group-I elements like hydrogen, lithium, and sodium, incorporated on a Zn site provide only one instead of two valence electrons and could therefore serve as an acceptor with one hole in the valence band. However, light elements are very mobile and may also occupy interstitial lattice sites, providing one additional electron to the conduction band. Hence, they are likely to act as a donor and efficiently self compensate the introduced acceptor state.

Hydrogen is a known contaminant in many semiconductors [44] and plays a substantial role in as-grown ZnO [45–49]. While molecular hydrogen (H_2) has virtually no effect on the optical and electrical properties of the crystal, hydrogen in its atomic form (H^+, H^0, H^-) can compensate shallow and deep defects, induce complexes and shift positions of energy levels [50]. On the other hand, hydrogen can also passivate acceptors [45, 51] and thus could prove helpful in achieving higher p-type carrier densities, since acceptor passivation would prevent self compensation during growth and subsequent annealing will remove the H from the lattice, thus activating the acceptors.

Based on first-principles calculations, Van de Walle *et al.* [45] suggested, that hydrogen in ZnO may exclusively occur in the positive charge state and therefore always act as donor, unlike in other semiconductors, where H usually assumes a charge state that counteracts the prevailing conductivity. The main reason for this behavior is the large strength of the $O - H$ bond, which drives the formation energy of H^+ down. This energy is low enough to allow for a large solubility of hydrogen and becomes even lower for Fermi-level positions lower in the band gap as in p-type material. Acceptor compensation by hydrogen donors is thus an important concern for growth and annealing when attempting p-doping of ZnO. Experimental data supports the importance of hydrogen interstitials acting as shallow donors [46, 47]. Electron paramagnetic resonance (EPR) measurements by Hofmann *et al.* [47] exhibited two donor resonances, with one of the two related to interstitial hydrogen. However, the persistence of n-conductivity after annealing of n-type ZnO samples above 600°C, for which hydrogen is found to have been removed [52] supports the assignment that hydrogen is not the dominant shallow donor [49].

Different experimental results concerning the possibility of lithium substituted for zinc (Li_{Zn}) leading to an acceptor state in p-conductive material were reported. EPR [53] and ODMR [24] data indicate that Li_{Zn} can indeed act as an acceptor and PL studies of donor-acceptor pair luminescence in Li-doped ZnO suggest the presence of an acceptor level around 165 meV above the valence band [54]. However, recent experimental investigations of the g-values associated with the Li-center indicate localized states, consistent with deep levels lying at least 500 meV above the valence band [24]. Theoretical calculations by Wardle *et al.* [55] led to the conclusion, that the experimentally observed deep levels most likely do not arise from isolated Li_{Zn}, but rather originate from $Li_{Zn} - O_i$ or $Li_{Zn} - V_{Zn}$ complexes and that Li_{Zn} is less stable than Li_i for the majority of conditions.

2.3.4 Group V Elements

Doping with group-V elements may be the most promising approach to achieving p-conductivity, although theoretical calculations predict shallower acceptor levels

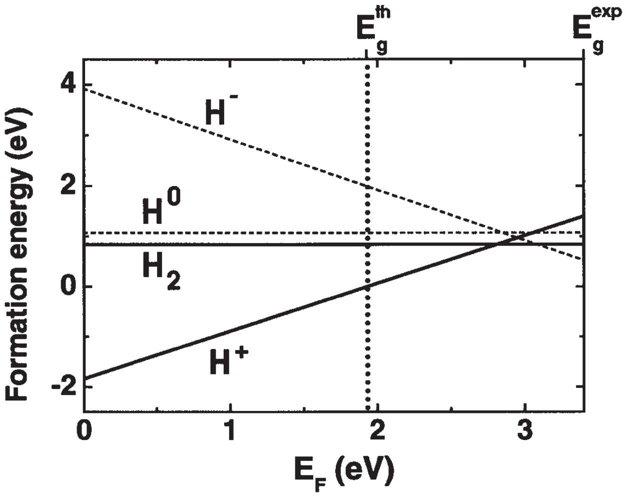

Figure 2.2: Formation energy of interstitial hydrogen in ZnO as a function of Fermi level. Taken from Walle [45].

for group-I species (table 2.1). Nevertheless, there are several reports on p-type ZnO by doping with nitrogen [51, 56–63], phosphorus [37, 38] and arsenic [39–42] in the literature. Caution should however be exercised, since many of the samples suffer from reproducibility issues or questionably high values for Hall mobility or hole concentration were reported.

Nitrogen has long been theoretically considered as a possible dopant for p-type ZnO [64]. Furthermore, the substitution for oxygen (N_O) appears to be a natural choice for an acceptor dopant, since it has about the same ionic radius as that of O (table 2.1). The successful substitution of N for O could be confirmed in ZnO lattice by EPR measurements [65, 66] and secondary ion mass spectroscopy (SIMS) revealed a nitrogen concentration to a level of more than 10^{19} cm^{-3} [60].

Yan *et al.* [67] showed that there is a unique and unusual opportunity when nitrogen is doped into ZnO, because of the availability of four different gases (N_2, NO, NO_2, N_2O) which can be used as a dopant source. Theoretical calculations for the use of NO or NO_2 revealed a negative formation energy for N_O in Zn-rich conditions, indicating that NO and NO_2 molecules can be incorporated spontaneously to form N_O defects, while the formation of nitrogen substitutes from N_2 and N_2O gases is suppressed, since an energy supplement is required to break the molecular N-N bonds. Therefore, the formation of nitrogen acceptor states in ZnO due to N_O defects should be quiet effective.

However, investigations of the compensation mechanism for N acceptors in ZnO through first-principles pseudopotential calculations demonstrated that for low N concentrations, nitrogen acceptors are mainly compensated by oxygen vacancies (V_O), while nitrogen acceptor - zinc antisite complexes ($N_O - Zn_O$) become the major compensation as the N concentration increases [67]. The atomic structures for these complexes in the ZnO lattice is displayed in Fig. 2.3.

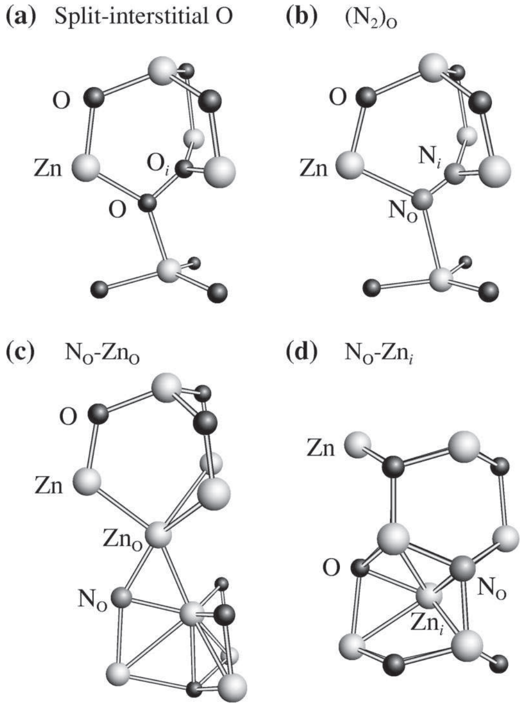

Figure 2.3: Atomic structures of the (a) split-interstitial-O_i complex, (b) N_2 at an O-site, (c) $(N_O - Zn_O)$-complex, (d) $(N_O - Zn_i)$-complex. Taken from Lee *et al.* [35].

Experimental studies have shown that N_O acts as an acceptor with a binding energy of about 165-175 meV [68–70] and leads to a PL emission peak at 3.359 meV within an accuracy of 1 meV. Thonke *et al.* [71] and Zeuner *et al.* [68] assigned an observed peak at 3.232 eV in the ZnO luminescence spectra to a DAP (chapter 3.3), with N_O being the acceptor participating in the DAP transition.

Phosphorus and arsenic as group-V elements have similar electron configurations as nitrogen and thus are also promising candidates for p-type ZnO. However, their larger ionic radius may give rise to new obstacles, that also apply for heavier group-I elements like sodium and potassium. Calculations by Park *et al.* [36] showed that P and As substituted for O with their rather large size mismatch and hence larger nearest-neighbor bond lengths of 2.18 Å for Zn-P and 2.23 Å for Zn-As compared to the typical 1.93 Å for Zn-O will induce large lattice strains. This increases the impurity formation energy and makes the formation of other compensating defects such as vacancies around the impurity easier. In order to avoid the build-up of strong local strains near the oxygen site, P and As are likely to form P_{Zn}^{3+} and As_{Zn}^{3+} antisites, which exhibit a donor-like behavior and provide another mechanism for compensating acceptors.

On the other hand, the predicted acceptor level energies for large size-mismatched impurities (table 2.1) strongly disagree with reported experimental values. According to a recently suggested model of Limpijumnung *et al.* [72] this disagreement can be overcome, if As does not substitute for O but rather forms a $As_{Zn} - 2V_{Zn}$ complex. The As core occupies a Zn antisite, spontaneously inducing two Zn vacancies. The resulting complex is an acceptor with both, a low formation energy of 1.59 eV and a low acceptor level energy of 150 meV. This is in reasonable agreement with the reported As acceptor level of 120 meV [40] and 180 meV, respectively [41].

Despite the different theoretical models, promising results for P and As doping have been reported [37–42]. Nevertheless, the assignment of PL emission peaks like DAP (chapter 3.3) and e-A transitions (chapter 3.4) to specific acceptors and their chemical identity is still missing or needs to be verified.

2.3.5 Deep Level Impurities

All impurity levels that cannot be treated within the framework of the effective mass approximation are considered as deep level impurities. Many impurities in ZnO form deep levels and contradict the attempts to achieve p-conductivity, since the deep acceptor states do not contribute holes to the valence band. In addition, deep levels often act as carrier traps, leading to new radiative or non-radiative transitions. The presence of impurity related non-radiative transitions that are not detectable with photoluminescence spectroscopy might be indicated by a smaller transition probability of the original channels, which leads to a reduced PL intensity. However, transmission spectroscopy is a more reliable indicator for the existence of deep level impurities, since not only the radiative, but also non-radiative transitions can be detected by absorption lines.

The identification of deep level impurities is facilitated by a large variety of characteristic internal transitions, which are enabled by the splitting of the energy levels of the impurity atom. This splitting is caused by the electrical field of the nearest neighbors (Stark effect), and the reduced crystal symmetry, from the perspective of the impurity atom, due to the two atomic basis and the trigonal crystal field. These effects lead to the relaxation of optical selection rules and thus to the occurrence of additional transitions.

On the other hand, deep level impurities play a crucial role in diluted magnetic semiconductors. All 3d transition metals that were predicted to introduce ferromagnetic behavior in ZnO, occupy deep energy levels within the band gap. Although the energy levels for the different transition metals are well known in ZnO from absorption experiments, the understanding of the influence of deep level impurities on ferromagnetism in semiconductors in still incomplete.

2.3.6 The Green Luminescence of Copper in ZnO

The emission spectra of ZnO crystals in the visible range is dominated by a broad luminescence band between 2.85 eV (435 nm) and 2.10 eV (580 nm) with a maximum around 2.45 eV (505 nm). This green luminescence was first reported by Ewles in 1938 [73]. Solbrig [74] and Dingle [29] were able to observe the zero-phonon line of this luminescence at 2.86 eV. High resolution PL revealed the presence of a doublet with a distance of 110 μeV and an intensity ratio of 2.25. This value is in excellent agreement with the nuclear isotope ration of ^{63}Cu/^{65}Cu and therefore allowed the identification of copper as luminescence center [29]. According to the model of Dingle, the green luminescence can be explained as radiative recombination of an excited hydrogen like $(\mathrm{Cu}^{+}, \mathrm{h})$ complex into the Cu^{2+} ground state.

Investigation of highly doped ZnO:Cu single crystals by Broser *et. al* [75] revealed the existence of three zero phonon lines in the excitation spectrum (α, β, γ) that exhibited a strong polarized anisotropic Zeeman splitting in external magnetic fields and indicated a splitting of the excited $\mathrm{Cu}^{+}, \mathrm{h}$ complex. Dean and Robbins [76, 77] explained the appearance of these three lines by the splitting of the valence band into the A, B, and C sub-bands (chapter 2.4.3). In addition, an absorption in the infrared spectral range that was first observed by Pappalardo and Dietz in CdS [78] and Weakliem in ZnO [79] could also be attributed to the Cu^{2+} center and showed the same double line structure with an intensity ratio matching those of the ^{63}Cu and ^{65}Cu isotopes [80].

In ZnO crystals, substitutional copper in the $3d^9$ Cu^{2+} state is incorporated on a Zn^{2+} lattice site as an isoelectric impurity with a low formation energy. The good agreement of the atomic masses and ionic radii of the Cu^{2+} ions with the Zn^{2+} ions reduces the probability of inducing mechanical defects by copper substitution in the vicinity of the impurity. In addition, copper atoms can be created by radioactive decay of small amounts of unstable zinc isotopes and trace amounts of copper are present in all ZnO specimens. Therefore, it can be concluded that although green luminescence bands have been reported as results of intrinsic defects [30–33], the common presence of copper in nominally undoped ZnO always makes Cu a possible candidate for the green luminescence. However, the green emission band can only doubtlessly be attributed to copper atoms, if the copper zero phonon lines are observed.

2.4 Electronic Properties

ZnO as a hexagonal material that crystallizes in the wurtzite structure and possesses C_{6v} symmetry with the c axis being the principal axis. The band structure of ZnO exhibits a splitting of the valence bands at the Γ-point due to several effects. Of particular interest are the ordering of the valence bands and the selection rules for optical transitions, as such these are subject to experimental investigation within this work. The basic phenomena that lead to the valence band splitting are briefly explained, followed by a review of the current research with regards to the ordering of the valence bands and the deduction of the allowed optical transitions.

2.4.1 Crystal Field Splitting

The crystal field (ligand field) is known as the effect of the electrical field of neighboring ions (ligands) on the energies of the valence orbitals of an ion in the crystal. For degenerated semiconductors like diamond or zincblende structures, the crystal field energy is zero. This does not apply to wurtzite (C_{6v}) structures like ZnO since they posses a principal axis. In ZnO, the conduction band (CB) is formed from the $4s^2$ electrons of Zn having s-like character, while the upper valence bands (VB) are generated by the $2p^4$ electrons of O with p-like character. The wurtzite crystal field leads to a discrimination of p_z-like states in the valence band from the p_x-like and p_y-like ones and thus removes part of the degeneracy of the p levels. This produces a valence band splitting that is not found in zincblende semiconductors.

Disregarding the crystal field, the symmetry at the center of the Brillouin zone for the s-like conduction band is Γ_1 and for the p-like valence band is Γ_4. The influence of the crystal field in ZnO leads to a splitting of the Γ_4 valence state into a upper Γ_5 (p_x, p_y) doublet and a lower Γ_5 (p_z) singlet state. This splitting was found to be 41.7 meV [81] and is schematically illustrated in Fig. 2.4. The crystal field splitting in ZnO has the largest influence on the energy levels of the valence bands, compared to other effects, such as the spin-orbit coupling (chapter 2.4.2), Zeeman splitting (chapter 3.6) or strain field effects (chapter 2.5).

2.4.2 Spin-Orbit Coupling

The orbital motion and the magnetic spin moment are coupled via the magnetic interaction of the magnetic field of the orbital motion with the magnetic spin moment. In ZnO, the introduction of spin $D_{1/2}$ considering the spin-orbit interaction leads to a splitting of the doubly degenerated Γ_5 valence state, which is represented by the direct products

$$\Gamma_5 \otimes D_{1/2} \quad \rightarrow \quad \Gamma_7 + \Gamma_9 \tag{2.2}$$

$$\Gamma_1 \otimes D_{1/2} \quad \rightarrow \quad \Gamma_7 \tag{2.3}$$

and thus results in a valence band maximum that is split into a triplet. Although the spin-orbit interaction increases with the atomic number Z, it is smaller than the crystal field splitting in ZnO. Therefore the Γ_1 state remains the lowest of these three valence states. Nevertheless, a negative spin-orbit splitting could reverse the ordering of the top most valence levels. Such a negative splitting was first discussed in copper and silver halides by Cardona [82], while Shindo *et al.* [83] explained it by lower-lying d-bands and calculated a value of $E_{s-o} = -8.7$ meV. More recent calculations determine this value to -8.0 meV [81]. The influence of a negative effective spin-orbit splitting on the valence band ordering in ZnO will be discussed in chapter 2.4.3.

The band structure with the band symmetries and selection rules for different polarization directions, taking crystal-field-splitting and spin-orbit-coupling into account, is presented in Fig. 2.4.

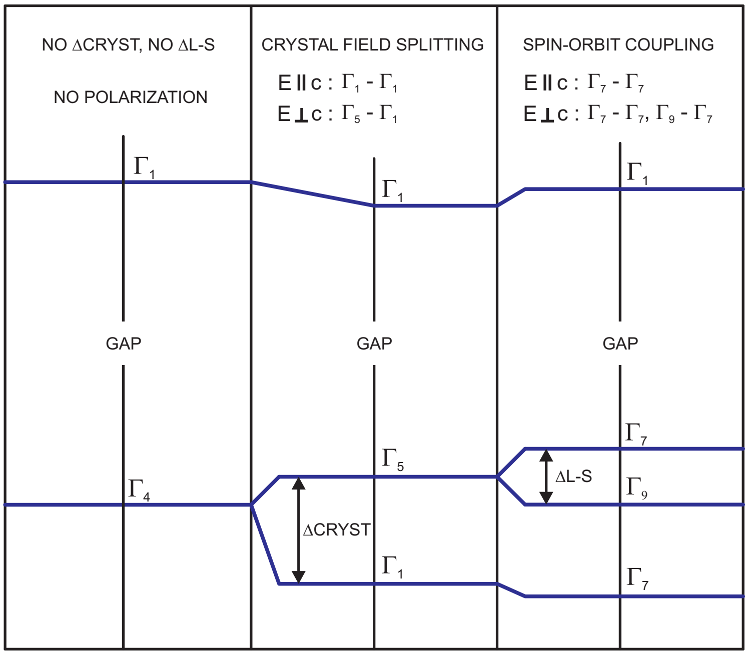

Figure 2.4: Band structure and selection rules with crystal-field-splitting and spin-orbit-coupling for ZnO. The allowed transitions for the various polarization direction of the electric wave vector with respect to the crystal c axis are indicated. Following the model of Birman [84, 85].

2.4.3 Valence Band Ordering

The valence band of ZnO, having a p-like character at the Γ-Point, is split due to the crystal field and spin-orbit interaction into three doubly degenerated sub-bands, which are labeled *A*, *B*, and *C* from the highest to the lowest band. The ordering of the valence bands, however, has been subject to extensive discussions [12, 27, 28, 86, 87] since the first investigations of the valence-band maximum fine structure by Thomas in 1960 [12]. Thomas came to the conclusion that the symmetry of the valence bands from the *A*, *B*, and *C* band is Γ_7, Γ_9, Γ_7 rather than Γ_9, Γ_7, Γ_7 and therefore anomalous compared to the usual ordering in other wurtzite II-VI materials like ZnSe and CdS. Theoretical calculations within the framework of the local density approximation (LDA) [88] explain the reversed order of the top valence bands by a negative effective spin-orbit coupling, that originates from the contribution of 7 eV below the valence band lying Zn 3d bands [89].

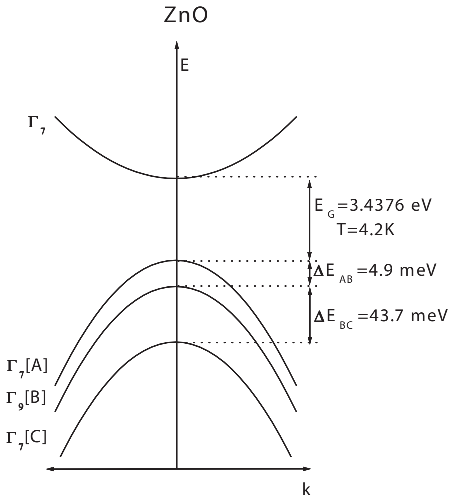

Figure 2.5: Splitting of the valence band into the A, B, and C sub-bands with Γ_7, Γ_9, Γ_7 symmetry caused by the combined effects of crystal-field splitting and spin-orbit coupling. The energy differences between the bands at the Γ-point are indicated for $T = 4.2$ K. Taken from [24].

Latest results show strong theoretical and experimental evidence [81,90] that the valence band ordering is indeed Γ_7, Γ_9, Γ_7 as originally proposed by Thomas. This assignment is also supported by the experimental results in this thesis.

2.4.4 Selection Rules for Optical Transitions

Analogous to the selection rules in atomic physics, i.e. the angular momentum can only change by one ($\Delta l = \pm 1$) for electric-dipole (E1) transitions, there are similar selection rules for solids that are determined by the symmetry of potentials in crystals. In order to deduce the selection rules, it is appropriate to use group theory considerations. Assuming the symmetry of the initial state $|i\rangle$ and the final state $\langle f|$ (i.e. the conduction band and the involved valence band for a electron-hole recombination) as well as the symmetry by which the perturbation Hamilton operator H_p transforms is known, it is directly apparent if the transition is allowed or forbidden by applying the matrix-element theorem:

$$\langle \psi_f | H_p | \psi_i \rangle \neq 0 \Leftrightarrow \Gamma_{\psi_f} \in \Gamma_{\psi_i} \otimes \Gamma_{H_p} \tag{2.4}$$

The matrix element of the Hamiltonian and the two wave-functions representing the initial and final state in eq. 2.4 can only differ from zero when the direct product of the representations of ψ_i and H_p contains an irreducible representation of ψ_f.

Using the matrix-element theorem, one can now easily obtain the selection rules for optical dipole transitions in ZnO. The zone center conduction band in ZnO is s-like with Γ_7 symmetry, while the valence band is p-like and split into three sub-bands having either Γ_7 or Γ_9 symmetry as discussed in chapter 2.4.3. The Hamiltonian for E1 transitions in crystals is represented by the dipole moment operator

$$p = (\frac{e\hbar}{imc})\mathbf{A} \cdot \nabla \tag{2.5}$$

with $\mathbf{A}$ being the vector potential. The dipole moment operator for electric dipole transitions transforms like x, y, or z depending on the polarization direction. For $\mathbf{E}$ being the electric vector of the incident light parallel or perpendicular to the c axis in wurtzite crystals with C_{6v} symmetry, the operator corresponds to different irreducible representations, which are Γ_1 for $\mathbf{E}\perp c$ and Γ_5 for $\mathbf{E}\| c$.

The intrinsic exciton ground state symmetries can be derived by calculating the direct product of the group representations of the band symmetries (Γ_7 for the conduction band, and Γ_7 or Γ_9 for the valence bands):

$$\Gamma_7 \otimes \Gamma_7 \quad \rightarrow \quad \Gamma_5 + \Gamma_1 + \Gamma_2 \tag{2.6}$$

$$\Gamma_7 \otimes \Gamma_9 \quad \rightarrow \quad \Gamma_5 + \Gamma_6 \tag{2.7}$$

According to the previous discussion it can be concluded that Γ_1 and Γ_5 are allowed transition for $\mathbf{E}\perp c$ and $\mathbf{E}\| c$, respectively, whereas Γ_2 and Γ_6 are forbidden. In addition, the Γ_5 and Γ_6 excitons are found to be doubly degenerated, while the Γ_1 and Γ_2 are singly degenerated.

2.5 Strain Effects

Hetero-epitaxial layers, i.e. thin films grown by vapor phase epitaxy on a different substrate, are subject to residual strain. Due to the lattice mismatch between the substrate and the deposition layer as well as difference in the thermal expansion coefficients of substrate and deposited material, the sample is prevented from being completely relaxed, which leads to either tensile or compressive strain. The incorporation of defect complexes produces additional strain in the vicinity of the defects.

The influence of strain on the optical properties can be extensive and effect both the intrinsic and extrinsic transitions in the crystal. Photoluminescence and absorption spectra of free and bound exciton lines (chapter 3.2) clearly exhibit shifted peak positions for samples with residual strain compared to the known energies for completely relaxed samples. Biaxial tensile strain leads to a decrease of the transition energy indicating a smaller bandgap, while compressive strain increases the transition energy. Annealing at high enough temperatures was found to reduce the built-in compressive strain resulting in red shift of the optical transitions [91].

In addition, in-grown strain can relax the selection rules since it reduces the symmetry of the crystal. Koda and Langer [92] first reported the splitting of exciton lines in wurtzite crystals when stress is applied but were unable to explain it, since all orbital degeneracies of the valence band are lifted by the trigonal crystal field and the spin-orbit coupling (Fig. 2.4). However, a theoretical interpretation for the splitting of the Γ_5 exciton could be provided by Akimoto *et al.* [93]. They found that the combined effects of stress and the electron-hole exchange interaction in a quasi-cubic model were able to predict the splitting as well as observed polarization patterns for the free exciton.

Finally, it was shown by Gil *et al.* [94] that the influence of strain-field effects could reverse the ordering of the valence bands, thus leading to reversed peak positions for the top most A and B valence bands, although they assumed the Γ_9, Γ_7, Γ_7 ordering for the A, B, C valence band, which was originally proposed by Reynolds *et al.* [86]. Because of these effects, internal strain plays an important role in the interpretation of optical spectra and should be considered as a source for observed shifts or splittings in PL or PT data.

Chapter 3

Fundamental Effects of the Experimental Techniques

3.1 Introduction

This chapter deals with the physical origin and manifestation of optical processes in semiconductors and particular in ZnO that are the primary source of information in photoluminescence (PL) and phototransmission (PT) spectroscopy. Hence, understanding these effects is important in order to discuss and interpret the acquired spectra. In particular, these are free and bound excitons, donor-acceptor-pairs (DAP), band-acceptor transitions (e-A) and two-electron-satellites (TES) as well as the influence of the Zeeman effect in external magnetic fields on the different types of bound exciton complexes.

3.2 Excitons

Free electrons and holes, as a pair of opposite charge, experience a Coulomb attraction and form excitons. For a strong electron-hole interaction, as often appears in ionic crystals, the electron and the hole are tightly bound to each other and the binding distance is of the order of one lattice constant. These excitons are known as Frenkel excitons. If the Coulomb interaction is screened by valence electrons, as in most semiconductors, the electron-hole pairs are only weakly bound since the overlap of their wavefunctions is smaller and the so called Wannier excitons can be spread out over several unit cells. Since Frenkel excitons are not of importance for the evaluation of the experimental results in this thesis, the following discussions will always refer to Wannier excitons.

One usually distinguishes between free excitons which can move relatively undisturbed through the crystal and bound excitons that are attracted to impurities. The binding energy of a free exciton can be calculated using the effective mass approximation within the framework of the hydrogen model. The exciton ionization energy is then given by

$$E_x = \frac{1}{4\pi\varepsilon_0}\frac{\mu e^4}{2\hbar^2\varepsilon_0^2}\frac{1}{n^2} \tag{3.1}$$

where $n \in \mathbb{N}$ indicates the different exciton states and μ is the reduced mass

$$\frac{1}{\mu} = \frac{1}{m_e^*} + \frac{1}{m_h^*} \tag{3.2}$$

with m_e^* and m_h^* being the electron and hole effective masses. For the minimum or maximum of a parabolic band, i.e the $\Gamma-$Point in ZnO, the effective masses to a good approximation can be considered to be a constant with different values for electrons and holes, depending on the curvature of the bands:

$$\frac{1}{m^*} = \frac{1}{\hbar^2}\frac{\partial^2 E}{\partial k^2}. \tag{3.3}$$

The intrinsic transition energy involving a free exciton is given by

$$\hbar\omega = E_g + E_{kin} - E_x \tag{3.4}$$

where E_g is the energy of the bandgap, E_x describes the ground state exciton binding energy in eq. 3.1 with $n = 1$, and E_{kin} represents the kinetic energy of the center of mass motion of the two particle system:

$$E_{kin} = \frac{\hbar^2 K^2}{2M}. \tag{3.5}$$

Due to the very large binding energy of the free exciton in ZnO of 60 meV, the free exciton is highly stable and the exciton recombination luminescence in ZnO samples can be observed even at room temperature and above, dominating the emission spectra.

$$60 \text{ meV} > k_B(T = 300 \text{ K}) = 25.9 \text{ meV}. \tag{3.6}$$

Besides the free exciton luminescence, the near band-gap emission spectrum of ZnO is dominated by recombination luminescence originating from bound excitons, that are localized near an impurity or defect site. At low temperatures, high quality ZnO samples exhibit a wide variety of different exciton lines with linewidths as narrow as 40 μeV. Transitions involving bound excitons emit photons with an energy

$$\hbar\omega = E_g + E_{kin} - E_x - E_{loc} \tag{3.7}$$

with E_{loc} being the location energy of the bound exciton at the impurity, by which the transition energy is reduced as compared to the energy of the free exciton. These bound exciton lines have been extensively studied by many researchers and were first

Excitonic lines in ZnO						
line	wavelenght [nm]	energy [eV]	loc. energy [meV]	TES spacing [meV]	donor binding E. [meV]	chemical origin
A_L	367.12	3.3772				
A_T	367.26	3.3759				
I_0	367.63	3.3725	3.4			
I_1	367.71	3.3718	4.1			
I_{1a}	368.13	3.3679	8.0			
I_2	368.19	3.3674	8.5			
I_3	368.29	3.3665	9.4			
I_{3a}	368.34	3.3660	9.9			
I_4	368.69	3.3628	13.1	34.1	46.1	H
I_5	368.86	3.3614	14.5			
I_6	368.92	3.3608	15.1	38.8	51.55	Al
I_{6a}	368.96	3.3604	15.5	40.4	53	
I_7	369.01	3.3600	15.9			
I_8	369.03	3.3598	16.1	42.1	54.6	Ga
I_{8a}	369.08	3.3593	16.6			
I_9	369.37	3.3567	19.2	50.6	63.2	In
I_{10}	369.76	3.3531	22.8	60.2	72.6	
I_{11}	370.28	3.3484	27.5			

Table 3.1: Exciton recombination energies and related properties of ZnO. Taken from Meyer *et. al* [24].

theoretically evaluated for nonmetallic solids by Lampert [95] and experimentally proven in silicon by Haynes [96]. For ZnO, the exciton structure was first studied by Thomas and Hopfield [12, 97, 98]. However, the assignment of some excitons bound to neutral or ionized acceptor and donor impurities in ZnO, as well as their chemical origin, is still under debate. The different emission lines with their binding energies in fully relaxed bulk ZnO samples are listed in table 3.1.

3.3 Donor-Acceptor-Pairs (DAP)

Semiconductors with significant concentration of donors and acceptors can exhibit radiative recombinations known as donor-acceptor pair (DAP) transitions. Under equilibrium conditions, some electrons from donors will be compensated by acceptors and therefore form ionized donors (D^+) and acceptors (A^-). Electrons and holes created by optical excitation in the conduction and valence band can then be trapped at the ionized impurity to produce neutral D^0 and A^0 centers. Returning to equilibrium, some of the electrons and holes bound to the neutral donors and acceptors will recombine by emitting photons. Both, the acceptor and the donor must be neutral for the transition to take place. With increasing temperature, the DAP lines often disappear as the shallow donor state thermally ionizes. The photon energy, which is characteristic of the DAP transition is given by

$$\hbar\omega = E_g - E_A - E_D + \frac{1}{4\pi\varepsilon_0}\frac{e^2}{\varepsilon_0 R}. \tag{3.8}$$

where E_A and E_D are the donor and acceptor binding energies, respectively. The last term describes the Coulomb interaction between the ionized donor and acceptor with R being the distance between D^+ and A^-, that leads to an increase of the emitted photon energy. The distance R in eq. 3.8 can by roughly estimated by

$$R = (\frac{3}{4}\pi\varepsilon_0 N_A)^{\frac{1}{3}}. \tag{3.9}$$

with N_A being the acceptor concentration.

In 1956, Prener and Williams first proposed DAP transitions as luminescence centers in compound semiconductors [99]. A good review of the early literature concerning DAPs by Williams can be found in reference [100].

3.4 Band-Acceptor Transitions

Band-band transitions involving the recombination of free electrons and free holes that are excited to the conduction and valence band, respectively, usually dominate for higher temperatures. The thermally excited carriers accumulate at the bands' extremes and recombine with high probability for allowed E1 transitions in direct semiconductors. On the other hand, (e, A) transitions (or in general free-to-bound transitions) are more dominant at lower temperatures, where the carriers tend to be localized at impurities. For p-type material with ionized acceptor states A^+, excited electrons from the conduction band can recombine with the holes trapped at the acceptors. Such transitions involving free electrons and holes bound to an acceptor are known as band-acceptor (e, A) transition. The energy of the emitted photons is given by

$$\hbar\omega = E_g - E_A. \tag{3.10}$$

Equivalent consideration applies for donors in n-type material. Hence, the observation of free-to-bound transitions provides an efficient way of measuring the impurity binding energy.

With increasing acceptor concentration, the average distance between the impurities becomes smaller, leading to a significant overlap of their wavefunctions. This results in the formation of an impurity band and therefore a broadening of the free to bound transition luminescence. In addition, the peak in the emission spectra red-shifts, due to bandgap renormalization for high impurity densities. This energy shift is a many-body effect and can be calculated from density functional theory within the local density approximation [101, 102].

The intensity of the electron to acceptor luminescence is a function of temperature. For low temperature ($k_B \ll E_A$), electron-acceptor recombinations are dominant, but for higher temperatures more holes are excited from the acceptor level to the valence band, thus leading to a decrease in the amount of (e, A) transitions and an increase in band-band transitions. The temperature dependence of the band-acceptor emission intensity is described by

$$I_{e-A} = 1 - exp\left[\frac{-E_A}{k_B T}\right]. \tag{3.11}$$

The ionization energy of the acceptor E_A can therefore be determined in graphs visualizing $ln\left[1 - (I_{e-A}/I_0)\right]$ as a function of $1/(k_B T)$. Such plots are known as Arrhenius plots, and provide a convenient method to obtain the ionization energies of shallow impurities.

3.5 Two Electron / Two Hole Satellites (TES, THS)

A strong indicator for bound excitons to be donor related is the appearance of two electron satellites (TES) in the emission spectra. They occur when the electron of a neutral donor D^0 is excited to a $n = 2$ or higher final state during the bound exciton recombination. These were first experimentally identified by Dean *et. al* in GaP [103] and later by Reynolds *et. al* [104, 105] in ZnO. For the principal bound exciton transition, the electron of the neutral donor is left in its $n = 1$ $(1s)$ ground state. The energy difference from the donor ground state to the corresponding excited state is provided by the exciton recombination (D^0, X). Hence, the TES lines appear as low-energy sidebands of the principal bound exciton transition. The energy spacing, given by the atomic energy levels of the donor atom, is therefore characteristic of the individual donor and allows the determination of donor binding energies. The energy transfer process from the exciton to the electron is less probable than the direct exciton recombination leading to a much weaker emission intensity.

Acceptor bound exciton recombinations can also exhibit low energy sideband emissions, originating from two hole satellites (THS). They appear analogously when a hole of a neutral acceptor is left in an excited state after the bound exciton recombination. Since the binding energies for acceptors are significantly larger than those of donors in ZnO, the THS are much further separated from the parent main (A^0, X) transitions than the TES in the case of donors. By comparing the energy spacing with the known binding energies of donors and acceptors in ZnO, the observation of two electron or two hole satellites is thus a reliable indicator for bound exciton transmissions to be donor or acceptor related, respectively.

The binding energies of donors can be deduced by the analysis of the localization of the TES lines and the calculation of the effective electron polaron Rydberg Ry^* for the donor bound exciton from the effective mass theory. Strictly speaking, the excited $n = 2$ states in a polar hexagonal semiconductor like ZnO are split into $2s$, $2p_z$ and $2p_{x,y}$ states due to the effects of anisotropy and the polar interaction with optical phonons. A numerical study of $n = 2$ splittings by Engineer and Tzoar [106] orders the $2p_z$ state at the lowest energy followed by $2s$ and $2p_{x,y}$ with equal spacing of 0.4 meV. Therefore, the TES lines originating from donor bound exciton transitions, leaving the electron in the excited $2p_{x,y}$ state, are found in the spectra at the largest distance from the principal bound exciton transitions, considering only $n = 2$ excited states. Since the $2p_{x,y}$ lines are usually also of the highest intensity, the following discussion will focus on these transitions. However, theoretical calculations by means of perturbation theory, taking anisotropic effects into account, have been performed by Sak [107] and Larsen [108].

In the spectra, the final state excitations $\Delta E_{1s\leftrightarrow 2p_{x,y}} = E_{2p_{x,y}} - E_{1s}$ is given by the distance of the TES lines to the associated donor bound exciton recombination lines. The donor ionization energy is then determined by

$$E_D = E_{1s\leftrightarrow 2p_{x,y}} + E_{2p_{x,y}} \tag{3.12}$$

with $E_{2p_{x,y}}$ being the binding energy of the $2p_{x,y}$ state. Within a simple hydrogen like effective mass approximation, the energy separation of the $n = 1$ and $n = 2$ is determined by $3/4\ Ry^*$. Hence, the value of the binding energy of the $2p_{x,y}$ state is found to equal $1/4\ Ry^*$, where Ry^* is the effective electron polaron Rydberg. Calculating the binding energy of the effective mass donor polaron with the equation given by Sak [107] and Larsen [108], the binding energy of the $2p_{x,y}$ state, depending on the used values of the effective mass and dielectric constants, can be determined to 12.6-12.9 meV [24, 109]. Using theses parameters, the spacing of a TES line from its parent transitions provides a rather direct determination of donor ionization energies with a precision comparable to that of donor infrared absorption or photocurrent measurements.

Haynes first described a correlation between the impurity ionization energy E_D or E_A and the bound exciton localization energy E_{loc}, which shows a linear dependence determined by

$$E_{loc} = aE_i + b \tag{3.13}$$

with E_i being E_D or E_A. It is further found that the energy spacing in the TES range for different donors should be the same as those observed in the $(\mathrm{D}^0, \mathrm{X})$ range but expanded by a stretching factor s that is directly related to the factor a in the generalized Haynes rule and is written as

$$\frac{|\Delta E_{TES}|}{\Delta E_{loc}} = \frac{a+1}{a} = s \tag{3.14}$$

where ΔE_{loc} is the variation of the bound exciton localization energies for different donors and ΔE_{TES} is the variation of the TES energies with

$$E_{TES} = E_{FX} - E_{loc} - E_{1s \leftrightarrow 2p_{x,y}} \tag{3.15}$$

being the energy of the two electron satellite and E_{FX} the energetic position of the free exciton given in eq. 3.4. By linear fitting the line positions in the experimental results, it is possible to derive the stretching factor s and the parameters a and b, respectively. Sauer *et al.* [109] and Meyer *et al.* [24] have recently reported values of 0.37 meV and 0.365 meV for a and -4.5 meV and -3.8 meV for b. Applying these parameters to Haynes rule it is thus possible to deduce the donor binding energy directly from the bound exciton localization energy E_{loc}, determined by the separation of the bound exciton recombination from the free exciton transition.

3.6 Zeeman Effect of Bound Exciton Complexes

In 1896, Zeeman observed a broadening of spectral lines due to applied external magnetic fields that could be explained by a splitting into separate components under observation with high spectral resolution. The degeneracy of the magnetic quantum states m_J is lifted by the external magnetic field, leading to a Zeeman splitting into $2J+1$ states (neglecting the hyperfine splitting due to non-zero nuclear momenta), with $\mathbf{J} = \mathbf{L} + \mathbf{S}$ being the total angular momentum.

For the free electron in a magnetic field, the electron spin induces a splitting of the energy levels by

$$\Delta E = \pm \frac{1}{2} g \mu_B B \tag{3.16}$$

where μ_B is the Bohr magneton and $g = 2.0023$ is the electron g-factor for the free electron, which in general links the orbital and spin momenta with the associated magnetic momenta. However, in solids ΔE is determined by an effective g-factor that can differ considerably from the g-value of the free exciton.

Thomas and Hopfield showed that the g-values of donors and acceptors in semiconductors, the binding energies of the various complexes, and even energy levels and g-values of excited states of donors and acceptors can be obtained from emission and transmission spectroscopy in an external magnetic field using the Zeeman effect [110]. As discussed in chapter 3.2, excitons can be bound to neutral or ionized donors or acceptors. The neutral impurities as well as the formed exciton complexes are doublet state ($S = 1/2$), since the electrons or holes of the bound exciton complex cannot have parallel spin. This spin configuration is known to result in an unstable configuration due to the exchange interaction, hence anti-parallel spins are required. Considering ground states without orbital angular momentum, the energy states of a neutral impurity in an external magnetic field will split according to the g-value of the odd particle in the exciton complex.

The first detailed Zeeman study of bound exciton complexes in ZnO was performed by Reynolds *et. al* in 1965 [86]. Within this work, the observed $I_2 - I_3$ multiplet was attributed to an exciton bound to an ionized impurity, whereas the I_9 was assigned to a neutral impurity complex. Since no thermalization effects could be demonstrated, the identification of the donor or acceptor character of the bound exciton complexes was not possible.

Loose *et. al* [111] later reported a magnetic thermalization of the I_8 and I_9 in ZnO single crystals. Both lines showed the higher energy Zeeman component to be of greater intensity than the lower energy component. Considering the observed linear splitting, all three exciton lines were consequently associated to neutral donor bound exciton complexes. However, several results of this study appeared questionable. By the splitting behavior of the Zeeman components in the magnetic field, the I_2 (D^+, X_B), I_6 (D^0, X_B), and I_9 (D^0, X_B) lines were attributed to ionized or neutral donors involving holes with Γ_9 symmetry from the B valence band. On the other hand, the I_3/I_{3a}, I_4, and I_8 line were assigned to exciton complexes involving holes with Γ_7 symmetry from the A valence band from which the I_4 was associated with a neutral acceptor bound exciton complex.

In 1981, Blattner *et. al* [112] investigated the Zeeman splitting of the ground and excited states of bound exciton complexes in ZnO crystals with magnetic fields up to 10 T. The presence of thermalization effects both in emission and absorption could be explained by the assumption of a non-zero hole effective g-factor $g_h^{\perp}$ (chapter 6.2), but did not allow the assignment of the I_8 to a donor or acceptor bound exciton complex. In addition, the I_9 line was attributed to an acceptor bound exciton complex in agreement with doping experiments, indicating that the I_9 line should originate from a neutral Na acceptor [54].

A study of bound exciton complexes in high-quality ZnO rods by magneto-optics and excitation spectroscopy, which was performed by Gutowski *et. al* [113] in 1988, resulted in the attribution of all lines from I_5 - I_{11} to excitons bound to neutral shallow acceptors with binding energies of 60-120 meV. The anisotropic hole effective g-factor was determined to be $g_h^{\parallel} = -3.02$ and -2.98 for complexes involving holes from the A (Γ_7) and B (Γ_9) valence bands, respectively.

Finally, Rodina *et. al* [90] recently reported a Γ_7 hole effective g-value in parallel fields of $g_h^{\parallel} = -1.24 \pm 0.04$. In particular, the I_4 and I_9 line could be assigned to donor bound exciton complexes by their thermalization behavior, while no evidence for transitions involving Γ_9 hole states could be found. The extensive experimental study combined the investigations of the magnetic and temperature dependent thermalization behavior in emission and absorption with systematic polarization dependent magnetic field measurements in Faraday and Voigt configuration, as well as for arbitrary angles. The theoretical analysis furthermore allowed the explanation of all recorded results, including those previously reported by Reynolds *et. al* [28] under the assumption of a Γ_9, Γ_7, Γ_7 valence band ordering, by assuming a Γ_7, Γ_9, Γ_7 valence band structure (chapter 2.4.3). Consequently, all observed bound exciton recombinations could be attributed to ionized or neutral donor bound exciton complexes involving holes from the A valence band with Γ_7 symmetry.

In summary, the overview of the relevant literature concerning the identification of bound exciton complexes in ZnO by magneto-optical measurements shows a remarkable discrepancy in the results of these studies. Therefore, it has to be concluded that even 40 years after the first Zeeman study of bound exciton complexes in ZnO in 1965, there is still uncertainty concerning the nature of several bound exciton complexes and further research, such as the studies presented within this thesis, is required.

Chapter 4

The Set of Specimens

4.1 Introduction

Optical and structural properties of various ZnO specimens were investigated and are presented within this thesis. The intention of this chapter is to introduce the fabrication techniques and properties of these samples. In particular, three different types of ZnO samples were available for studies. These are bulk single crystals, MOCVD grown specimens and thin films grown on silicon substrates by RF magnetron sputter deposition (MSD). At the beginning, a brief overview of the general growth techniques for these types of specimens is given, followed by the specific properties of the samples. The magnetron sputtered ZnO films were grown and annealed as part of my work at the University of Technology, Sydney. Therefore, the fabrication and doping process is described in more detail (chapter 4.5 and 4.6). On the other hand, the single crystals and MOCVD samples were provided by third parties and their origin and growth conditions are stated in chapters 4.3 and 4.4.

4.2 Growth Techniques

Nowadays, sophisticated growth techniques are able to produce high quality, high purity semiconductors for versatile applications which allowed the impressive development of the semiconductor industry in the past decades. Different growth techniques are available and used for specific applications. For example, it is possible to grow isotropic bulk single crystal with impurity concentrations of less than one part per trillion (10^{12}) and dislocation densities as low as 1000 cm^{-3}. A common technique to fabricate such large single crystals is the slow drawing of a rotating seed crystal in a molten bath of feeder material (Czochralski process) or variants like the Bridgman method. Therewith, it is feasible to grow nearly perfect crystals in the form of ingots with over 300 mm diameter, which can be cut and polished in order to produce, for instance, large silicon wavers for the creation of integrated circuits. In addition, single crystals are the best choice for studies of fundamental physical phenomena of high precision in solids, due to their exceptional low dislocation and impurity concentrations and the absence of strain effects due to lattice mismatched heterostructure layers.

Metal organic chemical vapor deposition (MOCVD) or alternatively metal organic vapor phase epitaxy (MOVPE) is another growth technique, with large industrial applications, that was first introduced in 1968 [114]. It is designed to produce thin epitaxial layers and artificial quantum- and hetero-structures under controlled (non-)equilibrium conditions with high crystalline quality, which are usually grown on top of a bulk crystal (substrate). That way, new semiconductor devices can be produced, which cannot be realized by the growth and cutting of single crystals. However, hetero-epitaxial layers have to deal with the consequences of different lattice constants and thermal expansions coefficients of the involved materials, which can lead to ingrown strain and an increased number of structural defects. In a typical CVD process the substrate is exposed to one or more volatile precursors, which react and/or decompose on the substrate surface to produce the desired deposit. Frequently, volatile byproducts are also produced, which are removed by gas flow through the reaction chamber. A detailed description of the MOVPE process can be found in references [115, 116].

Sputter deposition is one of the most prevalent techniques for the fabrication of thin-film structures on semiconductors. In the industry, it is used to deposit thin films of various materials onto silicon wafers, to apply thin coatings to glass for optical applications and to deposit gate, source, and drain metals for thin-film transistors as well as contacts for PIN diodes. The advantages are the relatively low expenses for acquisition, operation and maintenance and a high flexibility for different material systems. However, the structural quality and purity of the deposited films is inferior compared to the previously discussed techniques. Reviews of the physical sputtering process and deposition techniques can be found, for example, in references [117–119].

4.3 Growth and Properties of the MOCVD Samples

A set of high quality MOCVD grown ZnO samples, consisting of a nominally undoped (MD1750), a nitrogen doped (MD1763), and an arsenic doped ZnO specimen (MD2715), was investigated by optical characterization techniques in order to identify acceptor related luminescence centers. Using metal-organic chemical vapor deposition (MOCVD) with tert-BuOH and DMZn as precursors, a ZnO buffer layer grown at 450°C was initially deposited on the GaN/sapphire substrate.

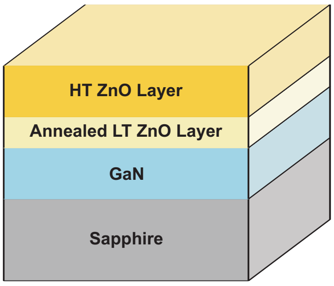

Figure 4.1: Schematic layer structure of MOCVD grown ZnO samples using a low temperature buffer layer on top of the GaN/sapphire substrate (provided by the group of Prof. J. Christen, Magdeburg).

Subsequently, the layer was annealed at 900°C in an N_2 atmosphere, followed by the growth and contingent doping of a thicker high temperature ZnO layer in nitrogen atmosphere at 850°C - 1050°C. The doping was realized via unsymmetrical dimethyl-hydrazine (UDMHy) for nitrogen doping and arsine (AsH_3) for arsenic doping, respectively. The film thickness of the nominally undoped and nitrogen doped ZnO samples is 0.5 μm, whereas the arsenic doped ZnO film is of a thickness of 1.0 μm. All specimens were studied as grown without additional post-growth annealing. The layer structure is visualized in Fig. 4.1.

specimen	substrate	layer thickness	dopant	growing temp.	annealed
MD1750	GaN / sapphire	0.5 μm	undoped	900°C	as grown
MD1763	GaN / sapphire	0.5 μm	N (UDMHy)	900°C	as grown
MD2715	GaN / sapphire	1.0 μm	As (AsH_3)	900°C	as grown

Table 4.1: Growth, doping and annealing properties of the investigated MOCVD grown ZnO samples. (provided by the group of Prof. J. Christen, Magdeburg).

Table 4.1 lists the substrate, layer thickness, dopant and growing temperature for the MOCVD samples. The specimens were grown and provided by the group of Prof. J. Christen from the Otto-von-Guericke-University, Magdeburg. The results of the optical investigations of the MOCVD grown specimens are presented in chapter 6.2 to 6.4

4.4 The Bulk Single Crystals

Two different single crystals were used in order to investigate the influence of dislocations on the optical properties in comparison with the MOCVD grown samples. The results of these studies are presented in chapter 6.4. The first investigated single crystal was produced by EaglePitcher and was subsequently doped with nitrogen (N) by ion implementation. This specimen is labeled EPaN1. The second crystal was doped with sodium (Na) during the growth process at the university of Erlangen. The graphs in chapter 6 simply refer to this specimen as Zn:Na.

4.5 Fabrication of the MSD Samples

A wide variety of undoped and transition metal doped ZnO thin films was grown by RF magnetron sputter deposition at the University of Technology in Sydney. The specimens were investigated concerning their structural and optical properties. The results of these studies are presented in chapter 7. In this section, the sputter process, as well as the sputter conditions and settings for the growth and doping of the ZnO thin films are described, followed by the explanation of the post-growth annealing specifications in section 4.6.

The impact of energetic ions in a solid target material results in the dissociation of atoms into the gas phase driven by momentum exchange. These atoms are not in their thermodynamic equilibrium state and therefore tend to condense back into the solid phase upon colliding with a surface. This effect results in the deposition of sputtered material on all surfaces inside a vacuum chamber. The ions for the sputtering process are supplied by a plasma that is induced in the sputtering equipment. The targets are usually mounted on diode electrodes that can be powered by AC or DC voltage. Compared to DC powered plasmas, radio frequency (RF) powered plasmas at a frequency of usually 13.56 MHz can reach higher plasma density and operate at lower system pressures [120]. Magnetic fields further promote the formation of high plasma densities near the target cathode, thus leading to high levels of ion bombardment and high sputter rates. In addition, magnetically enhanced plasmas can operate at pressures as low as 0.1 mTorr.

Thin films were sputtered in a conventionally vacuum deposition chamber with two independent operating sputter diodes. A 80 mm diameter ZnO target (99.999 % purity) was attached to the RF magnetron diode, while the different transition metal targets were mounted on a magnetron DC powered diode. These were in particular cobalt with a purity of 99.97 % and chromium with a purity of 99.95 % purchased from SCI Engineered Materials.

As substrate material, n-type Si (001) wafers with a thickness of 500 μm were used. The 100 mm wafers were cut into 20x10 mm pieces, cleaned in an ultrasonic acetone bath and subsequently dry-cleaned with ethanol. In addition, a glass substrate was cleaned and placed next to the silicon substrate on a rotation stage inside the sputter deposition chamber. The high purity sputter gases argon and oxygen (99.999 % purity) were induced by two separately controlled leak valves into the chamber, thus allowing an individual adjustment of gas mixture and pressure for each deposition process. Furthermore, the substrate distance from the sputter target, the rotation speed of the specimen stage, and the sputter power for each diode could be customized. Once adjusted, all settings were kept constant during the sputtering process.

In order to determine the optimal sputter conditions with regard to the optical properties of the ZnO thin films, numerous samples without transition metal doping were grown. Subsequently annealing in different atmospheres and at varying temperatures was performed and all samples were investigated with regard to their optical properties by cathodoluminescence spectroscopy (chapter 5.5). The amount of collected data by far exceeds the limit of a reasonable presentation within this work and might be only of minor interest since the purpose was to specify adequate settings for the growth of transition metal doped ZnO samples. Therefore, only the results of these studies as settings for the sputtering of doped films are provided.

Initial studies revealed a higher near band edge emission intensity and slightly lower green luminescence for ZnO films deposited in pure oxygen atmosphere compared to samples grown in an oxygen argon gas mixture and pure argon atmosphere. Therefore, most transition metal doped samples were grown in oxygen atmosphere. However, the origin of the better luminescence properties could not unequivocally be determined, since not only the oxygen excess condition but also the lower sputter rate, due to the lighter and less energetic ions, may have influenced the specimen morphology. For comparison reasons, argon was nevertheless used as a sputter gas for a few transition metal doped films. The most homogeneous films were found to be achieved for a substrate distance of 90 mm from the sputter sources, which were arranged at the top of the chamber, next to each other. The rotation speed of the sample holder was adjusted to 80 rpm. The influence of different sputter temperature could not be investigated, because a heat stage was not combinable with the rotating stage, the later of which proved to be essential.

Before starting the sputtering process, the vacuum chamber was evacuated to a pressure of $2 \cdot 10^{-6}$ Torr and several times flushed with oxygen respective argon gas. Two minutes of pre-sputtering with closed shutters ensured the existence of stable sputter conditions that could be observed for gas pressure as low as 1 mTorr. However, high sputter powers at the DC diode, as they were required in order to achieve heavily transition metal doped samples, made the usage of gas pressures up to 20 mTorr indispensable. The DC power was varied between 17 W and 265 W for the transition metal diode while kept constant at 75 W for the RF ZnO diode. Usually a sputter time of at least 100 min was chosen, leading to a film thickness of at least 300-400 nm.

4.6 Post Growth Annealing of the MSD Samples

The influence of annealing on RF magnetron sputter ZnO films has been investigated by several researchers [121–125]. In spite of several discrepancies in the explanation of physical processes and effects during annealing, the optical and structural properties were generally found to have improved after heat treatment at adequate temperatures. In order to benefit from the significantly increased luminescence output for further studies, each RF magnetron grown sample was cut into several pieces, one representing the untreated reference sample, while the others were annealed in different controlled atmospheres.

The samples were put inside an air sealed heat resistant tube, positioned inside a ceramic furnace. High purity nitrogen and oxygen gas (99.999 % purity) was directed into the tube, ensuring a constant gas flow during the annealing process. The temperature was chosen between 500 and 700 degrees celsius. By inserting and removing the tube in and from the furnace after it reached the intended temperature, comparatively steep flanks in the heating profile could be ensured. The annealing time was usually set to 60 min. Although there is a considerable amount of data on optical and structural properties before and after annealing, it is not the purpose of this thesis to investigate the annealing process in detail. Therefore, the differences are only exemplarily presented and the specimens with appropriate properties after annealing were used for further investigations.

Chapter 5

Experimental Techniques

5.1 Introduction

The purpose of this chapter is to provide an overview of the experimental techniques that were applied to investigate the single crystals and heterostructures, introduced in chapter 4, grown by MOCVD and RF magnetron sputtering. Within the individual sections, the fundamentals of each experimental technique are briefly explained, followed by a description of the specific set-up and settings that I used to perform the measurements. The photoluminescence and transmission measurements with and without external magnetic field, that were used in order to perform high resolution low temperature spectroscopy of the MOCVD grown samples, were conducted at the Technical University Berlin (chapter 5.2 to 5.4). In addition, the experimental methods in chapter 5.5 to 5.9 were applied to perform the investigations of the RF magnetron grown samples, which were grown at the University of Technology in Sydney under the supervision of Prof. Matthew Phillips.

5.2 Photoluminescence (PL)

PL spectroscopy is a powerful tool to study the optical processes in semiconductors and is particular sensitive to point defects, since they often induce characteristic radiative transition channels. A careful study of the large variety of defect related luminescence such as excitons, donor-acceptor-pairs, two-electron-satellites and phonon replica, together with the thermal activation and quenching behavior of transition lines, provides countless information that can be used to determine binding energies and even the chemical origin of point defects. In addition, the formation of deep levels in the band gap, that can serve as non-radiative channels for carrier recombinations, may be identified by their affect on of the PL intensity. An extensive discussion of the PL mechanism and applications can be found in references [126, 127].

A HeCd Laser with the 325 nm line and an output power of 36 mW is used to excite the ZnO specimen above the bandgap. The 441 nm laser line and additional plasma lines are filtered by a 325 nm interference filter. The samples are kept in a helium cryostat at 2 K at an angle of slightly more than 45 degrees to the incoming laser light, avoiding a direct laser reflex into the perpendicularly arranged monochromator. An additional 2 mm thick UG3 bandgap filter is placed in front of the entrance slit. Subsequently, the emitted light is dispersed by a 1200 lines/mm grating, blazed at 1 μm in a 1 m Jarrell Ash monochromator and detected by a bi-alkali detector, which is supplied with 1050 V high voltage.

5.3 Phototransmission (PT)

Phototransmission or absorption spectroscopy delivers, similar to photoluminescence spectroscopy, information about transitions and elementary excitation energies in solids. These transitions can usually be attributed to carriers in the vicinity of defects or impurities, which can be identified by their characteristic absorption spectra. In addition to photoluminescence, non-radiative channels as they often occur for internal transition of deep level impurities such as 3d transition metals, whose energy levels are split by ligand fields and spin-orbit interaction, can be observed and identified.

Transmission spectroscopy is performed by exciting the specimen in dependence of the spectral region with a water cooled 450 W XBO lamp (350-600 nm) or a 250 W halogen-tungsten lamp (above 450 nm). Helium cryostat, dispersion grating and monochromator are identical with those used for PL spectroscopy. The dispersed light is detected by a bi-alkali detector (300-600 nm), a gallium-arsenide detector (300-900 nm) or a nitrogen cooled germanium detector (800-1800 nm).

5.4 Magneto PL/PT

For magneto photoluminescence and phototransmission, the same principals, as discussed in the two previous sections, apply. However, a strong external magnetic field is used to acquire additional information due to the splitting of energy levels caused by the Zeeman effect (chapter 3.6). Therefore, an Oxford magnetic field cryostat with superconducting niobium coils is used to generate magnetic fields of up to 5.5 Tesla, while the sample can be cooled to 1.5 K. A HeCd 325 nm laser line with interference filter is used as excitation source for the PL measurements. The laser light is reflected by a prism of the size of the laser spot onto the sample surface with the electric wave vector perpendicular to the specimen c-axis in reflexion geometry. For absorption measurements, the light of a water cooled 450 W XBO lamp with a blue bandedge filter is focused on the sample in transition geometry.

The transmitted light is subsequently focused on the entrance slit of a Spex 0.75 m double monochromator to which an bandgap UG3 filter is attached, in order to reduce noise and annihilate false signals from laser scattering, plasma lines and higher orders, dispersed by a 600 lines/mm grating, which is blazed at 1600 nm, and detected by a bi-alkali detector. In addition, a $\lambda/4$ plate acting as polarizer and an analyzer could be inserted in front of the monochromator to perform polarization dependent measurements. By varying the angle of the specimen c-axis relative to the magnetic field, additional information regarding the valence band structure could be obtained. Furthermore, the thermalization behavior is studied by adjusting the temperature between 1.5 K and 50 K.

Combining the effects of temperature, angle, magnetic field-strength and polarization dependent measurements, a very powerful investigation method is created, that delivers deep insight into the origin of bound exciton related transitions. The theoretical aspects are shorty introduces in chapter 3.6 and extensively discussed against the background of the experimental results in chapter 6.

5.5 Cathodoluminescence (CL)

The emission of light from a material as a result of carrier excitation in the solid caused by electron beam irradiation is referred to as cathodoluminescence. By utilization of a high vacuum scanning electron microscopes (chapter 5.9), CL spectroscopy combines the high spatial resolution of the SEM with the energy dispersive analysis of luminescence centers and defects. While similar luminescence phenomena, such as photoluminescence (chapter 5.2) may be used for selective excitation of particular emission processes, CL activates all possible radiative recombination channels resulting in a competitive emission process. Furthermore, the irradiation with low energy electron beams (generally 1-40 keV) can lead to the formation or ionization of defects, thus actively influencing the transition channels. Detailed information concerning the physics of CL generation, emission, detection and applications can be found in references [128–130].

All CL measurements were carried out with a modified JEOL 35C SEM. The specimens are placed on a coldstage that can be cooled with liquid nitrogen to 80 K and allows temperature dependent measurements due to an attached heating element. With the sample situated in the focus point of a paraboloidal mirror, photons generated by the electron-specimen interaction are collimated by the mirror. The light is dispersed by an Oxford Instruments Mono CL2 monochromator with a 1200 lines/mm grating blazed at 500 nm and detected by a Hamamatsu R943-02 peltier cooled photomultiplier tube (250-900 nm), where the optical signal is finally transformed into a digital signal and made available for data processing. Consequently, all CL spectra were corrected for the total system response and converted into energy space.

5.6 X-Ray Diffractometry (XRD)

X-ray diffractometry (XRD) is used to acquire a wide variety of information from minerals and grown films such as crystal structure, substrate orientations, lattice parameters, stress levels and phase content. For the characterization of thin film specimens reflection geometry is used, as the substrate is usually to thick for transmission and high angular resolution is required to resolve the relatively sharp peaks in semiconductor materials.

A Siemens D5000 diffractometer is used to perform the $\theta - 2\theta$ scans of deposited thin ZnO films before and after annealing. The results, which are presented in chapter 7.5, provide information about the lattice mismatch between the film and the substrate and are therefore indicative of strain and stress or in polycrystalline films for the grain size. Detailed information about XRD technique and studies of solids can be found for example in reference [131].

5.7 X-Ray Photoelectron Spectroscopy (XPS)

A conventional x-ray tube with a Mg target is used to emit the soft x-rays of the Mg $K_{\alpha_{1,2}}$-lines at an energy of 1253.6 eV. These lines originate from the characteristic $2p_{1/2} \rightarrow 1s$ respective $2p_{3/2} \rightarrow 1s$ internal transitions of Mg, which have the highest transition probability for an empty K-orbital after the core electron is ejected by high energy incoming electrons. The XPS analysis is accomplished by irradiating a sample with the monoenergetic soft x-ray photons from these transitions and analyzing the energy of the detected electrons that are emitted from the sample. The energy detection is performed by a dispersive spectrometer that uses a concentric cylinder connected to different electric potentials to deflect the electrons. Depending on the applied voltage, only electrons of a specific energy can pass the exit slit and are detected by either a simple electron collector that generates a current by external photoelectrons or for low emission rates are amplified by a channeltron.

Using XPS, the chemical identity and concentration of elements in the sample can be determined by comparing the known binding energies of the elements E_b with those deduced from the kinetic energies of the emitted electrons E_{kin}

$$E_b = \hbar\omega - E_{kin} - \phi_s \tag{5.1}$$

where $\hbar\omega$ is the energy of the x-ray photon and ϕ_s the spectrometer work function. Variations in the elemental binding energies arise from differences in the chemical potential of compounds and lead to shifted energy peaks. These chemical shifts can be used to identify the chemical state of the materials.

The penetration power of x-ray photons in solids for the used Mg tube is of the order of $1-10$ μm. However, the electron interaction with matter far exceeds those of the photons. While the mean free path of photons is of the order of micrometers, that of the electrons is of the order of tens of angstroms. Thus, only the electrons that originate from ionization directly below the surface can leave the solid without energy loss due to inelastic scattering and therefore provide useful information on the chemical constituents.

5.8 Energy-Dispersive X-Ray (EDX)

Compared to the XPS (chapter 5.7), EDX spectroscopy does not detect the emitted photoelectrons and auger-electrons but rather the x-ray photons, originating from inner core transitions. The spectrum of the emitted x-rays provide information of the elemental composition and concentration. A FEI XL 30 ESEM (environmental scanning electron microscope) with attached x-ray detector is used to acquire the characteristic fluorescence x-rays emitted from the sample as a result of excitation by the imaging electron beam (chapter 5.9). The range of elements detectable by EDX ranges from Boron to Uranium. Since the EDX detector is designed to view samples under specific conditions, it is important to adjust the working distance to the required value of 10 mm. The electron beam is accelerated by an applied voltage of 15 kV, which is sufficient to identify all expected chemical elements. All measurements are performed in the high-vacuum mode at a pressure of $1 \cdot 10^{-6}$ mbar.

5.9 Scanning Electron Microscopy (SEM)

Scanning electron microscopy is a versatile technique that delivers a rich variety of information on specimen properties, such as composition, topology and crystallography. During SEM inspection a beam of accelerated electrons that is emitted from a tungsten gun is scanned across the specimen surface, resulting in the dissipation of the electron beam energy in the near surface region of the sample. These bombarding electrons, also referred to as primary electrons, dislodge electrons from the specimen. The emitted secondary electrons can be attracted and collected by several detectors producing signals, which are amplified, analyzed and translated into the SEM image.

Depending on the instrumental aperture and resolution, the maximum magnification for a SEM can be as large as one million times, thus allowing the observation of atomic clusters and nanostructures. In order to map the surface of several doped and undoped grown samples before and after annealing, a state of the art SEM of the type LEO Supra 55VP is used. Images are taken at magnifications between 1000 and 300000 times at electron beam acceleration voltage between 2 kV and 15 kV in ultra high vacuum.

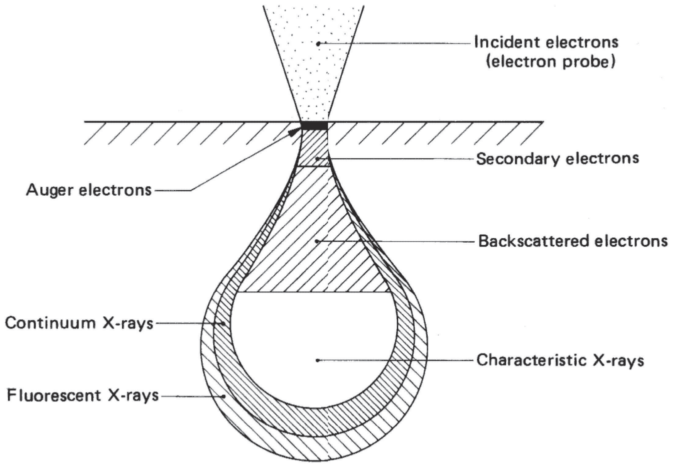

Figure 5.1: Interaction volume of the primary electron beam with the origin of various electron and x-ray signals. Taken from Goldstein *et al.* [132].

The penetration range of primary electrons is limited by elastic and inelastic scattering processes within the specimen and only produces secondary radiation, where they deposit energy into the solid. This region is known as the interaction volume (Fig. 5.1). The maximum penetration depth of the electron beam R_{KO} strongly depends on the acceleration voltage E_a as well as the mean atomic numbers Z and A, and the density ρ. According to the model of Kanaya and Okayama [133] it is given by

$$R_{KO} = \frac{0.0276A}{\rho Z^{0.889}} E_a^{1.67} \tag{5.2}$$

For 15 kV in a semiconductor like ZnO the maximum penetration depth is found to be of the size of 1 μm.

The energy of the primary electrons also determines the quantity of secondary electrons that are collected. The emission of secondary electrons from the specimen increases as the energy of the primary electron beam increases for energies up to around 2 to 5 keV. However, for a large primary beam energy above 5 keV, resulting in a deeper penetration, the number of collected secondary electrons diminishes as the energy of the primary beam is increased, because the beam predominantly scatters electrons deep below the surface of the specimen. Electrons coming from such depths usually recombine before reaching the surface for emission.

Chapter 6

Results and Discussion of Magneto-Optical Studies on MOCVD Grown Samples

6.1 Introduction

The fabrication of high quality p-type ZnO specimens is the main obstacle for ZnO to develop its full market potential for opto-electronic devices as demonstrated by the major progress of GaN in the past decade. In order to improve the p-conductivity, it is essential to identify the chemical origin and activation energy of shallow acceptor states that contribute to the hole carrier concentration and to understand the mechanisms that lead to efficient acceptor compensation in ZnO. Therefore, high quality MOCVD grown doped and undoped ZnO samples, which were introduced in chapter 4.3 and provided by the group of Prof. J. Christen at the Otto-von-Guericke-University, Magdeburg, are investigated to address these questions.

The outcome of various optical investigations, together with an extensive discussion of the results are presented within this chapter. Magneto-optical photoluminescence and transmission spectroscopy (chapter 5.4) as well as temperature resolved PL are applied to determine important characteristics, such as donor and acceptor bound exciton complexes and their thermalization behavior, localization and activation energies of impurity states and the valence band ordering of the investigated ZnO samples.

In addition, the optical properties of ion implanted ZnO single crystals, produced by EaglePitcher, are investigated with particular respect to deeply bound excitons at structural defects. The results of these measurements are compared with those of an arsenic doped ZnO heterostructure, grown by MOCVD in Magdeburg. In general, it applies that presented results, which were not acquired at the Technical University Berlin and are provided by a third party are expressly stated as such.

6.2 Magneto-Optical PL and PT of Nominally Undoped ZnO

Magneto-optical studies are a powerful and versatile method to elucidate the nature of exciton binding centers involved in optical transitions. Careful investigations of bound exciton transitions in magnetic fields provide all the necessary information that is required to determine if the excitons are bound to neutral or ionized impurities and if the impurities are acting as donors or acceptors. Theoretical considerations describing neutral and charged impurities in hexagonal semiconductors, during the applications of external magnetic fields, were first published by Thomas and Hopfield in 1961 [110]. The first experimental studies of II-VI semiconductors were performed by these authors on CdS single crystals and later by Reynolds *et. al* [86] on ZnO single crystals (chapter 3.6).

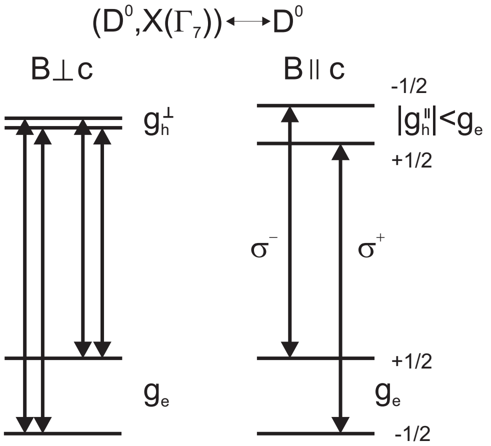

Figure 6.1: Zeeman splitting of donor bound exciton complexes involving Γ_7 valence band transitions. The splitting of the ground state is determined by the electron effective g-value (g_e), while the excited state splitting depends on the the anisotropic hole effective g-value ($g_h^\perp$ and $g_h^\parallel$, respectively). Taken from Rodina *et. al* [90].

The splitting of the ground and / or excited energy levels of an exciton complex when an external magnetic field is applied is caused by the Zeeman effect. This splitting, and consequently the energy for optical transitions between the split excited and ground state, depends on the type of exciton binding center, particularly if the exciton is bound to a neutral or ionized impurity. Excitons bound to ionized impurities can be distinguished from those bound to neutral impurities by a nonlinear splitting of energy levels in the magnetic field perpendicular to the c axis, while excitons bound to neutral impurities exhibit a linear splitting behavior for $\mathbf{B}\perp c$.

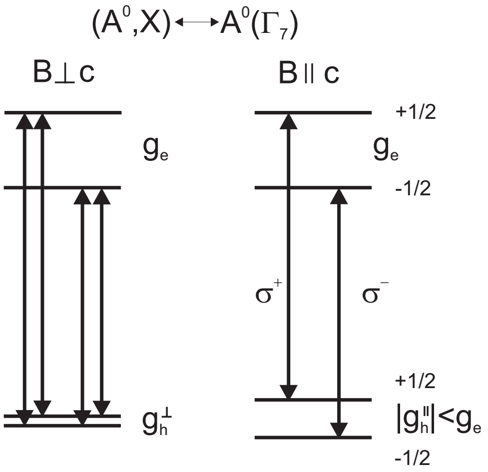

Figure 6.2: Zeeman splitting of acceptor bound exciton complexes involving Γ_7 valence band transitions. The splitting of the excited state is determined by the electron effective g-value (g_e), while the ground state splitting depends on the the anisotropic hole effective g-value ($g_h^{\perp}$ and $g_h^{\|}$, respectively). Taken from Rodina *et. al* [90].

The discrepancies in the literature according to the nature of the I_8 bound exciton line in ZnO as discussed in chapter 3.6, are addressed by systematic temperature and angular dependent photoluminescence and transmission measurements in external magnetic fields. Latest reports suggest that the I_8 line at 3.3598 eV is associated with a shallow donor bound exciton complex, resulting from gallium impurities [24, 134, 135]. In fact, Strassburg *et al.* [135] were able to attribute the large Ga concentration, using secondary ion mass spectroscopy (SIMS), to originate from a significant interdiffusion process of gallium from the GaN-substrate into the ZnO epitaxial film. From the study of two electron satellites (TES), the binding energy of the Ga-donor could be determined to be 54.6 meV [24]. However, the different assignments in previous works require additional studies.

The zero field near bandedge PL spectrum of nominally undoped ZnO (MD1750) is presented in Fig. 6.3. This particular specimen was selected, since the PL spectra exhibits only the dominant I_8 line in the range around 3.36 eV. The absence of the I_6 to I_9 lines is advantageous, since the interpretation and assignment of the individual Zeeman components in applied magnetic fields cannot be complicated by overlapping components originating from adjacent bound exciton lines, as it was observed by Rodina *et. al* [90]. The halfwidth of the I_8 line with approximately 300 μeV is very small for MOCVD grown samples, thus also facilitating the data interpretation for smaller magnetic fields. In addition to the I_8 line, the I_0/I_1 peak and the A free exciton (FX_A) as well as a non-attributed donor bound exciton peak

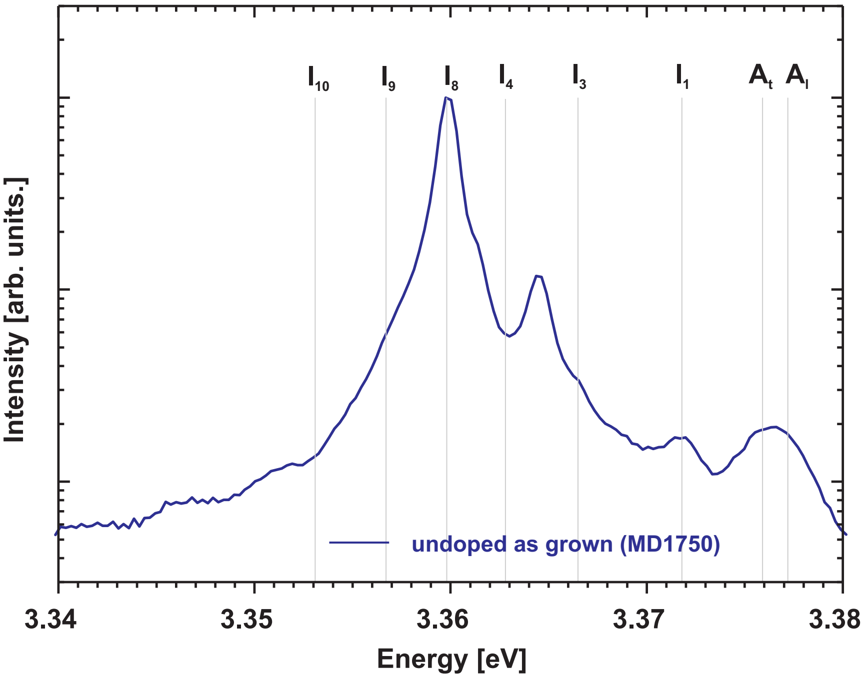

Figure 6.3: Photoluminescence spectra of exciton lines in nominally undoped ZnO (MD1750) at 3 K. The relaxed energies of the exciton recombinations in ZnO single crystals are indicated by the vertical drop lines. The I_8 dominates the bound exciton spectra with a halfwidth of 0.3 meV.

at 3.3648 eV located between the well known positions of the I_3 and I_4 line can be observed. However, the origin of this line remains controversial and is not subject to further discussions within this work.

The magneto-PL spectra of the I_8 exciton line are presented in Fig. 6.4. The left graph shows the spectra in Faraday configuration ($\mathbf{B} \| c$), while the PL data in the right graph have been recorded in Voigt configuration with $\mathbf{B} \perp c$. The strength of the magnetic field is varied from 0 T to 5 T. The results of the PL spectroscopy acquired from different angles between the direction of the magnetic field and the c-axis of the specimen at 5 Tesla are plotted in the center graph. All spectra are recorded at $T = 1.6$ K with the electric field vector of the incident light perpendicular to the specimen principal axis ($\mathbf{E} \perp c$).

In addition, polarization dependent spectroscopy has been performed, using a $\lambda/4$ plate in combination with an attached analyzer. The either right circular polarized (σ^+ with $\Delta s = +1$) or left circular polarized (σ^- with $\Delta s = -1$) light resulting from the bound exciton transitions becomes linear polarized in the $\lambda/4$ plate by a phase shift of one forth of the wavelength leading to a linear superposition of the oscillating electric wavevectors. Depending on the position of the analyzer (±45 deg),

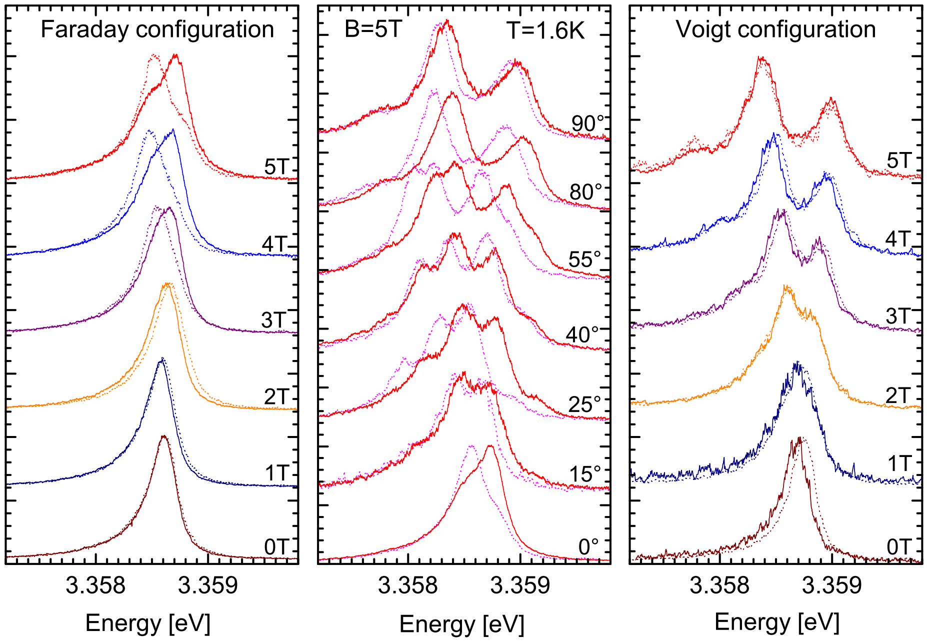

Figure 6.4: Photoluminescence spectra of the I_8 bound exciton line in nominally undoped ZnO at 1.6 K for different magnetic fields, orientations and angles. Left: Faraday configuration ($\mathbf{B}\|c\|\mathbf{k}$), right: Voigt configuration ($\mathbf{B}\perp c\|\mathbf{k}$), center: angles $\vartheta = 0$, 15, 25, 40, 55, 80, 90 between $\mathbf{B}$ and c with $B = 5$ T. The solid and dotted lines indicate the spectra measured for right σ^+ and left σ^- polarized light, respectively.

either the σ^+ or σ^- component can be selected, dispersed and detected. In Fig. 6.4, σ^+ is indicated by the solid lines, while the σ^- polarized light is represented by the dotted lines.

In order to perform a quantitative analysis of the Zeeman behavior, the peak positions for the Faraday and Voigt configuration as well as for the arbitrary angles are displayed in Fig. 6.5. According to Thomas and Hopfield [110, 136], the neutral or ionized character of bound exciton complexes can be determined by the linear or nonlinear splitting behavior of the exciton line in magnetic fields. For ionized impurity centers, the splitting for ($\mathbf{E}\perp c$) is found not to scale linearly with the magnetic field. Particular for low magnetic fields, only the high energy component, resulting from a Γ_5 state is visible, while the low energy component, originating from a $\Gamma_1 \rightarrow \Gamma_6$ transition is forbidden by selection rules (chapter 2.4.4). However, for larger magnetic fields, the selection rules are relaxed due to a spin-spin interaction of Γ_5 states with antiparallel spin, mixed with Γ_6 states with parallel spin, thus allowing the appearance of a new line associated with the Γ_6 state.

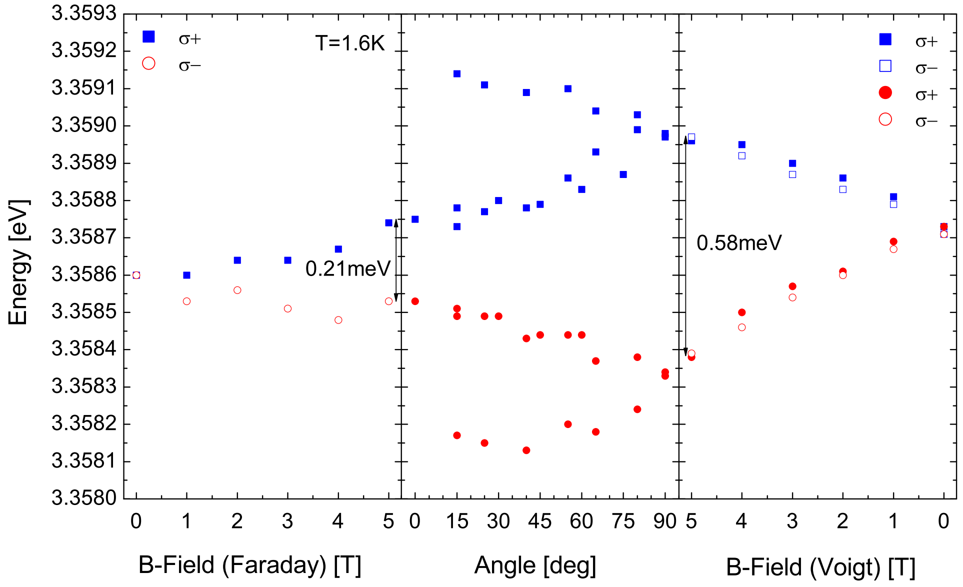

Figure 6.5: Zeeman splitting of the I_8 bound exciton line in nominally undoped ZnO at 1.6 K. Left: Faraday configuration ($\mathbf{B}\|c\|\mathbf{k}$), right: Voigt configuration ($\mathbf{B}\perp c\|\mathbf{k}$), center: arbitrary angles ϑ between $\mathbf{B}$ and c with $B = 5$ T. Solid dots and dashed dots indicate the peak position for σ^+ and σ^+ polarized light, respectively.

The extrapolation of peak positions to $B = 0$ T reveals the presence of the zero-field splitting, ascribed to the spin-spin interaction energy. Such an interaction can not occur in transition lines originating from excitons bound to neutral impurities, since the spin of the two like particles are antiparallel. From the linear splitting in Voigt as well as Faraday configuration in Fig. 6.5 it is evident, following the previous discussion, that the exciton line does not originate from an ionized impurity complex but rather from a neutral one.

The hole and electron effective g-values for an uncharged impurity complex can be calculated by fitting the peak positions of the split exciton lines. For a donor bound exciton complex, the Zeeman splitting of the excited state (D^0, X) and ground state (D^0) is determined by the anisotropic hole effective g factor (g_h) and the isotropic electron effective g factor (g_e), respectively (Fig. 6.1). In the case of an acceptor bound exciton, the splitting of the excited state (A^0, X) is determined by g_e, while the ground state (A^0) splits according to g_h (Fig. 6.2). Strictly speaking, there is not only an anisotropy in the hole g-factor but also in the electron g-factor with reported values of $g_e^{\|} = 1.956 - 1.958$ and $g_e^{\perp} = 1.955 - 1.956$, which is found to become smaller with increasing binding energy of the impurity complex [47, 137].

However, due to the small difference in the electron effective g-values ($\Delta g_e = |g_e^{\perp} - g_e^{\|}| < 0.001$) that can not be resolved by magneto-optical studies but rather by EPR or ODMR, the electron anisotropy is neglected in the further discussion. Thus, g_e can be treated as isotropic.

Following Thomas and Hopfield [136], the absolute value of the hole anisotropic g factor is given by

$$g_h = \sqrt{|g_h^{\|}|^2 \cos^2\vartheta + |g_h^{\perp}|^2 \sin^2\vartheta} \tag{6.1}$$

where ϑ is the angle between the c axis and the direction of the magnetic field B. Apparently, eq. 6.1 delivers $g_h^{\perp}$ for $\mathbf{B}\perp c$ and $g_h^{\|}$ for $\mathbf{B}\|c$. The magnetic anisotropy can be explained in the quasi-cubic approximation considering the expectation values of the orbital angular momentum L_x, L_y and L_z. For the topmost Γ_7 valence state having p_x, p_y like character, it is found that both, L_z and L_x, L_y are nonzero, so that the g value is anisotropic having the form in eq. 6.1, while for a Γ_9 valence band $L_x = L_y = 0$, $L_z \neq 0$ with $g = g^{\|}\cos\vartheta$.

The energy splitting in dependence of the magnetic field is described by

$$\Delta E = \mu_B B(g_e \pm g_h) \tag{6.2}$$

with μ_B being the positive value of the Bohr magnetron, B the magnetic field and g_e and g_h the electron and hole effective g-values, respectively.

From the PL spectra in Fig. 6.5, it is evident that the observed Zeeman splitting for $\mathbf{B}\|c$ is smaller than the splitting in $\mathbf{B}\perp c$ configuration. In addition, the upper Zeeman component in Fig. 6.4 is found to be active for σ^+ polarization, while the lower energy component is active for σ^- polarization. Following the reasoning of Rodina *et al.* [90], these facts can be explained for the top valence band having Γ_7 symmetry with $g_h^{\|} < 0$ and $|g_h^{\|}| < g_e$. In agreement with previous reports [81, 90, 111–113] the hole effective g-factor $g_h^{\perp}$ in $\mathbf{B}\perp c$ is considered to be small. Therefore, the Zeeman splitting in Voigt configuration is primarily mediated by g_e, while the influence of $g_h^{\perp}$ on the splitting size can be neglected. Hence, the smaller splitting in Faraday configuration requires a negative hole effective g-value $g_h^{\|}$ for a $\Gamma_7 \rightarrow \Gamma_7$ transition (Fig. 6.1 and 6.2).

Furthermore, the absolute value of the hole effective g-factor must be smaller than the electron effective g-value to ensure the σ^+ polarized transition to be of higher energy than the σ^- one. However this is not necessarily true if the top valence band is assumed to have Γ_9 symmetry. In order to address this issue, the angular dependent PL data are of great use. According to theoretical calculations [90], the topmost valence band having Γ_9 leads to a crossing of the peak positions of the two inner Zeeman components at an angle ϑ between $\mathbf{B}$ and c of around 40 deg, which is not observed in the spectra. In fact, fitting of the observed splitting in Fig. 6.5 additionally supports the assignment of the top valence band to have Γ_7 symmetry and reveals the following values for the effective g-factors:

g-factor	effective value
g_e	1.87
$g_h^{\|\|}$	-1.26
$g_h^{\perp}$	0.06

Table 6.1: Effective g-values for the I_8 bound exciton complex in nominally undoped ZnO in agreement with the results of Rodina *et. al* [90].

Optical transition from excitons bound to neutral acceptors (A^0, X) are distinguishable from excitons bound to neutral donors (D^0, X) by the thermalization of PL or PT lines. It is important to note that the thermalization behavior of the PL components depends on the splitting of the complex excited state (A^0, X) or (D^0, X) while the thermalization in absorption is caused by the splitting of the ground state (A^0) or (D^0) of the respective bound exciton complex. Since the splitting of the excited state for $\mathbf{B}\perp c$ is determined by the anisotropic hole effective g-factor $(g_h^{\perp})$ with $g_h^{\perp} \approx 0$ (chapter 6.2, Fig. 6.1), the PL intensities of the donor bound exciton transitions $(D^0, X) \rightarrow D^0$ are expected to be equal in $\mathbf{B}\perp c$ and independent of the temperature.

On the other hand, the splitting of the excited state for an acceptor bound exciton complex is given by the electron effective g-factor g_e (Fig. 6.2). Therefore, the intensity of the high-energy component of the $(A^0, X) \rightarrow A^0$ transition in $\mathbf{B}\perp c$ should be less than that of the low energy component for low temperatures, but is expected to increase with rising temperature since more exciton complexes can occupy the higher energy Zeeman level by thermal activation.

The determination of acceptor or donor bound exciton complexes is facilitated for $\mathbf{B}\perp c$, because $g_h^{\perp}$ of the Γ_7 hole is negligible small compared to $(g_h^{||})$ and can be approximated to zero. Thus, it does not cause a significant splitting of the excited state for the donor bound exciton and the ground state for the acceptor bound exciton complexes respectively, that could counteract the total energy splitting determined by the electron effective g-factor g_e. However since $(|g_h^{||}| < g_e)$, the same intensity relation for acceptor bound exciton transitions in $\mathbf{B}||c$ should be observed as discussed for $\mathbf{B}\perp c$.

The results of temperature dependent photoluminescence and absorption spectroscopy in Voigt configuration are displayed in Fig. 6.6. The spectra have been recorded at a magnetic field of 3 Tesla at 1.5 K and 18 K. It is obvious that for low temperatures at 1.5 K the intensity of the high energy PL peak is significantly smaller than that of the low energy component. With higher temperatures, the high energy line increases in intensity. This behavior is predicted for an acceptor bound

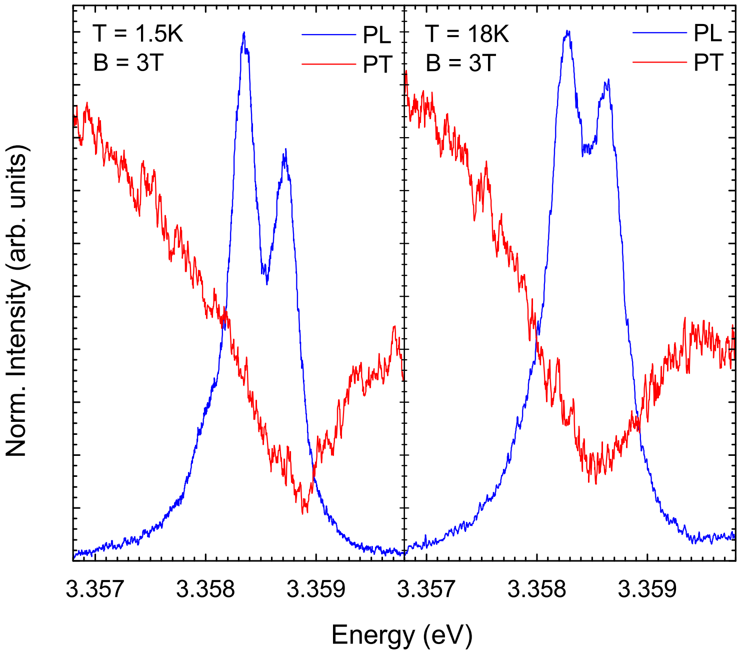

Figure 6.6: Temperature dependent PL and PT of the I_8 bound exciton line in nominally undoped ZnO. The spectra are recorded in Voigt configuration with $B = 3$ T at 1.5 K and 18 K, respectively.

exciton complex. Nevertheless, it should be noted that Rodina *et al.* [90] observed a similar behavior for the I_4 and I_9 exciton line in $\mathbf{B}\perp c$ indicating an acceptor complex, although the PL data in $\mathbf{B}\|c$ and absorption studies allowed the assignment of the I_4 and I_9 line to a donor bound exciton, following previous publications [24, 71, 138].

Hence, the investigation of the thermalization behavior in Faraday configuration would be advantageous. However, due to the additional splitting of the ground or excited state for acceptor and donor complexes in $\mathbf{B}\|c$ respectively, which is determined by the anisotropic hole effective g-factor ($g_h^{\|}$), the total splitting is smaller and consequently the low and high energy peaks were found not to be sufficiently separated at 5 Tesla in Faraday configuration to allow an unambiguous analysis.

In order to support the assignment of the observed emission line to an acceptor bound exciton, temperature dependent absorption spectroscopy is performed. As discussed, the thermalization behavior of the absorption lines depends, unlike in PL, on the ground state (D^0 or A^0) of the impurity complex. Therefore, the intensities of the $A^0 \rightarrow (A^0, X)$ transitions are expected to be equal in $\mathbf{B}\perp c$ (Fig. 6.2). For donor bound exciton complexes, the observed transition intensities in absorption at low temperatures should however be smaller for the low energy component and increase relatively to the high energy peak with raising temperature (Fig. 6.1).

The acquired temperature dependent absorption measurements are shown together with the PL data in Fig. 6.6. It is apparent, that the higher temperature transmission minimum exhibits a shift toward lower energies compared to the 1.5 K low temperature graph. Due to the small energy difference of less than 400 μeV between the two energy components, the decreased signal to noise ratio in transition and a limited spectral resolution, it is supposable that the observed peak consists of the two overlapping absorption components. In that case, the shift to lower energies could be explained by an increase of the low energy component in absorption. However, this interpretation contradicts the PL assignment of the bound exciton complex to be acceptor related, since an increase of the low energy component with temperature in transmission is predicted for a donor complex. Again, the splitting in Faraday configuration is to small too allow useful conclusions.

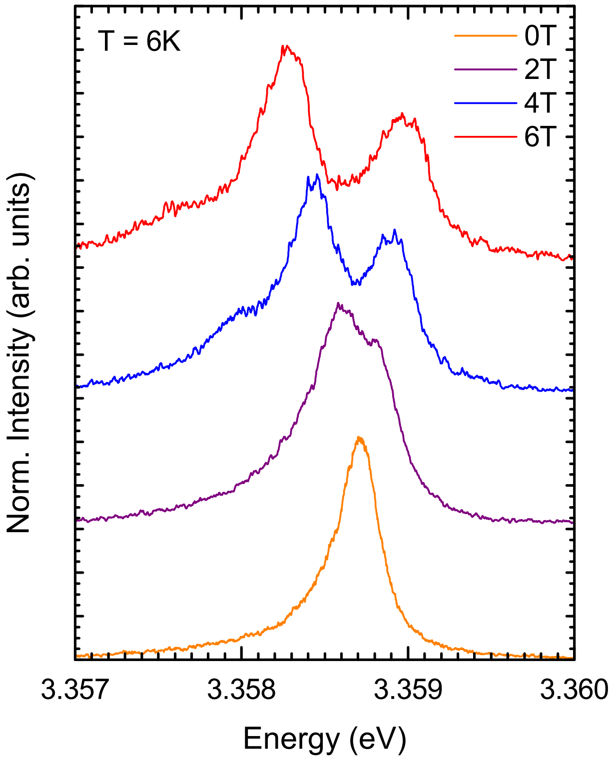

Figure 6.7: Photoluminescence spectra of the I_8 bound exciton line in nominally undoped ZnO as a function of the external magnetic field. The graphs were recorded at 6 K in Voigt configuration for 0-6 Tesla.

Since the thermalization behavior is also revealed by the evolution of the intensity ratio of the Zeeman split components with increasing magnetic field, an analysis of the B-field dependency of the bound exciton transitions is required and might be able to elucidate the inconsistencies regarding the nature of the bound exciton complex. Fig. 6.7 shows the photoluminescence spectra at 6 K for magnetic fields of 0-6 Tesla in Voigt configuration. It appears that the relative intensity of the higher energy component compared to the low energy one is decreasing with increasing magnetic field.

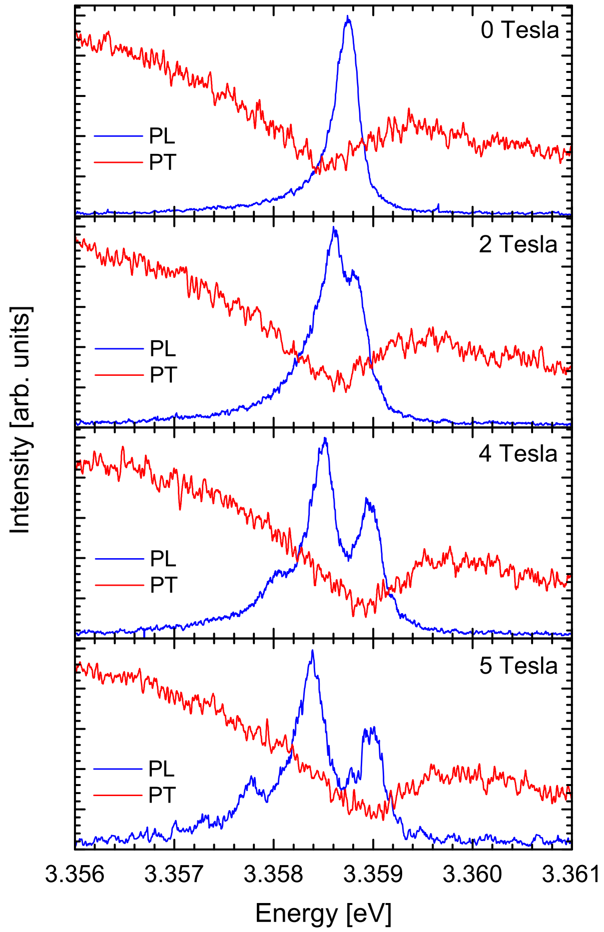

Figure 6.8: The phototransmission spectra of the I_8 bound exciton line in nominally undoped ZnO as a function of the magnetic field are displayed in combination with the respective PL spectra. The graphs were recorded at 1.5 K in Voigt configuration for 0-5 Tesla.

Given that, on the one hand the thermalization in PL depends on the splitting of the excited state and on the other hand the splitting of the excited state for an donor bound exciton complex is determined by $g_h^\perp$, which is known to be very small and therefore should not effect the intensities of the Zeeman components with increasing magnetic field, the observed behavior can only be explained for an acceptor bound exciton. Indeed, the large splitting of the excited state components given by g_e would also theoretically imply a decreasing intensity of the high energy line with increasing field. The observed magnetic thermalization behavior is therefore in excellent agreement with the temperature dependent PL data, indicating an acceptor bound exciton complex.

The results of magneto-dependent transmission spectroscopy at 1.5 K are presented in Fig. 6.8. With increasing magnetic fields the Zeeman splitting of the PL components is apparent. Again, the decreasing intensity of the high energy peak suggests the exciton to be acceptor related. For high magnetic fields (4 T and 5 T) a new peak appears at the low energy side of the two main Zeeman components. This line could be attributed to one of two outer components resulting from forbidden transitions in $\mathbf{B}\perp c$, but it is known to appear for arbitrary angles between $\mathbf{B}$ and c. It can therefore be explained assuming a not precisely perpendicular alignment of the orientation of the samples relative to the direction of the magnetic field.

Focusing on the absorption spectra, it is found that the transmission minimum shifts towards higher energies in accordance with the high energy PL component when increasing the magnetic field. Similar to the previously presented temperature dependent transmission spectra in Fig. 6.6, only one absorption peak can be observed. Since in transmission the thermalization depends on the Zeeman splitting of the ground state, the observed shift could indicates a donor bound exciton complex, thus contradicting the PL results. However this conclusion is not necessarily true. Assuming an acceptor bound exciton complex as suggested from the temperature and magnetic field dependent PL data, the behavior in transmission could only be explained if the transitions to the higher Zeeman component of the excited state are favored by selection rules. This could also explain the occurrence of only one peak in transition. However, since the PL transition does not seem to be effected, this description seems unlikely.

6.3 The Nitrogen Acceptor in ZnO

The zero field PL spectra of nominally undoped (MD1750) and nitrogen doped as-grown ZnO (MD1763) at low temperatures are presented in Fig. 6.9. The nitrogen doping was achieved using hydrazine (N_2H_4) rather than ammonia (NH_3), which has a smaller hydrogen to nitrogen ration. Since hydrogen is known to introduce shallow donor states and efficiently counteracts p-conductivity, a decrease in hydrogen incorporation would therefore be advantageous. The PL spectra of the nominally undoped sample is dominated by the excitonic luminescence, discussed in the previous chapters. Furthermore, the characteristic green luminescence centered around 2.2 eV and several smaller peaks at the low energy side of the main exciton luminescence between 3.2 eV and 3.35 eV, which are subject to discussion in following higher resolution spectra, can be identified in the nominally undoped ZnO specimen. It should be noted that the peak at 1.7 eV results from the second diffraction order of the spectrometer and therefore does not show a new luminescence line.

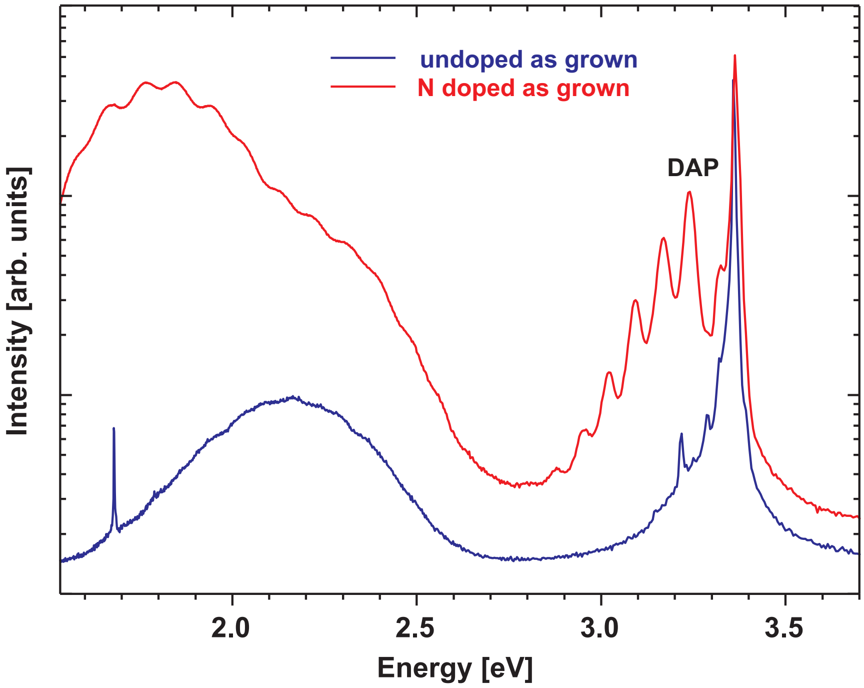

Figure 6.9: PL of nominally undoped and nitrogen doped ZnO at liquid helium temperature.

Compared to the undoped spectra, the nitrogen doped specimen shows significant differences in photoluminescence. These are, in particular, the greatly increased intensity and broadening of the luminescence band between 1.5 eV and 2.5 eV and the appearance of a dominant DAP that is accompanied by 5 phonon replica, thus indicating a strong phonon coupling. The presence of the strong DAP peak after nitrogen doping demonstrates the formation of a considerable amount of shallow acceptor state, which can be attributed to the nitrogen acceptor.

In order to perform a more detailed analysis of the near bandgap luminescence, temperature dependent PL spectra between 3.15 eV and 3.4 eV were analysed and are displayed for the undoped and nitrogen doped ZnO samples in Fig. 6.10 and Fig. 6.11, respectively. The lowest temperature spectra of the nominally undoped

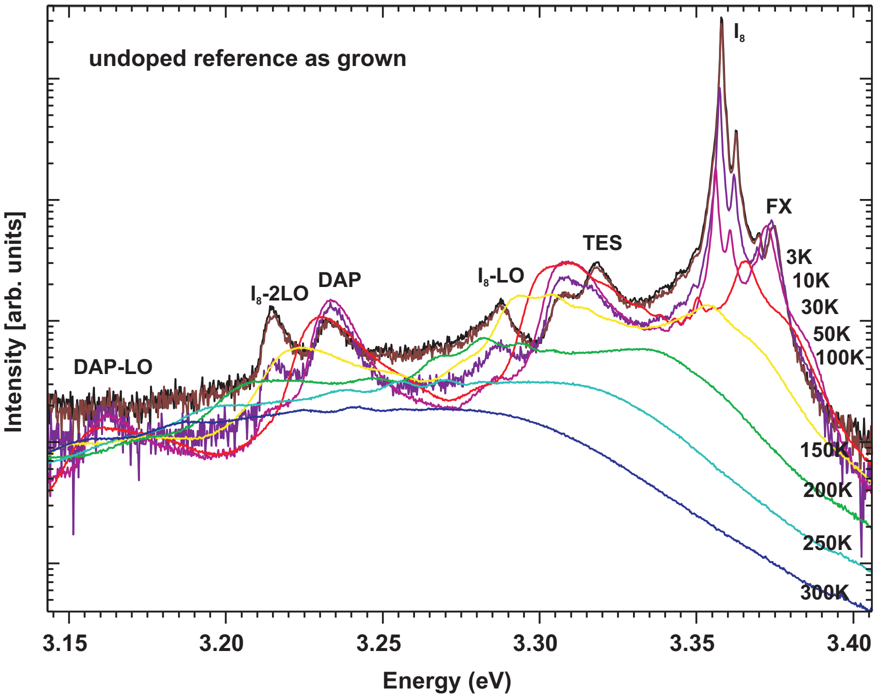

Figure 6.10: Temperature resolved near bandgap luminescence of nominally undoped ZnO between 3 K and 300 K. The spectra were provided by the group of J. Christen, Magdeburg.

ZnO specimen at 3 K (black line) shows several features next to the dominant bound exciton recombination peak at 3.358 eV. First, two lines at 3.286 eV and 3.214 eV can be identified and attributed to the first and second phonon replica of the I_8 line. The spacing between the lines equals 72 meV, supporting the assignment to phonon replica of the I_8 in agreement with previous publications [139–141].

Second, the appearance of a peak at 3.316 eV can be noted, which originates from a two electron satellite (chapter 3.5) and is likely to be associated with the dominant I_8 transition. The energy separation between the TES and the bound exciton line reveals a final state excitation energy $E_{1s\leftrightarrow 2p_{x,y}}$ of 42 meV. By adding the denoted values of the binding energy of the $2p_{x,y}$ state in chapter 3.5, which were calculated for an effective mass like donor, a donor binding energy of 54.9 meV ± 1 meV is derived. This is consistent with the reported values of 54.5 meV and 54.6 meV for the I_8 donor binding energy [24, 109, 135]. Finally, a peak at 3.235 eV with its phonon replica at 3.160 eV can be attributed to a DAP transition (chapter 3.3) in excellent agreement with previous studies of Meyer *et al.* [24].

The low temperature (3 K) PL spectra of the nitrogen doped specimen in Fig. 6.11 also exhibits the main features of the nominally undoped ZnO spectra. In particular, the TES and I_8 phonon replica can be identified besides the domi-

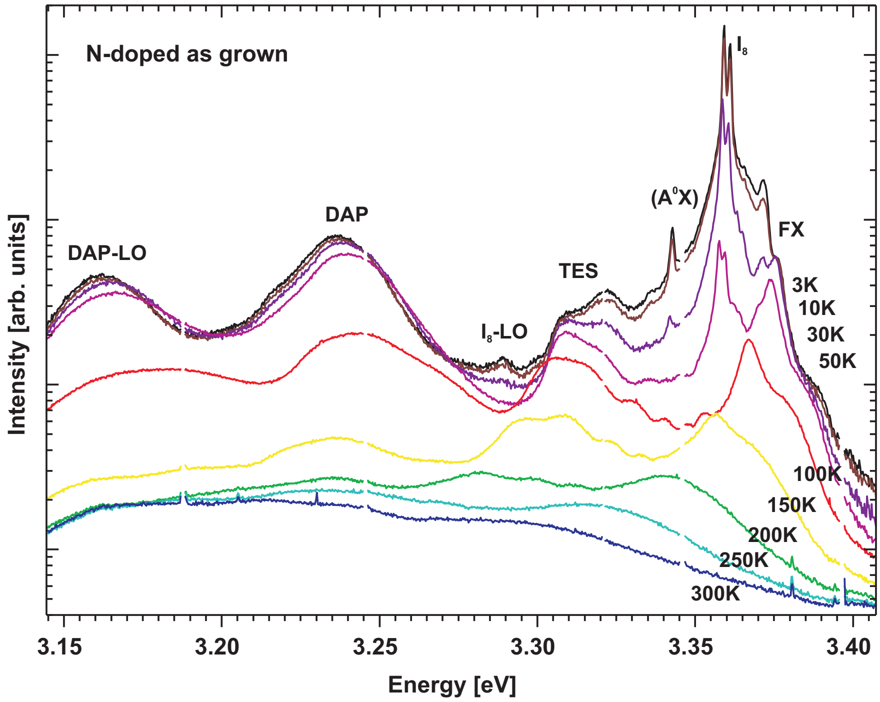

Figure 6.11: Temperature resolved near bandgap luminescence of nitrogen doped ZnO between 3 K and 300 K. The spectra were provided by the group of J. Christen, Magdeburg.

nating bound exciton luminescence. However, there are a few significant differences after doping with nitrogen. In particular, a new peak at 3.342 eV can be observed. The small half width and line shape, as well as the rather quick disappearance with increasing temperature indicates the transition peak to be of exitonic origin. The position at lower energies compared to the main I_0 to I_{11} bound exciton transitions further suggests that the exciton might be bound to an acceptor complex with a typically larger localization and ionization energy.

In addition, it is evident from Fig. 6.9, that the intensity ratio of the DAP at 3.235 eV to the dominant bound exciton lines has increased by at least one order of magnitude for the nitrogen doped ZnO sample. The large amount of phonon replica also hints at the participation of an acceptor in the transition, which usually exhibits a stronger coupling with the optical phonons than donors. With increasing temperature up to 100 K, the center of the DAP transition peak is found to shift towards larger energies and generally decreases in intensity. This temperature dependence is common for donor-acceptor pair transitions (D_0, A_0), because they turn into free electron-acceptor transitions (e, A_0) when the donors become thermally ionized. For temperatures between 30 K and 100 K, Thonke *et al.* [71] reported very similar behavior for a DAP at 3.220 eV. It was found that with increasing temperature the intensity of the DAP decreased in favor of an adjacent line at 3.236 eV, resulting from a band-acceptor transition. The acceptor binding energy can be calculated according to eq. 3.8 in chapter 3.3. Assuming the deduced donor binding energy of 54.9 meV represents the energy of the dominant donor in the samples, the binding energy of the involved nitrogen acceptor can be estimated in agreement with the results of Zeuner *et al.* [68] to be of the size of 165 meV.

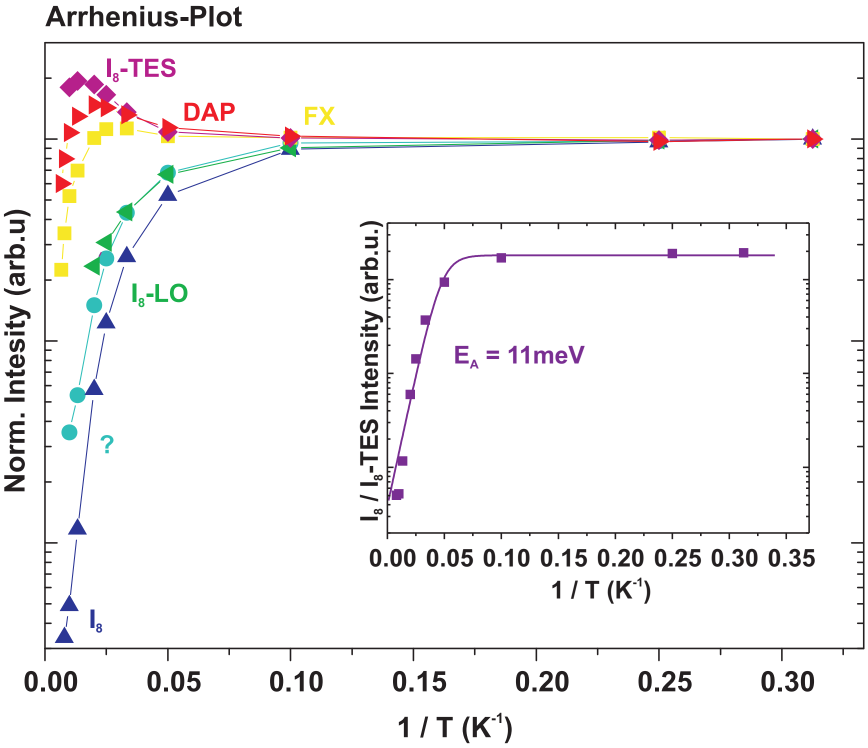

Figure 6.12: Arrhenius plot of thermally activated luminescence centers in nominally undoped ZnO. The spectra were provided by the group of J. Christen, Magdeburg.

The evaluation of an Arrhenius plot, as described in chapter 3.4, provides a convenient method to determine the thermal activation energy of the different luminescence centers. Fig. 6.12 displays the normalized intensity of the observed luminescence lines in the nominally undoped ZnO sample as a function of the reciprocal temperature. For the bound exciton transitions and their phonon replica, a significant decrease in the luminescence intensity is found for temperatures higher than 10 K. On the other hand, the free exciton, DAP, and TES luminescence gets thermally activated for an increased temperature and shows the strongest luminescence at values between 30 K and 75 K.

The encapsulated graph on the right side of Fig. 6.12 displays the PL intensity of the I_8 line divided by the intensity of the associated TES. Fitting of the acquired data points delivers the thermal activation energy, which is determined to be 11 meV in the case of the donor bound I_8 complex. This value is exceptionally small compared to previous reports on the thermal activation energy of this complex. Considering the discussed thermalization behavior in magneto-optical PL studies of the I_8 line, as well as the low thermal activation energy, it can be concluded that the I_8 line in the investigated ZnO sample shows an anomalous behavior compared to common undoped ZnO samples, for which the I_8 line was recently reported to be related to recombinations of excitons bound to gallium shallow donor complexes. [24,134,135].

6.4 Deeply Bound Excitons at Structural Defects

The spectra of Fig. 6.13 shows the photoluminescence of the arsenic doped ZnO specimen (MD2715) in the near bandgap regime and has been recorded at 2 K without an external magnetic field.

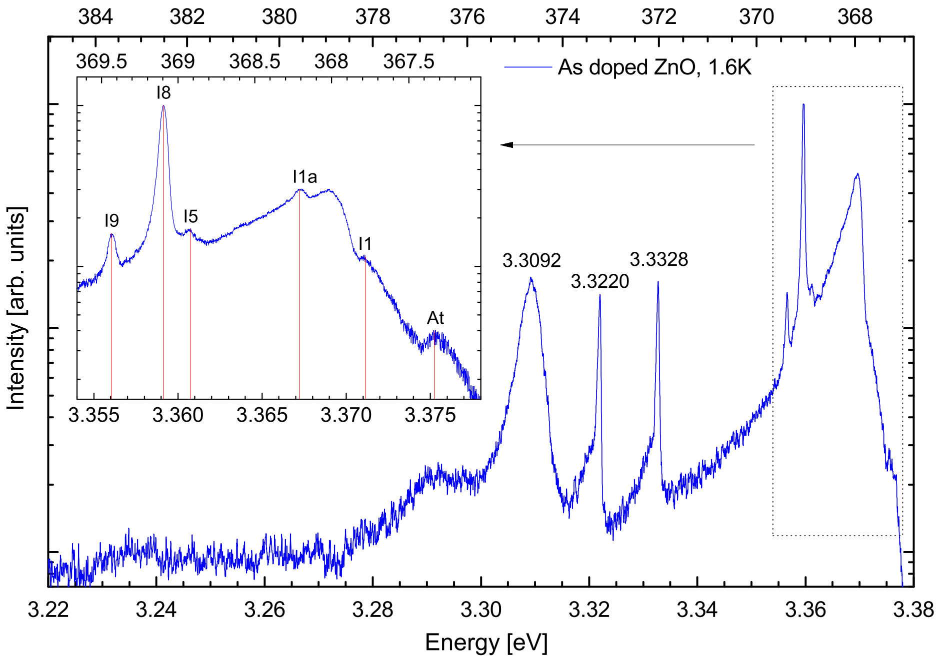

Figure 6.13: Near bandgap PL of As doped ZnO at 1.6 K. Left: Enlarged view of the excitonic regime. The positions of the free and bound exciton transitions are indicated by the vertical drop lines.

In the smaller left graph, the range of the free and bound exciton recombination lines is displayed in higher resolution. Clearly, the I_8 can be identified as the most dominant exciton line. Furthermore, the bound exciton lines I_9, I_5, I_{1a}, and I_1 as well as the transversal A free exciton A_T can be observed. From the comparison of the recorded line positions with the energy values for relaxed bulk ZnO given in table 3.1, a red shift of all transition lines by 660 μeV is found. This indicates the presence of minor tensile strain in the specimen.

By extending the range of the luminescence spectra, three additional peaks at energies of 3.3092 eV, 3.3220 eV, and 3.3328 eV can be identified in the main window of Fig. 6.13. The line at 3.3092 eV is attributed, by its temperature dependent intensity and shifting behavior (not shown), to a band acceptor (e, A^0) transition, which is possibly involving an As acceptor [142]. Calculating, with the bandgap energy of 3.437 eV at 2 K, a binding energy for the acceptor involved in the (e, A^0) transition, a value of approximately 128 meV can be derived. This value is in very good agreement with the reported As-acceptor ionization energy of 130 meV by Ryu *et. al* in arsenic doped ZnO grown by hybrid beam deposition [40].

With regard to the lines at 3.3220 eV and 3.3328 eV, it is suggested that the observed transitions may result from deeply bound excitons at structural defects. Dean [143] first reported similar luminescence peaks (Y and Z-lines) in ZnSe that are caused by localized recombinations within extended defects, involving a non-central force electronic system. In particular, a strong intensity of these lines could be observed in the vicinity of hetero-epitaxial interfaces in CVD grown samples as well as cut bulk samples. Fast and exponential decay times furthermore indicate that no correlation to the much slower and non-exponential DAP recombination mechanism exists. In addition, the Huang-Rhys parameter, describing the coupling strength to LO phonons, was found to be exceptionally weak in relation to their spectral position below the band gap [143]. Furthermore, Kutrowski *et. al* [144] recently performed a substantial analysis of the dislocation related Y and Z lines in ZnSe by means of μ-PL which gave rise to new questions regarding the origin and properties of structural defect related luminescence.

Equivalent observations of excitonic recombinations at structural defects have also been reported by other authors in the material systems of ZnTe, CdTe, CdS, and GaN [145–149]. Naumov *et. al* [145] discovered the intensity of Y-emissions in ZnTe epilayers to be a function of the lattice mismatch between layer and substrate and concluded that the observed luminescence is related to recombinations of excitons bound to extended structural defects, which should be represented by misfit dislocations. Similar transition lines were found in CdTe, which have been attributed to excitons bound at structural defects such as twins, dislocations or stacking faults [146]. In addition, Hoffmann and Gutowski [147, 148] performed cathodoluminescence wavelength imaging and magneto-optical Zeeman studies on

CdS specimen. They were able to identify several luminescence lines as originating from defect bound excitons associated with screw dislocations and map the spatial distribution of the dislocation related luminescence. The Zeeman splitting of these lines was found to be rather isotropic in contradiction to the usual anisotropy for recombinations at point defects under the influence of the localized crystal field. It could be concluded that the observed emission lines are related to deep excitons bound to dislocations, from which two lines exhibited an ionized-donor-complex like behavior.

A theoretical description for dislocation bound excitons in II-VI semiconductors was developed by Rebane, Schreter and Steeds [150–153], which assumes that the exciton forming carriers are bound to a dislocation by its strain field. Within this model, it was possible to derive the influence of the deformation potential on the exciton for screw dislocations as well as Taylor-Orowan dislocations. A substantial discussion of dislocation bound excitons in II-VI semiconductor heterostructures can be found for example in [154] and references within.

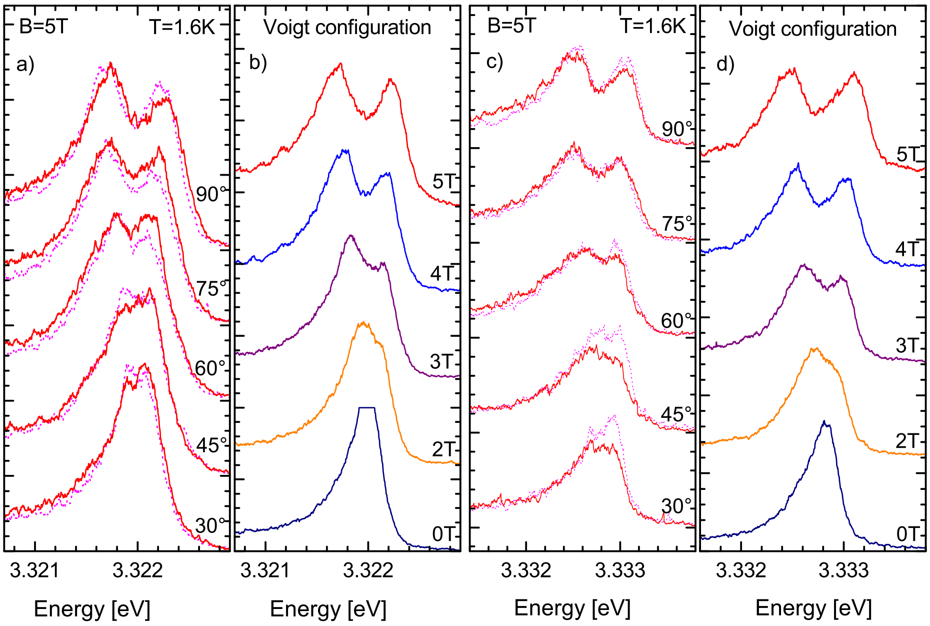

Figure 6.14: Magneto-optical PL of the deeply bound exciton transitions at 3.3220 eV and 3.3328 eV in arsenic doped ZnO at 1.6 K.

Deeply bound exciton luminescence related to extended structural defects has also been reported for epitaxial ZnO and ZnO nanowires [24,138,155–157]. However, publications on this subject are seldom and a convergent picture of their attribu-

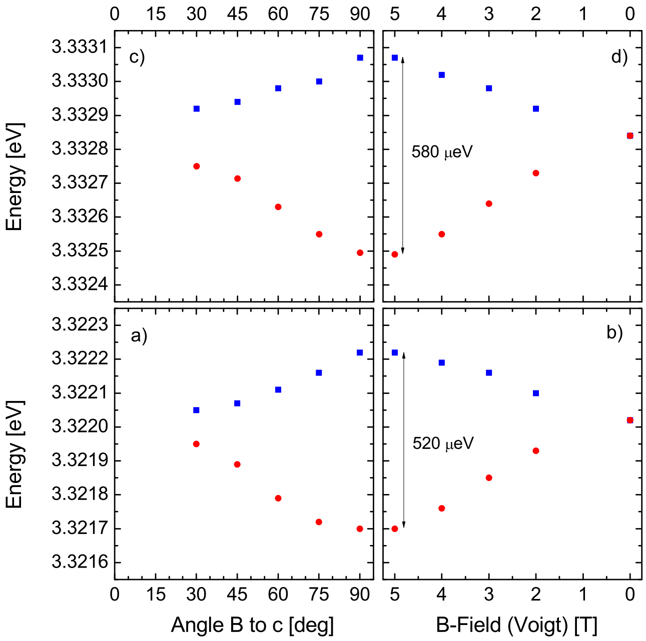

Figure 6.15: Shifting of the Zeeman compounds of the deeply bound exciton transitions 3.3220 eV and 3.3328 eV in arsenic doped ZnO at 1.6 K.

tion to particular extended structural defects has not yet emerged. Nevertheless, cathodoluminescence with its high spatial resolution has enabled the forthcoming of several interesting investigations concerning the spatial distribution of dislocation related luminescence centers. Meyer *et. al* [24] reported a transition line at 3.333 eV that could be attributed to the recombination of an excitonic complex with an activation energy of 10 meV, due to its temperature dependent PL and rather fast decay behavior. It has been suggested, that this transition may result from deeply bound excitons at structural defects, which is supported by the spot like and localized character of the luminescence band.

In order to support the assignment of the lines at 3.3220 eV and 3.3328 eV to deeply bound excitons (DBX) at structural defects and to analyze the donor or acceptor behavior of the defect complex, magneto-optical photoluminescence and temperature dependent measurements were performed. Although the observed transition lines in the PL spectra have not been recorded in any of the other investigated undoped or nitrogen doped ZnO samples, similar peaks could be identified in recent measurements of different ZnO specimen performed by Strassburg *et al.* and are discussed in combination with the results of the As doped ZnO specimen.

The magneto-optical PL spectra of both DBX recombination lines with $\mathbf{B}\|c$ as well as for arbitrary angles are presented in Fig. 6.14. The graphs on the left side (a, b) show the spectra for the lower energy peak at 3.3220 eV, which is labeled DBX_2, while the higher energy line at 3.3328 eV (DBX_1) is displayed on the right side of the graphic (c, d). In addition, the red solid lines for arbitrary angles indicate a polarization direction of σ^+ and the dotted magenta lines represent the spectra with selected σ^- polarization. With increasing magnetic field, it is obvious that both exciton lines exhibit a Zeeman splitting into two components (b, d). For a field strength of $B = 5$ T, the intensity of these two Zeeman components is found to be of equal size. This observation applies for DBX_1 as well as for DBX_2. Since the thermalization behavior for emission depends on the splitting of the complex excited state (as previously discussed), the absence of a magnetic thermalization suggests that no exited state splitting is present.

From the angular dependent spectra, no clear evidence for a different behavior depending on the polarization direction can be derived. However, it is noticeable that compared to the previous Zeeman studies of the I_8 in nominally undoped ZnO (chapter 6.2), the weakly forbidden Zeeman components, which could be observed for arbitrary angles at lower and higher energies of the two main components, are not present in the DBX spectra.

The peak positions of the Zeeman components determined by fitting of the photoluminescence spectra by Gaussian peaks are displayed in Fig. 6.15. From the linear splitting in $\mathbf{B}\|c$ with increasing magnetic field, it can be deduced that both DBX lines should result from excitons bound to neutral defect complexes. For an ionized complex, a nonlinear splitting of the components would be expected, as has been reported for dislocation bound excitons in CdS [148]. The size of the Zeeman splitting in Voigt configuration at a magnetic field strength of five Tesla is found to exhibit a deviation for the two different exciton lines (graph b and d). The DBX_1 peak at 3.3328 eV shows a splitting of 580 μeV, while the distance of the Zeeman components at 5 T for the DBX_2 line at 3.3220 eV is of the size of 520 μeV.

Apparently, this difference is also present in the angular dependent data, for which a smaller splitting of the DBX_2 line at a certain angle can be observed compared to the Zeeman splitting of the DBX_1. Hence, different g-values for the two exciton complexes should be decisive. However, according to the theoretical considerations of Rodina *et. al* [90], both bound exciton complexes appear to involve holes from a valence band state with Γ_7 symmetry, since for the involvement of hole states with Γ_9 symmetry, a crossing of the Zeeman components for smaller angles between $\mathbf{B}$ and c would be expected.

Temperature dependent PL spectra of the DBX range were recorded in order to support the donor complex like behavior that is suggested by the intensity evolution of the Zeeman components in Voigt configuration. Fig. 6.16 shows the luminescence

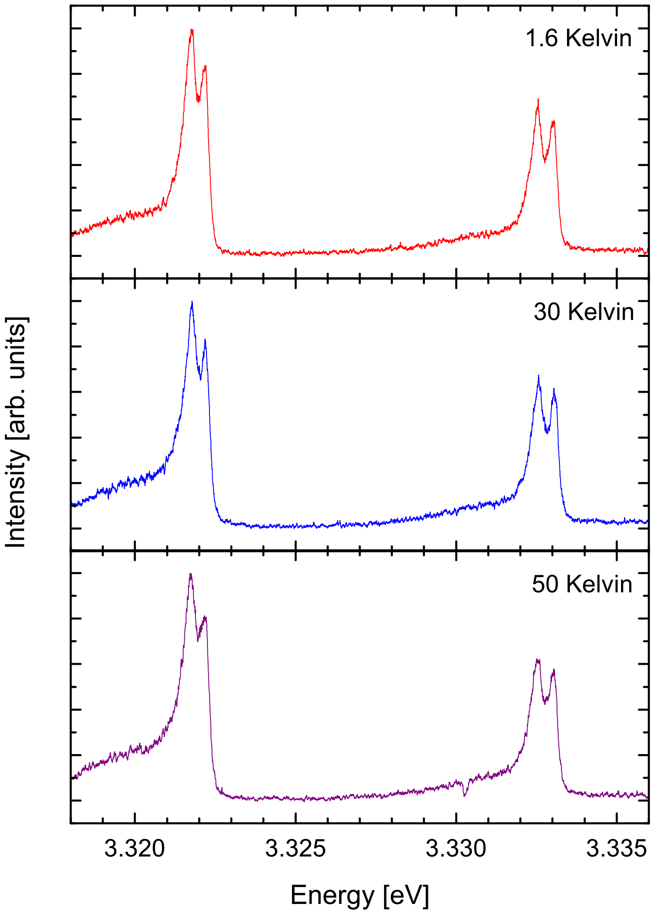

Figure 6.16: Temperature dependent PL of deeply bound excitons in arsenic doped ZnO. The measurements were performed at a magnetic field of 5 Tesla perpendicular to the crystal c-axis.

at temperatures of 1.6 K, 30 K, and 50 K. Evidently, no significant changes in the peak intensities of the two Zeeman components with increasing temperature can be reported. This corresponds to the expectations for a donor bound exciton complex with a split ground state (D^0) that is determined by the electron effective g-value g_e. Hence, the influence of an increasing temperature on the intensity ratio of the Zeeman components could only effect the excited state, who's splitting is given by $g_h^{\perp} \approx 0$ and therefore negligible small.

Interestingly, no energetic shift of the excitonic lines with increasing temperature up to 50 K can be observed. Such a behavior supports the assignment of excitons bound to deep defect states, since shallow levels are well known to shift with the bandgap. In addition, the missing quenching of the lines indicates a relatively large

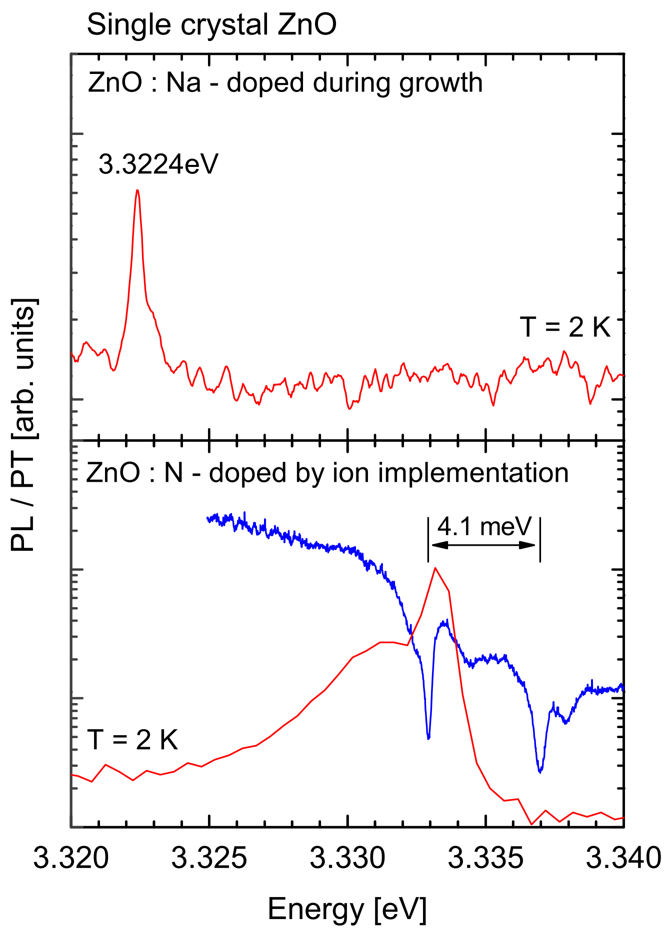

Figure 6.17: Deeply bound exciton PL and Absorption in N ion implanted and Na doped ZnO single crystals at 2 K.

thermal activation energy compared to reported values of 11 meV for the 3.335 eV line by Alves *et. al* [138] and the 10 meV for the 3.333 eV line by Meyer *et. al* [24].

The presented results for neutral donor bound exciton recombinations at extended structural defects in arsenic doped ZnO epilayers are now compared with photoluminescence and absorption spectra from single crystals. As shown by the presence of DBX peaks in bulk ZnO samples, the occurrence of these lines is not only restricted to heteroepitaxial films with induced dislocations due to the lattice mismatch between different layers, but can also appear in single crystals [24]. In particular, additional defects in single crystals can be introduced by cutting, polishing or etching processes, giving rise to new localized luminescence centers, related to structural defects close to the surface. Furthermore, ion implementation can also, besides the usually intended doping by impurity atoms, lead to the creation of new structural defects, which may serve as radiative recombination centers [149].

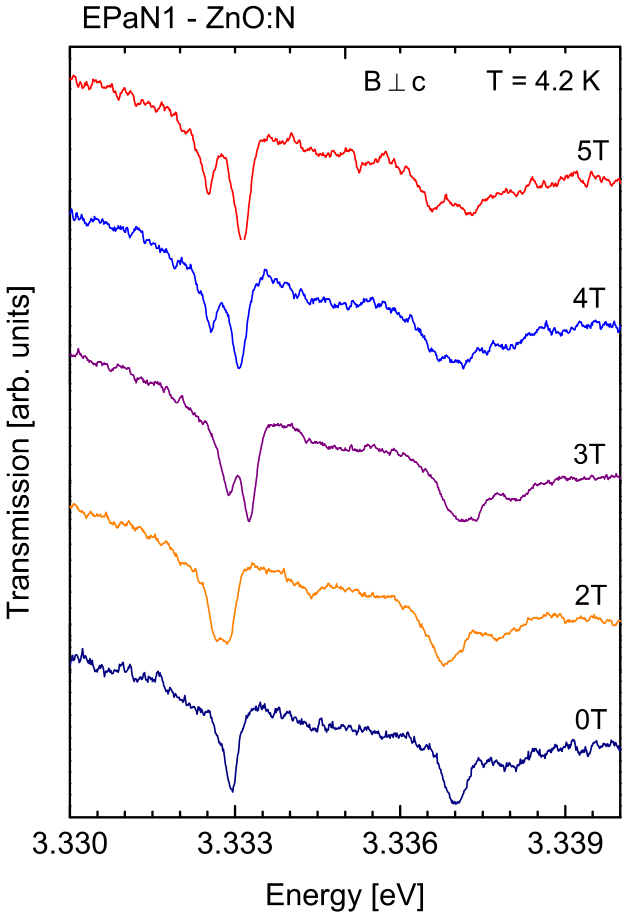

Figure 6.18: Deeply bound exciton absorption of N implanted ZnO single crystals in external magnetic fields. The spectra were recorded in Voigt configuration with field strengths between 0 T and 5 T at 4.2 K.

Fig. 6.17 shows the luminescence and absorption of ZnO single crystals, which exhibit similar transition lines in the range of 3.32-3.34 eV, as they were found in the arsenic doped ZnO epilayers. All spectra were recorded at a temperature of 2 K without external magnetic field. The upper graph of Fig. 6.17 displays the PL signal of an bulk ZnO specimen that was doped with sodium (Na) during the growth process at the University of Erlangen. At an energy of 3.3224 eV, an emission line can be observed, which energetic position and linewidth is consistant with the DBX$_2$ peak in the As doped samples. However, at the position of the DBX$_1$ line in the arsenic doped specimen, no luminescence peak can be observed in the ZnO:Na crystal. It is thereby apparent that the occurrence of the two peaks are not necessarily correlated and seem to be independent of the specific growth process or doping.

This conclusion is further supported by the transmission and photoluminescence spectra of a nitrogen doped ZnO single crystal, which are presented in the lower graph of Fig. 6.17. The ZnO crystal was produced by EaglePitcher and subsequently doped with nitrogen by ion implementation. In the transmission spectra, two well separated absorption lines at 3.3329 eV and 3.3370 eV can be identified. The peak at 3.3329 eV, which is also found in the PL spectra, is in excellent agreement with the energetic position of the luminescence line in the arsenic doped samples (DBX_1). Furthermore, the full-width at half-maximum (FWHM) with values of $200-300$ μeV matches well for the absorption and emission spectra in the two different samples. Therefore, it can be assumed that these two lines are related to similar defects. The presence of the transition line in the absorption spectra further excludes the unlikely possibility of the DBX_1 line originating from two electron satellites.

The absorption spectra of the nitrogen doped ZnO single crystals in external magnetic fields between 0 T and 5 T are presented in Fig. 6.18. All spectra are recorded in Voigt configuration at a temperature of 4.2 K. For the lower energy transition at 3.3329 eV, the splitting with increasing magnetic field into two Zeeman components is clearly visible. The energetic separation of these two lines at 5 T is found to be of the size of of 580 μeV, which is in excellent agreement with the observed splitting in the photoluminescence spectra of the arsenic doped ZnO specimen.

From the intensity ratio of the two Zeeman components of the peak at 3.3329 eV, it is obvious that the lower energy component decreases in intensity with increasing magnetic field compared to the higher energy component. The observed magnetic thermalization behavior provides additional evidence for the attribution of the bound exciton complex to be donor related. This is, because the thermalization in absorption depends on the splitting on the ground state, which is only present assuming a $\Gamma_7 \rightarrow \Gamma_7$ transition for a donor bound exciton complex (Fig. 6.1).

The magnetic thermalization of the second absorption line at 3.3370 eV is ambiguous and the small intensity of the absorption peaks makes a doubtless statement difficult. Nevertheless, it appears that the magnetic thermalization which is particularly strong at a magnetic field of $B = 5$ T for the 3.3329 eV line is not present for the 3.3370 eV absorption. Hence, the two components show a similar intensity. This can only be explained if the complex ground state, which is decisive for the thermalization in absorption, does not exhibit a significant splitting. For $\mathbf{B} \perp c$, this is only true for an exciton bound to an acceptor complex involving either a hole state with Γ_7 or Γ_9 symmetry. However, due to the uncertainty caused by the small intensities, the assignment to an acceptor complex can not be doubtlessly confirmed.

The less intense absorption in the nitrogen doped single crystals at 3.3370 eV

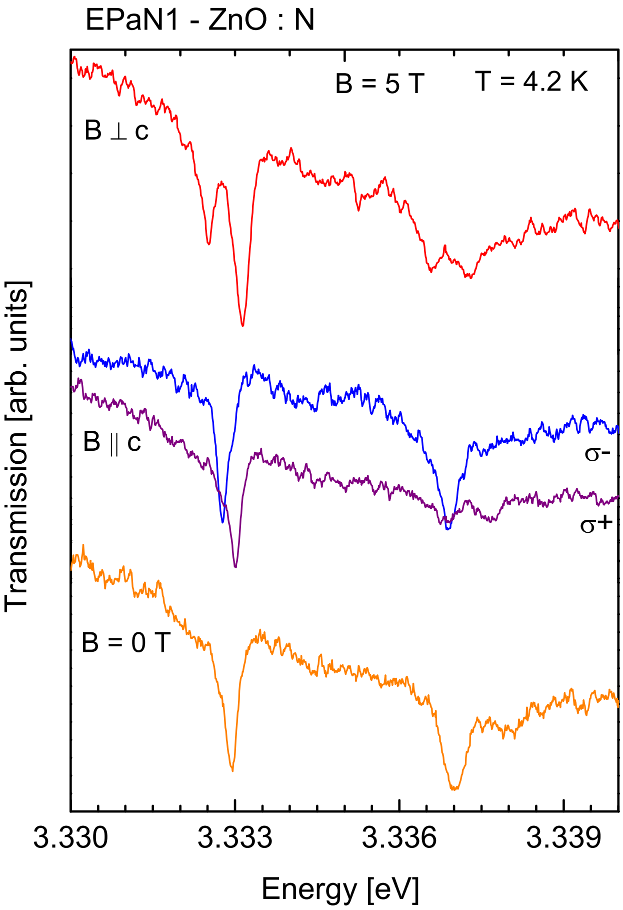

Figure 6.19: Magneto-optical transmission spectroscopy of deeply bound excitons in N implanted ZnO single crystals. Top: $\mathbf{B} \perp c$ at 5 T, center: $\mathbf{B} \| c$ at 5 T with polarization directions σ^+ and σ^-, zero-field transmission. All spectra a recorded at a temperature of 4.2 K.

is separated from the other transition peak at 3.3329 eV by an energy of 4.1 meV. This value is close to the energetic difference of the A and B valence subbands at the Γ-point in ZnO with a size of 4.9 meV (chapter 2.4.3). Therefore, it might be possible that the higher energetic absorption line results from a deeply bound exciton, which involves a hole from the B valence band. Thus, the involved hole state in the B valence band should possess Γ_9 symmetry. According to the considerations in chapter 6.2, this could be proven by a crossing of the Zeeman components for arbitrary angles, which would be expected for a exciton complex involving a hole from a Γ_9 state. Unfortunately, the Zeeman components for high magnetic fields are difficult to distinguish due to their small intensity and consequently no angular dependent measurements could be performed. However, absorption data in Faraday configuration might allow advanced argumentations (see below).

Fig. 6.19 displays the absorption lines for zero magnetic field (bottom), polarization dependent transmission in Faraday configuration at 5 T (center) and the transmission in Voigt configuration at 5 T (top) for a temperature of 4.2 K. Of particular interest should be the polarization dependent data for $\mathbf{B}\perp c$ configuration. Analogous to the PL results for the I_8 in nominally undoped ZnO (chapter 6.2), the splitting of the Zeeman components of the DBX$_1$ line is found to be smaller in $\mathbf{B}\|c$ than in $\mathbf{B}\perp c$. Furthermore, the higher energetic transition in Faraday configuration is active for σ^+ polarization, while the lower energetic position is active for σ^-. These results further suggest the involvement of a Γ_7 hole state in the bound exciton complex.

Concerning the transition line at 3.3370 eV, an energy separation of the two Zeeman components of approximately 620 μeV can be derived for a magnetic field of $B = 5$ T in Voigt configuration. Although slightly larger, this value can be taken as consistent with the previously observed splitting of 580 μeV of the DBX$_1$ transition within the given accuracy of measurements. However, the Zeeman splitting in Faraday configuration reveals a very different behavior to the peak at 3.3329 eV.

As usual, the lower energy Zeeman component at 5 T with $\mathbf{B}\|c$ is found to be active for the σ^- polarization, while for σ^+ polarization, a higher energy component can be observed that is not present in the σ^- spectra. For a magnetic field of 5 T, these peaks are found at energies of 3.3369 eV and 3.33765 eV, respectively. Therefore, an energy separation of 750 μeV can be calculated. This value is not only larger than the typical splitting in Faraday configuration, but also exceeds the observed size of the Zeeman splitting for $\mathbf{B}\perp c$. In addition, both Zeeman components for $\mathbf{B}\|c$ are located at higher energies than their respective energy components for $\mathbf{B}\perp c$.

Following the argumentation of Rodina *et. al* [90], the observed correlations can be explained for an exciton complex involving hole states of Γ_9 symmetry. Equivalent to the discussion in chapter 6.2, the Zeeman behavior of a donor bound exciton complex (D^0, X) depends on the splitting of the excited state, which is determined by the anisotropic hole effective g-value $g_h^{\|}$, as well as the splitting of the ground state (D^0), that is given by the electron effective g-value g_e. For an acceptor bound exciton complex, the relations are vice versa. However, for an involved hole state having Γ_9 symmetry, the anisotropic hole effective g-factor $g_h^{\|}$ is larger than g_e ($|g_h^{\|}| > g_e$) in contrast to the smaller absolute value of $g_h^{\|}$ for an hole of Γ_7 symmetry. Due to this larger anisotropic hole effective g-value, the σ^+ and σ^- transitions in $\mathbf{B}\|c$ are of higher energy than their respective transitions for $\mathbf{B}\perp c$ with the unsplit excited or ground states for donor or acceptor bound complexes, respectively.

In summary, it can be concluded that the absorption line at 3.3329 eV most likely results from a localized deeply bound exciton at a structural dislocation center, which exhibits a neutral donor complex like behavior and involves a hole state having Γ_7 symmetry. On the other hand, it is suggested that the 3.3370 eV transition, which also originates from a dislocation bound exciton complex, involves a hole from the B valence band possessing Γ_9 symmetry, while the defect complex might exhibit an acceptor like behavior.

Chapter 7

Results and Discussion of RF Magnetron Sputtered Samples

7.1 Introduction

The results of different experimental methods (chapter 5) that were applied to investigate the RF magnetron grown thin films are presented and discussed in this chapter. The fabrication and post growth annealing specifications of these samples were introduced in chapter 4.5 and 4.6. Firstly, the successful incorporation of transition metals by XPS and EDX is investigated. Secondly, the structural properties and the influence of annealing by XRD and SEM imaging are examined. Finally, the optical properties of doped specimens at different temperatures, determined by PL and CL spectroscopy are discussed and evaluated. The presented results within this chapter from the previously grown doped and undoped ZnO specimens were acquired, without exception, by myself. Except for the photoluminescence spectra, that were recorded at the Technical University Berlin, all measurements were performed at the University of Technology in Sydney.

7.2 X-Ray Photoelectron Spectroscopy

Surface analysis by x-ray photoelectron spectroscopy (XPS) was accomplished by irradiating a Co doped sample with mono-energetic soft x-rays emitted by the Mg K_α-line at 1253.6 eV. In Fig. 7.1, the relative intensity of the emitted electrons, as a function of the binding energy, is displayed with a resolution of 1 eV. The background originates from electrons that are emitted from ionized atoms deeper under the surface and undergo inelastic scattering processes before they emerge from the solid. The feature rich regions are measured at higher resolution with steps of 100 meV, and are displayed magnified and background corrected. The 0 eV level equals the Fermi energy. Several types of peaks can be observed in the XPS spectra. It is important to distinguish which are fundamental to the technique, result from instrumental effects or depend on the chemical nature of the sample and can provide information on the constituents.

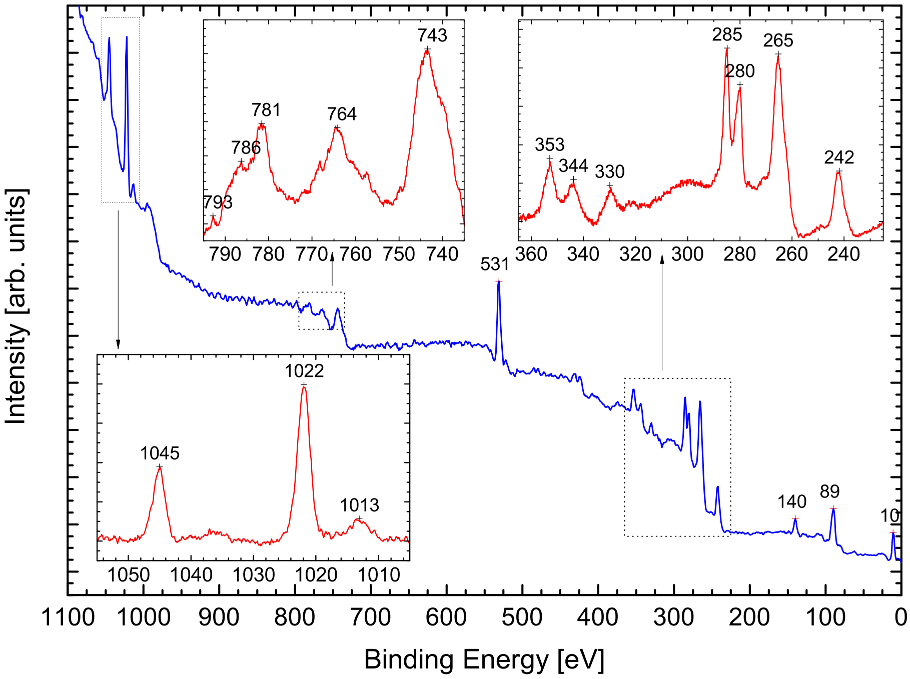

Figure 7.1: X-Ray photo-electron spectra of Co-doped ZnO. Three selected areas are displayed in higher resolution and background corrected.

The lines at 1045 eV and 1022 eV originate from zinc and exhibit the characteristic spin-orbit splitting of the 2p level with the typical intensity ratio of 1:2. However, the peak at 1013 eV does not naturally belong to Zn, but rather is an x-ray satellite that appears as a minor peak at lower binding energies, with intensity and spacing characteristic of the x-ray anode material. It is labeled α_3 with an energy displacement of 8.4 eV and a relative height to the main peak of 8.0 for a Mg x-ray tube. Further peaks associated with Zn are the 3s state at 140 eV, the $3p_{3/2}$ at 89 eV and the 3d peak at a binding energy of 10 eV.

Furthermore, several Auger lines associated with zinc can be identified. These lines occur, when an inner core vacancy, that was created by the emission of an photoelectron due to x-ray bombardment, is occupied by a higher orbital electron, and the transition energy is not emitted as a photon but rather non-radiatively used to ionize another electron. This electron is called an Auger electron and is independent of the initial ionization source. The Auger lines in the spectra form rather complex patterns, for example the $L_3M_{23}M_{45}(^1P)$ Auger line describes a process with an initial vacancy in a L3 = $2p_{3/2}$ state and two final vacancies in the M23 = $3d_{3/2}$ and M45 = $3d_{5/2}$ states. Most of the lines between 360 eV and 240 eV can be assigned to Zn Auger processes. In any case zinc, oxygen (1s at 531 meV), and carbon (1s at 285 meV) can be clearly identified by their photoelectron- and Auger lines. The table 7.1 lists all the observed main features together with their literature values, chemical origin and configuration. A shift of 3-4 eV to higher energies for the Zn Auger lines and a shift of 2 eV to lower energies for the O Auger lines is observed. The origin of these shifts still needs to be determined.

peak energy	energy (literature)	chemical identity	configuration
1045	1045	Zn	$2p_{1/2}$
1022	1022	Zn	$2p_{3/2}$
1013	1013	Zn	α_3 satellite
793	793	Co	$2p_{1/2}$
786	?	?	?
781	781	CoO	$2p_{3/2}$
	780	O	KL_1L_1
764	766	O	KL_1L_{23}
743	745	O	$KL_{23}L_{23}$
531	531	O	1s
353	349	Zn	$L_3M_{23}M_{45}(^1P)$
344	340	Zn	$L_3M_{23}M_{45}(^3P)$
330	326	Zn	$L_2M_{23}M_{45}(^1P)$
285	285	C	1s
280			
265	262	Zn	$L_3M_{45}M_{45}$
242	239	Zn	$L_2M_{45}M_{45}$
140	140	Zn	3s
89	89	Zn	$3p_{3/2}$
10	10	Zn	3d

Table 7.1: Assignment of the observed transition lines in XPS to their chemical identity and electronic configuration. The measured energy values are compared with the known values from the literature.

Of particular interest in terms of the doping process is the region between 800 eV and 770 eV, since cobalt is known to exhibit the most intense $2p_{3/2}$-line at 778 eV and the $3p_{3/2}$-line at 793 eV. However, the identification of these lines is difficult due to different reasons. Firstly, oxygen is known to exhibit the lowest intensity KL_1L_1 Auger line at 780 eV although following the observed shift of the other O Auger lines, this line is expected to appear at 788 eV, which is exactly the energy of the $2p_{3/2}$-line of cobalt. Although there is no evidence in the spectra, an overlapping influence with O Auger lines can not completely ruled out. Secondly, there is a very small peak at the position of the $2p_{1/2}$-line at 793 eV, but the missing of the more intense $2p_{3/2}$-line indicates that this might be an artifact.

The influence of chemical compounds on the position and shape of the Co lines in XPS spectra is of great significance. Epitaxial CoO films with a Co^{2+} charge state and Co_2O_3 films with a Co^{3+} charge state are known to show a shift of around 3 eV of the $2p_{3/2}$-line to higher energies and a noticeable line broadening compared to atomic polycrystalline cobalt metal film (Co^0). These characteristics are consistent with the observed peak at 781 eV.

On the high energy side-band at 786 eV another peak can be recognized. However, a definitive assignment is not straightforward. One possibility is the appearance of a shake-up line. These lines result from photoelectrons emitted by ions that were left in an excited state rather than the ground state, which reduces the emitted energy of the electrons and leads to the formation of a satellite peak a few electron volts lower than the main peak. Assuming the attribution to a shake up line is correct, the data indicate that cobalt is likely to be present in the 2^+ oxidation state, since Co_2O_3 films with cobalt in the 3^+ oxidation state usually do not exhibit shake up lines. This assignment is also supported by the results of XPS measurements reported by Tuan *et al.* [158].

As discussed in chapter 2.3.2, a high solubility of impurity atoms, as it was reported for Co in ZnO by Jin et. at. [159], naturally requires a close conformity of the ionic radii. It is therefore expected that Co^{2+} occupies Zn^{2+} sites in the ZnO lattice since their ionic radii differ by only 10% and the EDX data in chapter 7.3 only show a relative decrease of the Zn concentration with increasing Co, while the relative O level remains constant. Hence, Co is likely to be incorporated in the Co^{2+} charge state, however, further investigations would be necessary to support this assignment.

Silicon as a substrate material is, as expected, not present in the photoelectron spectra. Although there is a high probability that silicon atoms become ionized by the x-ray photons, the mean free path (tens of amstrongs) of the emitted electrons is significantly too small to pass through the 300-500 nm thick ZnO layer and therefore cannot contribute to the spectra (chapter 5.7).

To summarize the analysis, all major feature of zinc, oxygen and carbon could be identified. Cobalt is likely to be present at the surface of the sample and the spectra indicate that it might be dominant as CoO. However, a quantitative analysis is not possible and further experimental methods need to be applied in order to determine the concentration and successful incorporation of Co in ZnO during the magnetron sputtering process (chapter 7.3).

7.3 Energy-Dispersive X-Ray (EDX) Analysis

In order to determine the amount of successfully introduced transition metals and the dependence of the sputter power on the dopant concentration in the ZnO samples, standardless quantitative energy dispersive x-ray analysis (chapter 5.8) using a scanning electron microscope (chapter 5.9) is performed. Fig. 7.2 shows the relative intensity of the detected x-rays that originate from the irradiation of the sample with a 15 kV primary electron beam as a function of the emitted x-ray photon energy. Four cobalt doped zinc oxide sample that were sputter with different DC sputter power in argon and oxygen atmosphere are investigated.

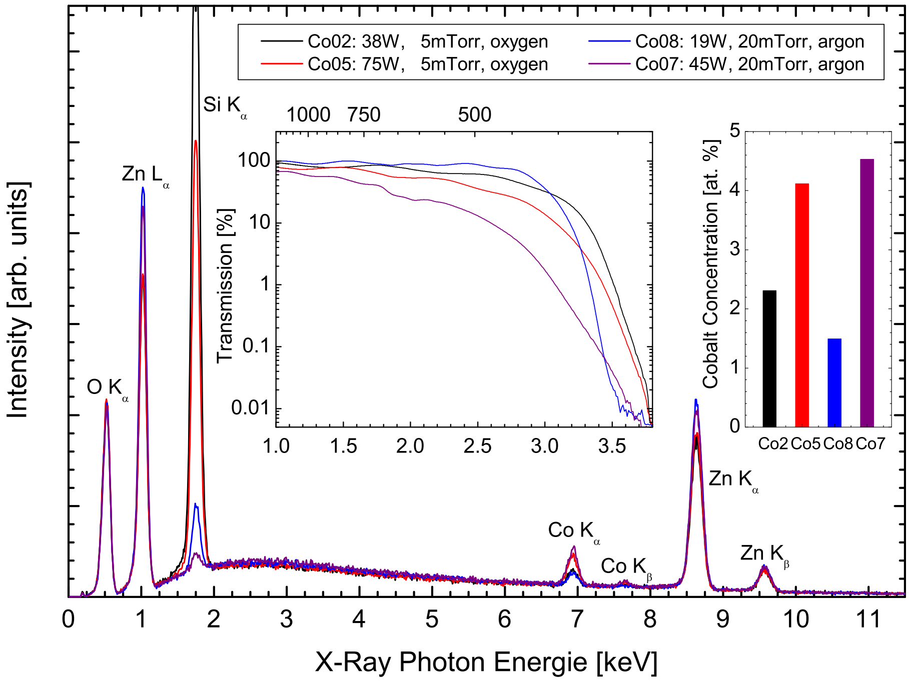

Figure 7.2: EDX spectra of cobalt doped ZnO specimen grown in an argon and oxygen atmosphere. The Co concentration is determined by standardless quantization of the EDX data (right graph). In addition, the transmission at 300°C for the Co doped samples is displayed in the encapsulated center graph.

Several peaks can be clearly identified and associated with the characteristic K and L lines of different chemical elements. K lines occur as result of transitions from electrons of the L or M shell to a K shell vacancy (K_α respective K_β) while L-lines appear, when a vacancy of the L shell is occupied due to a transition from a higher orbital. An analysis of the peak position results in the well-defined attribution of the strongest peaks to oxygen ($K_\alpha(O) = 520$ eV), silicon ($K_\alpha(Si) = 1.75$ keV) and zinc ($K_\alpha(Si) = 8.63$ keV). Furthermore, the Co K_α and K_β lines at 6.94 keV and 7.64 keV, respectively, indicate the presence of cobalt in the samples.

A comparison of the intensity of the Si K_α line reveals a significant difference in the detected Si concentration of more than one order of magnitude for the different samples. This effect originates from the varying film thickness of the specimen. The kinetic energy of ionized argon atoms exceeds those of oxygen, thus leading to a highly efficient sputter process. Since the sputter time for all Co doped ZnO samples was kept constant at 100 min, the samples grown under pure argon atmosphere show a substantially larger film thickness. Similar considerations apply for higher sputtering power. The electron beam for the thin film specimen Co02 (low sputter power, oxygen atmosphere) thus easily penetrates the surface layer, resulting in a strong silicon peak from the substrate. On the other hand, the EDX spectra of a sample with a factor of three larger film thickness, resulting from higher sputter power in argon atmosphere (Co07), only exhibits a very small x-ray peak from the substrate.

The results of a quantitative analysis of the Co concentration are visualized in the right graph of Fig. 7.2 which shows the relative quantity of Co in atomic percentage within the ZnO film for the different sputtered samples. In order to determine the concentration of Co in the thin film correctly, the influence of the substrate peaks in the EDX spectra on the concentration has to be excluded. Therefore the Si peak is not taken into account.

The results show that Co was successfully introduced up to a concentration of 4.5 atomic percentage in oxygen as well as argon atmosphere and the Co concentration increases with higher sputter power of the cobalt target. In addition, it is obvious that a smaller sputtering power in argon atmosphere is sufficient in order to obtain a similar Co concentration as it is in oxygen. The relative dopant concentration within the investigated concentration range seems to scale linearly with an increase in the cobalt target sputter power. However, this has to be verified by a more detailed analysis of a larger sample set (chapter 7.4).

The center graph in Fig. 7.2 visualizes the optical transmission as a function of photon energy for the four investigated Co-doped ZnO samples. The absorption edge is found to be steeper for low cobalt concentrations. The very low transparency of less than ten percent down to a photon energy of 2.6 eV for the heavily doped Co07 sample may also be supported by the larger film thickness, thus leading to a smaller intensity of the transmitted light. The undulated transmission intensity that is visible in the range of 1 eV to 2.6 eV results from Fabry-Perots and is therefore a thin film effect that is not directly correlated with the doping, but can also be observed in plain ZnO thin films.

In conclusion, the quantitative analysis of the EDX spectra suggests that Co is present in the ZnO samples with a concentration of 1.5 to 4.5 atomic percentage and that the cobalt concentration depends on the used sputter atmosphere as well as the applied DC sputter power.

7.4 Influence of Sputter Power on Dopant Concentration

A set of chromium doped ZnO samples was grown by RF magnetron sputtering with constantly increasing sputter power of the transition metal target to investigate the influence of the Cr concentration on the optical properties. The analysis of the incorporated Cr concentration also allows a convergent picture of the dopant concentration in dependence on the sputter conditions to be drown. All samples were grown with 75 W RF power at an ambient pressure of 5 mTorr in a pure oxygen atmosphere. The chamber vacuum was as good as $5 \cdot 10^{-6}$ mTorr. The silicon substrate was mounted on a rotating stage at a distance of 100 mm from the RF powered ZnO source and 25 cm from the DC powered Cr source. The sputtering time for the samples was 150 min. Table 7.2 contains the varying data for the DC power at the Cr target.

sample	I [A]	U [V]	P [W]
Cr04	0.05	340	17
Cr01	0.10	370	37
Cr02	0.15	400	60
Cr03	0.20	440	88
Cr05	0.25	450	112
Cr06	0.30	460	138
Cr07	0.35	470	165
Cr08	0.40	490	196
Cr09	0.45	510	230
Cr10	0.50	530	265

Table 7.2: Sputter deposition data for Cr doped ZnO specimen. Applied DC current (I), voltage (U) and output power (P) of the chromium sputter diode are denoted.

The chromium concentration as a function of sputter power is displayed in Fig. 7.3. Under the sputter conditions described above, a relative Cr concentration of five percent for the maximal sputter power of 265 W could be calculated from EDX measurements. The excellent agreement of the experimental data with a linear fit demonstrates that at least up to five atomic percentage, there is indeed a proportional scaling of the transition metal incorporation with the applied sputter power. The almost constant relative oxygen concentration and decreasing relative zinc concentration further indicate that the chromium atoms preferably occupy zinc sites in the lattice.

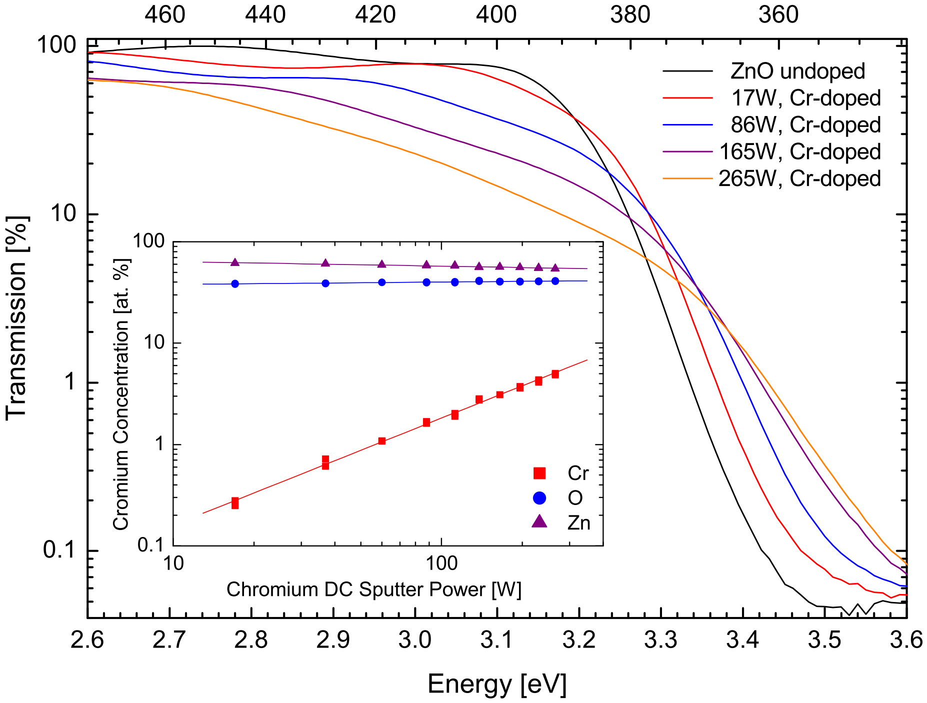

Figure 7.3: Shifting of the optical absorption edge with increasing sputter power for the chromium target. The lower left graph shows the concentration dependence on the sputter power.

In addition, the results of transmission spectroscopy measurements of four selected Cr-doped samples and an undoped ZnO reference sample are illustrated in Fig. 7.3. Starting from the undoped sample to the maximum Cr concentration, the steepness of the absorption edge is not only constantly decreasing, but the energy for which the transmission is reduced to 1 % also shifts from initially 3.33 eV to 3.43 eV at room temperature. According to Burnstein and Moss [160, 161], a blueshift of the absorption edge can be explained for heavily doped semiconductors by the band filling of the lowest energy electron- and hole states, thus enabling transitions with larger energies. Hence, the observance of a Burstein-Moss shift indicates an increase in carrier concentration. Concerning ZnO, Roth *et al.* [162] found the described behavior to apply for carrier concentrations up to $3 \cdot 10^{19}\text{cm}^{-3}$. Therefore, it is likely that the chromium doping increased the free carrier concentration in the sputter specimen, however, no Hall measurements were performed to finally address this issue.

7.5 Structural Properties

Up to now, the chemical constituents of the doped ZnO films, the influence of sputter conditions on the achievable dopant concentration and the effects on the optical transmission were investigated. However, a structural analysis of the samples is required to evaluate the quality of the grown films. In particular, the effect of subsequent annealing on the film structure needs to be examined. Therefore, x-ray diffraction spectroscopy (chapter 5.6) and scanning electron microscopy measurements (chapter 5.9) were conducted.

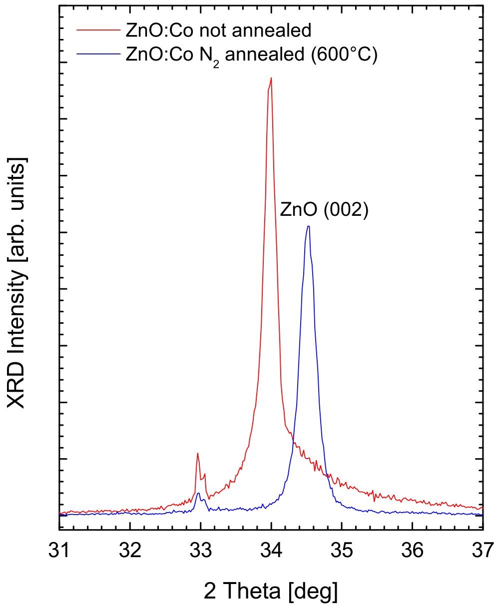

Figure 7.4: XRD $\theta - 2\theta$ scan of Co-doped ZnO on Si (001) substrate with a cobalt concentration of 4 at. %. The two different graphs show the XRD spectra before and after annealing in nitrogen excess atmosphere at 600°C for 60 min.

The x-ray diffraction pattern for Co-doped ZnO with a cobalt concentration of 4 at. % in Fig. 7.4 exhibits a strong peak, that can be attributed to the ZnO (002) plane. In addition, some selected samples also showed the appearence of very weak ZnO (101) and (102) peaks at $2\theta = 36.2°$ and $47.5°$ respectively, which is in good agreement with reports of other researchers on sputtered ZnO films on silicon substrate [122, 163, 164]. However, these peaks did not increase noticeably from the background, nor are they present in the Co doped sample and will therefore not be further discussed. The peaks at 32.96° and 33.04° can be attributed to the silicon substrate and hence are not directly associated with the doped ZnO film. The specimens were found to show a polycrystalline structure and a preferential orientation [001] with the c-axis perpendicular to the silicon substrate surface (001). This is in agreement with results of Fujimura *et. al* [165], who reported, that sputtered ZnO thin films were generally polycrystalline and show the observed preferential orientation due to the lowest surface free energy of the (002) plane in ZnO.

After annealing the sample at 600°C for 60 min in nitrogen excess atmosphere, the largest peak clearly shifted from its initial position at 33.98° to an angle of 34.52°. This is close to the (002) angular peak position of ZnO powder with $2\theta = 34.421°$ [166]. The deviation of the diffraction peak from its powder value is usually caused by a uniform state of stress as a consequence of the different lattice constants of substrate and film. A smaller diffraction angle thereby indicates the presence of compressive stress, while a larger angle suggests tensile stress to be prevailing. The stress in sputtered ZnO films has been investigated by various groups and associated with the formation of interstitial oxygen due to the impact of the sputtered atoms [167,168].

Several researchers reported a relief of stress in ZnO sputtered thin films on silicon substrate with an increase of the postannealing temperature, indicated by a shift of the diffraction peak towards the peak position of ZnO powder. However, for too high temperatures the difference in the thermal expansion coefficient of ZnO, being higher than that of silicon, will lead to the predominance of tensile strain, implied by the shifting of the diffraction peak to higher angles than found for the powder [123]. Therefore, it can be concluded, that the investigated cobalt doped ZnO specimens seem to exhibit compressive stress, which is turned into minor tensile stress after annealing at high temperatures.

Furthermore, it can be noticed, that the halfwidth of the (002) diffraction peak is increased from 0.16° for the not annealed sample to 0.20° for the nitrogen annealed one. By applying the Scherrer formula

$$D = \frac{0.9\lambda}{B\cos\theta} \tag{7.1}$$

the average grain size D of the polycrystalline film can be determined, with $\lambda = 1.54$ Å being the x-ray wavelength of the used Cu K_α line, θ the Bragg diffraction angle and B the full-width at half-maximum (FWHM) of the ZnO (002) diffraction peak. The mean grain size is then determined to be 91 nm and 73 nm for the samples before and after annealing, respectively. However, the increase of the FWHM after annealing is in contradiction to the usual behavior of ZnO films on silicon substrate, which does not only indicate a reduction in grain size, but also an increase in stress. It is suggested, that although the stress caused by the deposition on the silicon substrate is reduced by annealing in high temperatures (as indicated by the peak shifting), the internal stresses induced by the incorporation of the cobalt atoms may

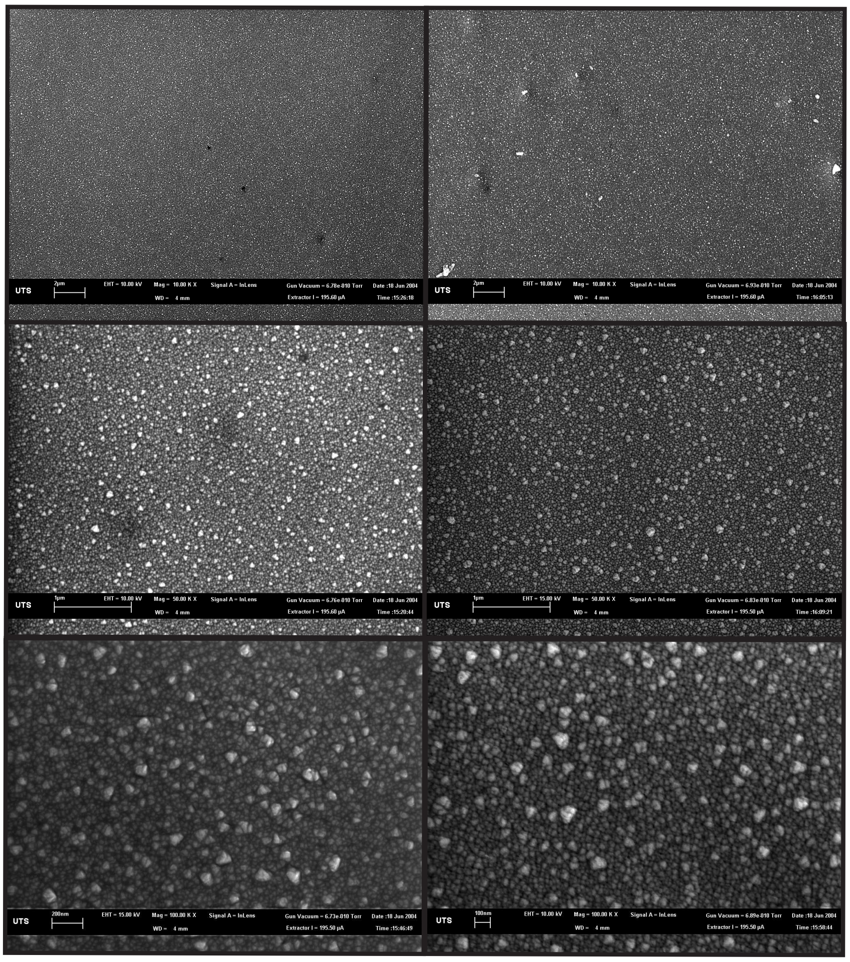

Figure 7.5: SEM image of undoped ZnO films before (first column) and after annealing (second column) at different magnifications. First row: 10000x, second row: 50000x, third row: 100000x.

become higher and contribute to the formation of extensive defects. Similar behavior has also been reported for iron doped ZnO sputtered films [163].

In addition, it has to be reported, that no evidence of cobalt could be found in the XRD spectra. However, this result is consistent for a cobalt concentration of less than 5 at. %, as found in the sputtered ZnO samples, with XRD measurements of Co doped ZnO by Risbud *et. al* [169]. Due to the very high solubility of cobalt of up to 40 at. %, which has been found to be the highest of the 3d transition metals in ZnO [159], phase segregation can only be observed by XRD for high cobalt concentrations. In fact, Risbud *et. al* found a threshold of $x > 0.25$ in bulk polycrystalline $Zn_{1-x}Co_xO$ samples for the appearence of new lines in the XRD spectra associated with a secondary spinel Co_3O_4 phase [169].

In order to investigate the effects of doping and annealing on the surface structure of the specimen, high resolution scanning electron microscopy (chapter 5.9) was

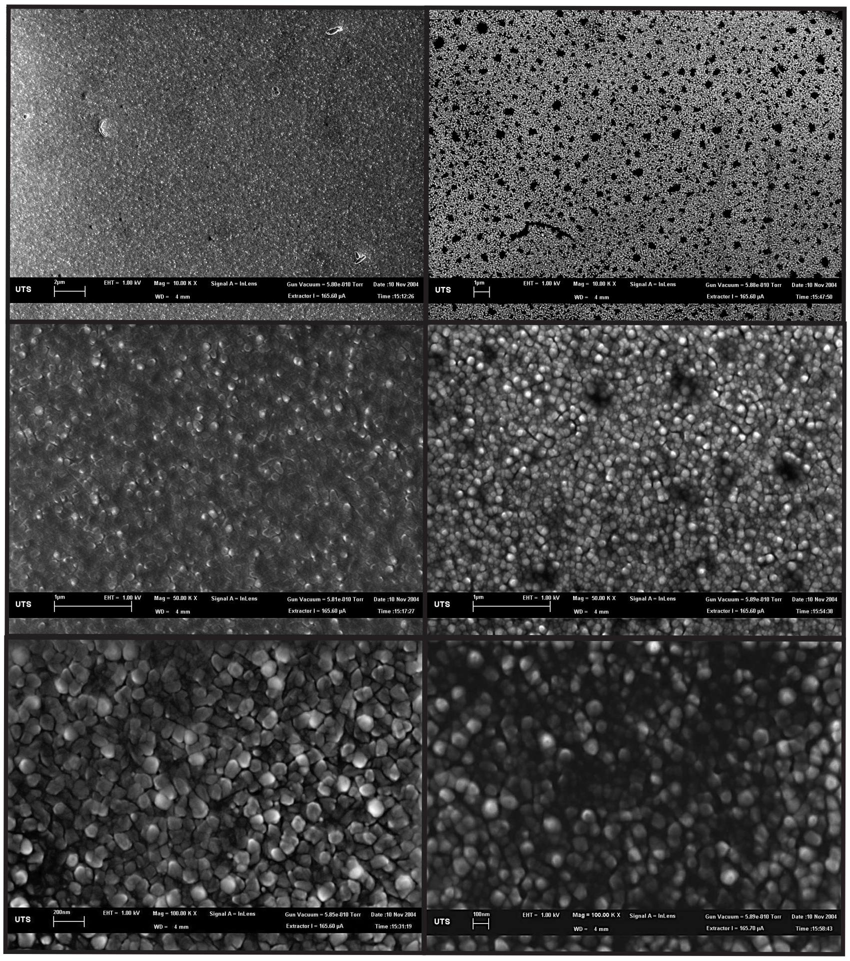

Figure 7.6: SEM image of Co-doped ZnO films before (first column) and after annealing (second column) in nitrogen atmosphere at different magnifications. First row: 10000x, second row: 50000x, third row: 100000x.

performed. Fig. 7.5 displays the SEM images of an undoped ZnO sample before and after annealing for 60 min in a nitrogen atmosphere at 600°C. All images were recorded at display magnifications of 10000x, 50000x and 100000x and are presented in this order from top to bottom with the left side showing the not annealed sample and the right side displaying the SEM images of the annealed one.

The undoped samples clearly show a polycrystalline film with a relatively uniform surface height and structure. The images at 10000x magnification in the first row also indicate the presence of few localized large scale defects with diameters up to 500 nm, that even seem to increase in size after annealing, although it has to be considered that this is not necessarily true, since different sample locations are displayed in the images. At the highest magnification, the grain size can be determined to be

50-100 nm in both, the annealed and not annealed specimen. The larger grains on the surface of the sample are found to be evenly distributed, too. In summary, no large difference between the annealed and not annealed sample undoped ZnO film can be noticed in the SEM images.

On the other hand, the SEM images of the cobalt doped ZnO film with an Co concentration of 4 at. % before and after annealing in Fig. 7.6 exhibit siginicant differences. First of all, the lowest magnification picture of the annealed Co doped ZnO sample shows the massive presence of large scale structural defects with a size of up to 1 μm that are randomely distribute over the surface and not present in the doped sample before annealing. This structural alteration may well be responsible for the increased half-width in the annealed XRD spectra. With larger magnification, it becomes evident, that also for the not annealed Co doped sample, the uniformity in the surface structure and height as seen in the undoped samples is noticeably reduced. Finally, it can be stated, that the observed grain size in the SEM images is, within the precision of measurements, in good agreement with the derived values from the XRD spectra using the Scherrer equation.

7.6 Optical Properties

The optical properties of the undoped as well as cobalt and chromium doped zinc oxide thin films grown by RF magnetron sputtering before and after annealing in different atmospheres are studied by cathodoluminescence and photoluminescence measurements at room temperature, liquid nitrogen temperature and liquid helium temperature. Fig. 7.7 shows the CL spectra of undoped and Co doped ZnO at 80 K. The cobalt concentration in the latter specimen was determine to be five atomic percentage by energy dispersive x-ray analysis (chapter 7.3). After the growth, both samples were annealed for 60 min in nitrogen atmosphere at 600°C.

The typical features of ZnO are clearly present in the CL spectra of the undoped specimen. These are in particular the strong near-bandedge emission resulting from free and bound exciton lines at 3.3 eV in first order and 1.65 eV in second order and the broad defect luminescence between 2 eV and 2.6 eV. In general, the origin of the defect luminescence band is attributed by different theoretical and experimental approaches to intrinsic and / or extrinsic defect complexes. One possible explanation for the emission band in these samples is the green copper luminescence in ZnO (chapter 2.3.6), although an unequivocal assignment would require the observance of the Cu zero phonon line at 2.86 eV.

There are significant differences between the luminescence spectra of the Co-doped and undoped ZnO samples. In particular, the bandedge recombinations seem to be greatly suppressed, resulting in a massive reduction of luminescence inten-

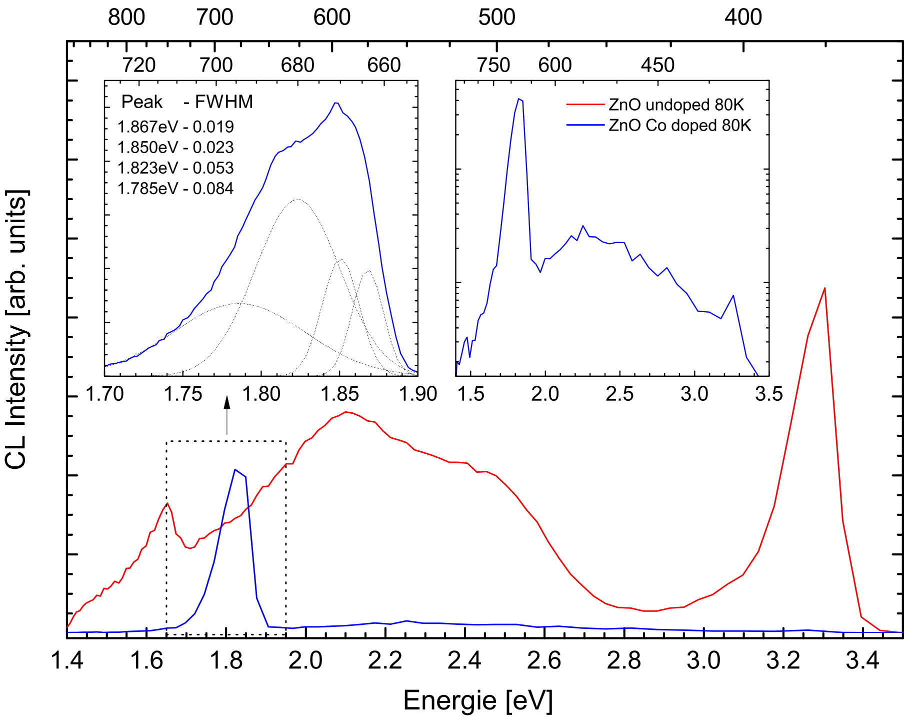

Figure 7.7: Cathodoluminescence of undoped and Co doped ZnO. The upper left graph shows a higher resolution spectra of the red luminescence band in the Co doped samples, while the upper right graph displays the CL spectra with logarithmic scaling, showing a significantly reduced intensity of the near bandgap luminescence compared to the green luminescence an particular to the luminescence centered around 1.8 eV.

sity. A possible explanation is the formation of not only extrinsic defects by the cobalt atoms, but also a large amount of structural defects that effectively introduce carrier traps (chapter 2.3.5), indicating an inferior crystal quality. Electron hole recombinations in the vicinity of these defects are likely to occur non-radiatively, thus leading to a significantly lower CL intensity. The logarithmic scaling in the upper right graph of Fig. 7.7 however shows, that the bandedge and green luminescence, although greatly decreased, are still present in the Co doped sample.

On the other hand, a new luminescence band with strong intensity in the Co-doped specimen centered around 1.8 eV can be observed. The upper left graph in Fig. 7.7 displays a higher resolution CL spectra in the range of 1.7 eV to 1.9 eV. The large emission intensity indicates the formation of highly efficient radiative recombination channels, which might be associated with extrinsic point defects due to the cobalt-doping. Indeed, several other researchers have reported internal cobalt transitions that can be found at similar peak positions [170–172]. The peak shape, supported by Gaussian fitting further suggests that several different radiative transitions contribute and overlap to the observed luminescence.

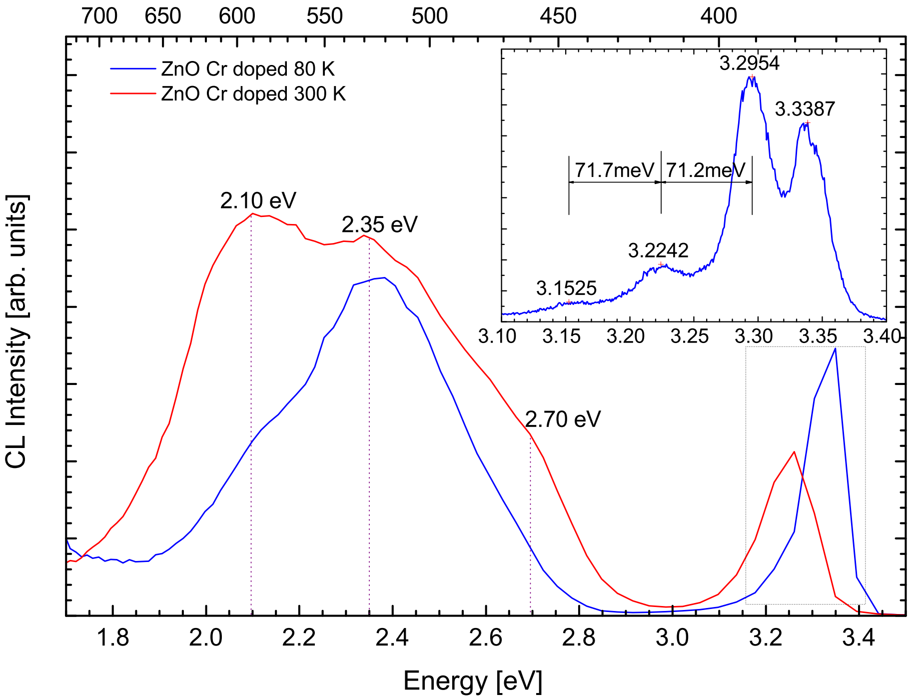

Figure 7.8: Temperature dependent cathodoluminescence of Cr doped ZnO at liquid nitrogen- and room temperatur. The two graphs on the right side show the near bandgap luminescence of a bound exciton complex and three phonon replica of the free exciton zero phonon line (ZPL).

Fig. 7.8 shows cathodoluminescence spectra of heavily chromium doped ZnO at room temperature (300 K) and liquid nitrogen temperature (80 K). The sample was sputtered in a pure argon atmosphere with a chromium diode power of 100 W. Quantitative EDX spectroscopy revealed chromium concentration of 13 at. %. Different from the previously discussed Co-doped sample, the exciton lines and the green luminescence band are strongly present. A more detailed study of the broad luminescence band reveals that it consists at least of two separate overlapping bands. In fact, fitting of the observed luminescence by Gaussian peaks produces a good agreement for three different peaks that are centered at 2.10 eV and 2.35 eV and a smaller side-peak at 2.70 eV. While the peak at 2.35 eV stays almost constant in intensity for the two different spectra at 80 K and 300 K, the peak at 2.10 eV greatly increases in intensity for higher temperatures. Such a behavior could possibly be explained by carriers trapped at deep level defects, which become thermally activated at higher temperatures, leading to new radiative recombination channels and an increase in the peak intensity.

The top right graph of Fig. 7.8 displays the near band gap cathodoluminescence of the chromium doped ZnO specimen at higher resolution. At 80 K, the spectra reveals several well separated peaks at 3.339 eV, 3.295 eV, 3.224 eV and 3.153 eV. The highest energy peak most likely results from a dominant donor bound exciton transition (D^0X), however, the attribution to a specific point defect is not possible. The other three lines appear each at a distance of 71 meV, which corresponds to the energy of the longitudinal optical A_1 mode in ZnO [139–141]. Hence, the lines at 3.224 eV and 3.153 eV can be identified as phonon replica of the higher energy peak.

In order to determine the origin of the most intense peak at 3.295 eV several possibilities need to be discussed. Adding additional 71 meV to the energy of this line leads to a value of 3.366 eV. At this energy, no transition peak can be observed in the luminescence spectra. In addition, the energy of the A free exciton, which could be a possible candidate for a zero phonon line, at a temperature of 80 K under consideration of the Varshni-shift would be 3.3703 eV. This energy deviates by 34 meV from the calculated peak position of a questionable zero phonon line. Hence, it can be concluded, that the peak at 3.295 meV is not a phonon replica itself but rather originates from a different transition.

Possible candidates for this transitions are TES, DAP and free to bound transitions. Two electron satellites may appear at a similar energy (for example the $2p$ TES of the I_{10} at 3.295 eV [24]), but are always accompanied by their significantly more intense parent transition (D^0, X), which is not present in the observed spectra. Therefore, two electron satellites as origin for the 3.295 eV peak can be ruled out. In addition, the common DAP in ZnO are located between 3.10 eV and 3.25 eV for shallow donor and acceptor states, which is at lower energies, than the observed peak. Hence, the emission at 3.295 eV can most likely be attributed to a free to bound transition.

The location of this peak at 135 meV below the bandgap of ZnO (3.43 eV at 80 K) further suggests, that it might result from a (e, A^0) rather than (D^0, h) free to bound transition, since in ZnO the acceptor binding energy E_A is known to be larger than the binding energy of typical dominant donors with $E_D = 35 - 60$ meV. However, the chemical identity of the involved impurity atoms can not be determined at present. Consequently, the lines at 3.224 eV and at 3.153 eV are the first and second phonon replica of this free to bound transition.

In order to investigate and identify the excitonic near-bandgap transitions, low temperature photoluminescence of chromium doped ZnO was recorded. The PL spectra of the previously discussed, heavily doped specimen at a temperature of 2 K

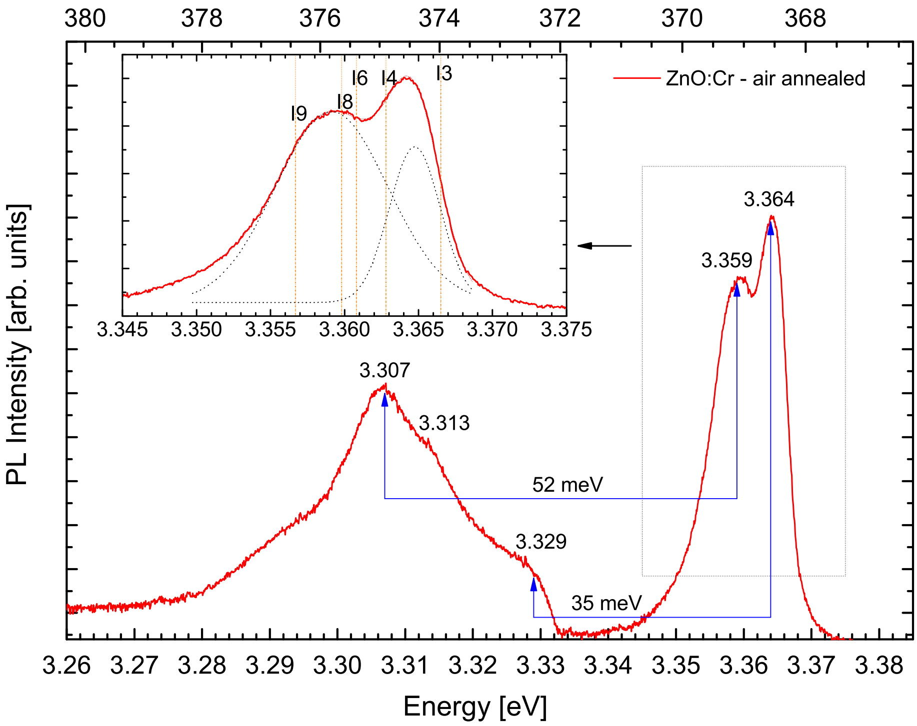

Figure 7.9: High resolution PL spectra of Cr doped ZnO annealed in nitrogen and air atmosphere at 2 Kelvin. The excitonic regime is magnified in the upper left graphs. The positions of bound exciton lines in relaxed bulk ZnO according to the data in table 3.1 are indicated by the vertical drop lines.

in the range of 3.26-3.38 eV is presented in Fig. 7.9. At least two peaks resulting from bound exciton transitions in the chromium doped ZnO sample can be clearly identified. Due to a relatively large halfwidth, resulting in an overlap of the lines, Gaussian fitting reveals slightly different peak positions than those of the local maxima in the spectra. The line energies are therefore determined to be 3.3647 eV and 3.3591 eV. In the upper left graph of the Fig. 7.9, an enlarged view of the bound exciton lines is displayed. The Gaussian fits are represented by the dotted black lines, from which the halfwidth of the peak at 3.3647 eV could be calculated to be 3.4 meV and that of the peak at 3.3591 eV to be 7.6 meV. The vertical orange lines in this window represent the positions of bound excitons in the relevant energy range for a completely relaxed ZnO sample at 2K according to table 3.1.

As discussed in chapter 2.5 the exciton energies can shift under the influence of tensile strain to lower energies and under the presence of compressive strain to higher energies. As all exciton lines shift by the same amount, it is a convenient method to determine the size of the shift for the free exciton in order to specify the influence caused by the internal strain, and then to apply this value to the remaining lines. Unfortunately, the position of the free exciton cannot be ascertained in the acquired spectra, which is probably due to the strong localization of carriers at defects for very low temperatures as discussed in chapter 3.2. Nevertheless, an assignment to bound exciton lines is not impossible without the presence of the free exciton line in the spectra.

Assuming hydrogen is removed from the crystal for an annealing temperature of 700°C [52], the appearance of a strong hydrogen related exciton line can be ruled out. In this case, the two main lines do not need to be considered as possibly shifted against the position of the I_4 exciton line. This would eliminate the possibility of the peak at 3.3591 eV to be associated with an In bound exciton (I_9) shifted under the influence of compressive strain to higher energies. Under the assumption of tensile strain, that is leading to a shift of 1.7 meV to lower energies, the fitted peak positions would match the positions of the I_3 exciton line at 3.3665 eV, which was assigned to an ionized donor [90], and the I_6 exciton line at 3.3608 eV, which is attributed to a neutral aluminum bound exciton [24, 173].

However, this is not the only possible assignment for the bound exciton lines. In order to address this issue, the strong luminescence band between 3.28-3.33 eV in the chromium doped ZnO, which is particularly pronounced for the air annealed specimen, is analyzed. Fitting this region of the spectra by Gaussian peaks reveals the overlapping of at least three separated transition lines, centered at 3.307 eV, 3.313 eV and 3.329 eV, as well as a low energy sideband. All peaks are well within the energy range of typical two-electron-satellites in ZnO and are interpreted as such.

According to chapter 3.5 the energetic position of the TES lines equals those of the associated bound exciton lines from the free exciton, multiplied by a stretching factor s, which was found to be of the size of 2.7 in ZnO [24, 109]. Assuming the lowest energy TES peak at 3.307 eV is correlated with the bound exciton transition at 3.359 eV and the previously reported stretching factor does apply for the investigated samples, a localization energy of 19.2 meV can be derived. This value corresponds exactly to the localization energy of the I_9 bound exciton. Therefore, the peaks at 3.307 and 3.313 could be attributed to the $2p$ and $2s$ TES of the I_9, respectively.

Consequently, the second exciton peak should be assigned to I_4 and is therefore indicating, that hydrogen has not been completely removed from the lattice. According to table 3.1, the localization energy of the I_4 bound exciton complex equals 13.1 meV. Applying the same stretching factor of $s = 2.7$, an associated TES transition for the donor bound exciton peak at 3.3647 eV should be observed at 3.329 eV. This is in excellent agreement with the fitted peak position at the high energy side of the TES luminescence band. However, it should also be noted, that there is an excellent match of the energetic positions, the intensity ratio of the TES line to the associated bound exciton transition peak should be similar for all donor bound exciton complexes within one sample. Hence, the deviant intensities does not allow a doubtless assignment.

Nevertheless, assuming the previous analysis to be correct, the presence of compressive strain, which leads to a blue shift of approximately 2 meV, could be derived from the positions of the bound exciton recombination lines associated with I_4 and I_9. This can be ascribed to the presence of large amounts of chromium atoms, since Cr^{2+} with an ionic radius of 0.73 Å and Cr^{3+} with an ionic radius of 0.615 Å have 22 % and 2.5 % larger ionic radii than Zn^{2+}, which site chromium is expected to occupy in the lattice. Hence, there are strong indicators supporting the later discussed assignment of the bound exciton transitions.

Chapter 8

Conclusion

It was the objective of this thesis to investigate the structural and optical properties of single crystals, high quality MOCVD grown ZnO specimens and thin films grown by RF magnetron sputter deposition by means of various spectroscopic techniques. Of particular interest in this context was the influence of different dopants on the optical properties. Therefore, nitrogen and arsenic as candidates for shallow acceptor states in the MOCVD grown specimens and the transition metals chromium and cobalt for the MSD grown samples were used as dopants.

In order to identify the impurity bound excitons in the MOCVD grown specimens, photoluminescence and transmission spectroscopy in strong external magnetic fields was performed. In particular, detailed studies of the I_8 bound exciton line in nominally undoped ZnO were conducted. From magneto-optical PL measurements, the exciton line was found to split linearly into the two Zeeman components for Faraday and Voigt configuration, thus indicating an exciton complex bound to a neutral impurity. The analysis of the splitting for all possible orientations between the external magnetic field direction and the c-axis of the specimens, including arbitrary angles, allowed the determination of electron and hole effective g-values, which are in good agreement with recently published results [90]. Polarization dependent spectroscopy for $\mathbf{B}\|c$ revealed the high energy Zeeman component to be dominant in σ^+ polarization. Considering the significantly smaller splitting in Faraday than in Voigt configuration and the absence of a crossing of the inner two Zeeman components for arbitrary angles, the bound exciton complex could be identified to involve a hole state having Γ_7 symmetry.

Temperature dependent magneto-optical PL spectroscopy, as well as the thermalization behavior for increasing magnetic fields in photoluminescence, revealed strong indications for the exciton to be bound to an acceptor complex. However, the anomalous behavior for transmission spectroscopy did not allow a conclusive identification.

In the low temperature PL spectra of nitrogen doped ZnO, a strong DAP transition peak with up to six phonon replica, centered at 3.24 eV, could be identified. Since the appearance of a new DAP line after doping with nitrogen is only possible if assuming the introduction of a considerable amount of acceptor states, nitrogen was found to act indeed as an acceptor in the investigated sample. From the energetic position of the DAP and the previously found binding energy of the dominant donor of around 40 meV in ZnO, the acceptor binding energy could be determined to be approximately 165 meV. This is in excellent agreement with the results published in references [68–70]. The large number of phonon replica also shows a significantly stronger phonon coupling of the nitrogen related DAP compared to the less intense residual DAP in nominally undoped ZnO.

At 3.345 eV, an additional new emission peak in the nitrogen doped spectra with excitonic line-shape at low temperatures was identified. The energetic location and the absence of the associated two-electron-satellites supports the attribution to an acceptor bound exciton complex. Temperature dependent PL for nominally undoped and nitrogen doped ZnO showed the thermal activation and quenching behavior from which the thermal activation energy can be determined.

PL spectroscopy of the arsenic doped ZnO specimen revealed, apart from the typical shallow bound exciton spectra of undoped ZnO, three new emission lines at low temperatures. One peak was attributed to a band-acceptor transition involving arsenic as a shallow acceptor state with a binding energy of 128 meV. The other two lines could be identified as deep excitons bound at structural defects. Similar transitions were also observed in nitrogen and sodium doped single crystals. The polarization and angular dependent magnetic field measurements clearly show that the involved hole in the exciton complex originates from a valence band with Γ_7 symmetry. The temperature and magnetic field dependent measurements indicated that these structural defects behave like neutral donor complexes.

Furthermore, an additional emission line could be observed in the PL spectra of the nitrogen doped single crystal, which is shifted by about 4.1 meV to higher energies. The Zeeman splitting of this peak shows a different behavior, which can only be explained by the participation of a hole state from the B valence band with Γ_9 symmetry.

At the University of Technology, Sydney, a large amount of transition metal doped ZnO thin films were grown by RF magnetron sputtering and subsequently annealed in different controlled atmospheres. The properties of these samples were investigated by various experimental techniques, including the study of the optical and structural changes before and after annealing. The successful incorporation of the transition metals was confirmed by EDX and XPS measurements. Using standardless quantization of the EDX data, the transition metal concentration for the previously grown specimens could be determined to be 0-13 at. % and was found to scale linearly with the applied sputter power. Furthermore, the XPS spectra supported the assumption that Co atoms are induced to the ZnO lattice in the isoelectric Co^{2+} charge state on the Zn^{2+} lattice site.

The structural properties of the grown ZnO specimens were investigated by x-ray diffraction (XRD) and scanning electron microscopy (SEM). It was found that the thin films possess a polycrystalline structure with a mean grain size of 70-100 nm. In addition, significant structural variation could be visualized with high resolution SEM pictures before and after annealing.

Finally, it could be shown by cathodoluminescence and photoluminescence spectroscopy that the near bandedge emission of heavily chromium doped ZnO still exhibits the main characteristics of undoped ZnO films. The bound excitons as well as several phonon replica of a free to bound transition could be identified and the appearance of the associated TES lines indicated that the observed exciton lines are bound to donor complexes. The large impact of annealing on the luminescence intensity, which increased up to three orders of magnitude for selected samples compared to the not annealed one, could be noted. On the other hand, Co doped ZnO samples showed a greatly reduced excitonic luminescence and the appearance of a new emission band centered at 1.82 eV, possibly resulting from internal cobalt transitions.

Chapter 9

Zusammenfassung

ZnO basierte Halbleiterbauelemente bieten ein enormes Potenzial für eine Vielzahl von zukünftigen technologischen Anwendungen. Dies betrifft insbesondere die Entwicklung von UV-LEDs und Lasern in der Opto-Elektronik und die Fertigung von Hochtemperatur- und Hochleistungs-Mikroelektronik, wie zum Beispiel transparente Feldeffekt-Transistoren. Auf Grund der starken Widerstandsfähigkeit der strukturellen und optischen Eigenschaften in strahlungsreichen Umgebungen bietet sich ZnO außerdem für die Herstellung elektronischer Bauelemente in Satelliten und Raumsonden an. Darüber hinaus verspricht die Entwicklung von magnetischen Halbleitern (Spintronics) die Möglichkeit, eine völlig neue Klasse der Bauelemente zu erschließen, die von schnellen permanenten Halbleiterspeichern bis zur Fertigung von Quantencomputern reicht.

Allerdings verlangt die Herstellung von qualitativ hochwertigem Zinkoxid für die technologische Anwendung ein grundlegendes Verständnis der intrinsischen und extrinsischen Störstellen und Defekte. Eines der Hauptprobleme der Kommerzialisierung von ZnO-basierten Bauelementen ist dabei die bisher unzureichende p-Leitfähigkeit. Daher ist insbesondere eine umfassende Einsicht in die Bildung flacher Akzeptor-Zustände und der einhergehenden Kompensationsmechanismen erforderlich.

In der vorliegenden Arbeit wurden die strukturellen und optischen Eigenschaften von Einkristallen sowie MOCVD und MSD gewachsenen ZnO-Proben unter Anwendung verschiedener spektroskopischer Methoden untersucht. Zur Identifikation der störstellengebundenen Exzitonen wurden Photoluminesenz- und Absorptionsmessungen in starken externen Magnetfeldern durchgeführt. Insbesondere wurde die gebundene Exziton-Rekombinationslinie I_8 in undotierten MOCVD-Proben bezüglich ihrer Thermalisierung untersucht. Die PL-Spektren der Zeeman-gespaltenen Emissionslinie zeigen sowohl mit steigender Magnetfeldstärke als auch mit wachsender Temperatur eine deutliche Thermalisierung, die im Rahmen der verwendeten theoretischen Modelle einen Akzeptor gebundenen Exziton-Komplex nahe legt. Anhand der Aufspaltung der einzelnen Komponenten im Magnetfeld konnte ferner gezeigt werden, dass es sich um ein Exziton, gebunden an einer neutralen Störstelle, handelt. Polarisations- und winkelabhängige Magnetfeldmessungen erlaubten die Bestimmung der effektiven Elektronen- und Löcher Landé-Faktoren. Außerdem konnte die Symmetrie der involvierten Loch-Zustände als Γ_7 identifiziert werden.

Die Photoluminesenz-Spektren von Stickstoff dotiertem ZnO zeigen das Auftreten eines dominanten DAP-Überganges, der von bis zu sechs Phonon Replica begleitet wird. Anhand der Position des DAPs und der bekannten Bindungsenergie des in ZnO dominanten Donators von ungefähr 40 meV konnte die Bindungsenergie des zugehörigen Akzeptors auf ca. 165 meV bestimmt werden. Die Position einer weiteren neuen Exziton-Linie bei 3.345 eV und das Fehlen der assoziierten TES-Emission deuten ebenfalls auf einen Akzeptor gebundenen Exziton-Komplex in den Stickstoff dotierten Proben hin. Temperaturabhängige Messungen erlauben die Untersuchung der thermischen Aktivierung von Störstellen, von denen die jeweiligen Aktivierungsenergien bestimmt werden konnten.

In der Arsen dotieren MOCVD-Probe konnte eine Luminesenz beobachtet werden, die einem Band-Akzeptor-Übergang zugeschrieben wird. Eine Bindungsenergie von 128 meV für den involvierten Akzeptor-Komplex, dessen chemische Identität naheliegender Weise als Arsen angenommen wird, wurde ermittelt. Darüber hinaus wurden in dieser Probe sowie in zwei mit Stickstoff und Natrium dotierten ZnO-Einkristallen tief gebundene Exziton-Linien an strukturellen Defekten beobachtet. Anhand von polarisations- und winkelabhängigen Magnetfeldmessungen wurde eine Γ_7-Symmetrie des beteiligten Loch-Zustandes für die exzitonischen Linien in der Arsen dotierten Probe bestimmt. Das Thermalisierungsverhalten zeigte außerdem, dass sich die untersuchten Komplexe an strukturellen Defekten wie neutrale Donatoren verhalten. In dem Stickstoff implantierten Einkristall wird ferner eine weitere um 4.1 meV zu höheren Energien verschobene Emissionslinie beobachtet. Die Zeeman-Aufspaltung dieser Linie impliziert die Beteiligung eines Loches aus dem B-Valenzband mit Γ_9-Symmetrie.

Eine große Anzahl undotierter und Übergangsmetall-dotierter dünner ZnO-Filme auf Silizium-Substrat wurde mittels Sputter Deposition hergestellt. Die Eigenschaften dieser Proben wurden in Abhängigkeit von den Herstellungsparametern mit einer Vielzahl unterschiedlicher experimenteller Methoden untersucht. Dabei wurden ebenfalls die strukturellen und optischen Veränderungen vor und nach dem Tempern in verschiedenen Atmosphären analysiert. Der erfolgreiche Einbau der Übergangsmetalle wurde mittels EDX and XPS nachgewiesen. Durch die quantitative Auswertung der EDX-Daten konnte eine Konzentration der 3d Metalle von 0 bis 13 at. % nachgewiesen werden, die linear mit der Sputter Leistung skaliert. Außerdem wurden Hinweise in den XPS-Spektren gefunden, die auf einen Gittereinbau der Kobalt-Atome im Co^{2+} Ladungszustand hindeuten könnten.

Die strukturellen Eigenschaften der hergestellten dünnen ZnO Schichten wurden mittels Röntgendiffraktometrie (XRD) und Rasterelektronenmikroskopie (SEM) untersucht. Die Ergebnisse dieser Messungen zeigen, dass die ZnO-Schichten eine polykristalline Struktur mit durchschnittlichen Cluster-Größen von 70-100 nm besitzen. Außerdem konnten deutliche strukturelle Veränderungen der dotierten Filme nach dem Tempern visualisiert werden.

Durch Kathodenluminesenz und Photoluminesenz Spektroskopie wurde gezeigt, dass die Bandkantenemission von Chrom dotiertem ZnO die typischen Charakteristika von ZnO aufzeigt. Mit Hilfe der Spektren bei tiefen Temperaturen konnten gebundene Exzitonen und mehrere Phonon Replica eines Band-Akzeptor-Übergangs identifiziert werden. Außerdem deutet die Präsenz der zugehörigen TESs auf Donator gebundene Exziton-Komplexe hin. Die große Bedeutung des Temper-Prozesses nach dem Wachstum konnte durch eine teilweise um drei Größenordnungen höhere Bandkantenemission verdeutlicht werden. Co dotiertes ZnO zeigte andererseits eine starke Reduzierung der exzitonischen Luminesenz und das Auftreten eines neuen Emissionsbandes um 1.82 eV, das möglicherweise internen Co-Übergängen zugeschrieben werden kann.

Chapter 10

Publications

Parts of this work have already been presented at international conferences:

- E-MRS Spring Meeting, Strasbourg, France, May 31 - June 03, 2005
  European Materials Research Society
  - **CL Studies of transition metal doped ZnO produced by RF magnetron sputtering** (oral)
    M. R. Phillips[1], M. R. Wagner[2], E. Malguth[2], A. Hoffmann[2]
    [1] Microstructural Analysing Unit, University of Technology Sydney
    [2] Institute of Solid State Physics, Technical University Berlin
  - **Acceptor Related Luminescence in ZnO** (poster)
    A. Hoffmann[1], M. R. Wagner[1], J. Christen[2], F. Bertram[2], Th. Hempel[2], S. Petzold[2], A. Dadgar[2], N. Oleynik[2], A. Krost[2]
    [1] Institute of Solid State Physics, Technical University Berlin
    [2] Institute of Experimental Physics, Otto-von-Guericke-University Magdeburg

- II-VI 2005, Warsaw, Poland, September 12 - 16, 2005
  12th International Conference on II-VI Compounds
  - **Direct Observation of As-related (e,A)-emission in ZnO** (oral)
    F. Bertram[1], S. Giemsch[1], J. Christen[1], A. Dadgar[1], A. Krost[1],
    M. R. Wagner[2], A. Hoffmann[2]
    [1] Institute of Experimental Physics, Otto-von-Guericke-University Magdeburg
    [2] Institute of Solid State Physics, Technical University Berlin
  - **Direct Evidence of Impurity Related Free-to-Bound Transition in ZnO** (poster)
    J. Christen[1], F. Bertram[1], S. Giemsch[1], Th. Hempel[1], S. Petzold[1], A. Dadgar[1], N. Oleynik[1], A. Krost[1], M. Wagner[2], A. Hoffmann[2]
    [1] Institute of Experimental Physics, Otto-von-Guericke-University Magdeburg
    [2] Institute of Solid State Physics, Technical University Berlin

- 2005 MRS Fall Meeting, Boston, USA, November 28 - December 01, 2005
  Fall Meeting of the Materials Research Society
  - **Acceptor related Luminescence in ZnO** (oral)
    F. Bertram[1], J. Christen[1], S. Giemsch[1], T. Hempel[1], S. Petzold[1], A. Dadgar[1], A. Krost[1], A. Hoffmann[2], M. R. Wagner[2]
    [1] Institute of Experimental Physics, Otto-von-Guericke-University Magdeburg
    [2] Institute of Solid State Physics, Technical University Berlin
  - **On the role of group I elements in ZnO** (oral)
    B. Meyer[1], J. Sann[1], N. Volbers[1], A. Zeuner[1], A. Hoffmann[2], U. Haboeck[2], M. R. Wagner[2]
    [1] Physikalisches Institut, Justus-Liebig-Universität Gießen
    [2] Institute of Solid State Physics, Technical University Berlin

Chapter 11

Acknowledgement

The research and outcome presented within this thesis are the results of the work, both in the Institute of Solid State Physics at the Technical University, Berlin (TUB) and in the Microstructural Analysis Unit at the University of Technology, Sydney (UTS). I would like to use the opportunity to thank all persons, who supported me during the entire process of this thesis and contributed to the accomplishment of this work.

From the Technical University, Berlin:

- Priv. Doz. Dr. Axel Hoffmann for the opportunity to work in an interesting and dynamic evolving field of research, where I could greatly benefit from his knowledge and comprehension. I am also very thankful for his support in all matters of organization, enabling me to spend two semesters at the UTS in the group of Prof. Matthew Phillips, which I greatly enjoyed and acknowledge as beneficial. In addition, I would like to express my gratitude for his dedication and enthusiasm towards the realization of future projects.

- Prof. I. Broser for being co-supervisor and his manifold comments and suggestions to improve this thesis.

- Heiner Perls and Bernd Schöler, who always found time and helpful solutions for any kind of practical problems in the everyday lab-work and therefore greatly contributed to the efficient progress of the projects.

- Robert McKenna, Jhonny Vielses, and Suresh Gondi for their assistance with the magneto-optical measurements

- Hagen Telg for his tips and tricks concerning LaTeX

- Matthias Dworzak for his introduction and advice

- all members of the work group Thomsen/Hoffmann for contributing to the great atmosphere within this group through lots of fun and fruitful discussions.

From the University of Technology, Sydney:

- Prof. Matthew Phillips for introducing me to the concepts of scientific research and his support in all question of physics and beyond. I gratefully thank him for many physical insights he revealed to me, as well as his joyful manner of dealing with his students and colleagues, making my time at the UTS not only an enlightening and informative, but also very pleasant time.
- Katie McBean, Richard Wuhrer and Mark Berkahn for their assistance with various aspects of the SEM and XRD measurements, as well as their time and help solving many small problems.
- The whole staff of the MAU for their support and humorous way of life that makes everything look easy and contributed to me having a great time in Sydney.
- Geoff McCredie for his assistance with the RF sputter deposition process and the XPS measurements.

From the Otto-von-Guericke-University, Magdeburg:

- The group of Prof. J. Christen, who provided the MOCVD grown samples and the temperature dependent PL spectra of the nominally undoped and nitrogen doped ZnO specimens.

Diane, my brother and my parents.

Bibliography

[1] D. C. Reynolds, D. C. Look, and B. Jogai, “Optically pumped ultraviolet lasing from ZnO”, Solid State Commun. **99**, 873 (1996).

[2] D. M. Bagnall, Y. F. Chen, Z. Zhu, T. Yao, S. Koyama, M. Y. Shen, and T. Goto, “Optically pumped lasing of ZnO at room temperature”, Appl. Phys. Lett. **70**, 2230 (1997).

[3] Z. K. Tang, G. K. L. Wong, P. Yu, M. Kawasaki, A. Ohtomo, H. Koinuma, and Y. Segawa, “Room-temperature ultraviolet laser emission from self-assembled ZnO microcrystallite thin films”, Appl. Phys. Lett. **72**, 3270 (1998).

[4] M. Wraback, H. Shen, S. Liang, C. R. Gorla, and Y. Lu, “High contrast, ultrafast optically addressed ultraviolet light modulator based upon optical anisotropy in ZnO films grown on R-plane sapphire”, Appl. Phys. Lett. **74**, 507 (1999).

[5] Y. Li, G. S. Tompa, S. Liang, C. Gorla, Y. Lu, and J. Doyle, “Transparent and conductive Ga-doped ZnO films grown by low pressure metal organic chemical vapor deposition”, J. Vac. Sci. Technol. A **15**, 1063 (1997).

[6] T. Makino, Y. Segawa, M. Kawasaki, A. Ohtomo, R. Shiroki, *et al.*, “Band gap engineering based on $\mathrm{Mg_xZn_{1-x}O}$ and $\mathrm{Cd_yZn_{1-y}O}$ ternary alloy films”, Appl. Phys. Lett. **78**, 1237 (2001).

[7] K. Nomura, H. Ohta, K. Ueda, T. Kamiya, M. Hirano, and H. Hosono, “Thin-film transistor fabricated in single-crystalline transparent oxide semiconductor”, Science **300**, 1269 (2003).

[8] P. F. Carcia, R. S. McLean, M. H. Reilly, and J. G. Nunes, “Transparent ZnO thin-film transistor fabricated by rf magnetron sputtering”, Appl. Phys. Lett. **82**, 1117 (2003).

[9] D. C. Look, D. C. Reynolds, J. W. Hemsky, R. L. Jones, and J. R. Sizelove, “Production and annealing of electron irradiation damage in ZnO”, Appl. Phys. Lett. **75**, 811 (1999).

[10] D. C. Look, J. W. Hemsky, and J. R. Sizelove, “Residual native shallow donor in ZnO”, Phys. Rev. Lett. **82**, 2552 (1999).

[11] F. D. Auret, S. A. Goodman, M. Hayes, M. J. Legodi, H. A. van Laarhoven, and D. C. Look, “Electrical characterization of 1.8 MeV proton-bombarded ZnO”, Appl. Phys. Lett. **79**, 3074 (2001).

[12] D. G. Thomas, “The exciton spectrum of zinc oxide”, J. Phys. Chem. Solids **15**, 86 (1960).

[13] S. C. Jain, M. Willander, J. Narayan, and R. van Overstraeten, “III-nitrides: Growth, characterization, and properties”, J. Appl. Phys. **87**, 965 (1999).

[14] T. Dietl, H. Ohno, F. Matsukura, J. Cibert, and D. Ferrand, “Zener model description of ferromagnetism in zinc-blende magnetic semiconductors”, Science **287**, 1019 (2000).

[15] K. Sato and H. Katayama-Yoshida, “Material design for transparent ferromagnets with ZnO-based magnetic semiconductors”, Jpn. J. Appl. Phys. **39**, 555 (2000).

[16] T. Wakano, N. Fujimura, Y. Morinaga, N. Abe, A. Ashida, and T. Ito, “Magnetic and magneto-transport properties of ZnO:Ni films”, Physica E **10**, 260 (2001).

[17] S. W. Jung, S.-J. An, G.-C. Yi, C. U. Jung, S.-I. Lee, and S. Cho, “Ferromagnetic properties of $\mathrm{Zn_{1-x}Mn_xO}$ epitaxial thin films”, Appl. Phys. Lett. **80**, 4561 (2002).

[18] K. R. Kittilstved, N. S. Norberg, and D. R. Gamelin, “Chemical manipulation of high-T_c ferromagnetism in ZnO diluted magnetic semiconductors”, Phys. Rev. Lett. **94**, 147 209 (2005).

[19] T. Minami, H. Sato, H. Nanto, and S. Takata, “Group III impurity doped zinc oxide thin films prepared by RF magnetron sputtering”, Jpn. J. Appl. Phys. **24**, 781 (1985).

[20] G. F. Neumark, “Achievement of well conducting wide-band-gap semiconductors: Role of solubility and nonequilibrium impurity incorporation”, Phys. Rev. Lett. **62**, 1800 (1989).

[21] D. J. Chadi, “Doping in ZnSe, ZnTe, MgSe and MgTe wide-band-gap semiconductors”, Phys. Rev. Lett. **72**, 534 (1993).

[22] S. B. Zhang, S. H. Wei, and A. Zunger, “Microscopic origin of the phenomenological equilibrium doping limit rule in n-type III-V semiconductors”, Phys. Rev. Lett. **84**, 1232 (1999).

[23] T. Dietl, A. Haury, and Y. M. d’Aubigne, “Free carrier-induced ferromagnetism in structures of diluted magnetic semiconductors”, Phys. Rev. B **55**, 3347 (1997).

[24] B. K. Meyer, H. Alves, D. M. Hofmann, W. Kriegseis, D. Forster, *et al.*, “Bound exciton and donor-acceptor pair recombinations in ZnO”, Phys. Stat. Sol. (b) **241**, 231 (2004).

[25] S. J. Pearton, D. P. Norton, K. Ip, Y. W. Heo, and T. Steiner, “Recent progress in processing and properties of ZnO”, Progress Mat. Sci. **50**, 293 (2005).

[26] Y. Chen, D. M. Bagnall, H.-J. Koh, K.-T. Park, K. Hiraga, Z. Zu, and T. Yao, “Plasma assisted molecular beam epitaxy of ZnO on c-plane sapphire: Growth and characterization”, J. Appl. Phys. **84**, 3912 (1998).

[27] W. Y. Liang and A. D. Yoffe, “Transmission spectra of ZnO single crystals”, Phys. Rev. Lett. **20**, 59 (1968).

[28] D. C. Reynolds, D. C. Look, B. Jogai, C. W. Litton, G. Cantwell, and W. C. Harsch, “Valence-band ordering in ZnO”, Phys. Rev. B **60**, 2340 (1999).

[29] R. Dingle, “Luminescent transitions associated with divalent copper impurities and the green emission from semiconducting zinc oxide”, Phys. Rev. Lett. **23**, 579 (1969).

[30] E. G. Bylander, “Surface effects on the low-energy cathodoluminescence of zinc oxide”, J. Appl. Phys. **49**, 1188 (1978).

[31] K. Vanheusden, C. H. Seager, W. L. Warren, D. R. Tallant, and J. A. Voigt, “Correlation between photoluminescence and oxygen vacancies in ZnO phosphors”, Appl. Phys. Lett. **68**, 403 (1996).

[32] M. Liu, A. H. Kitai, and P. Mascher, “Point defects and luminescence centers in zinc oxide and zinc oxide doped with manganese”, J. Luminescence **54**, 35 (1992).

[33] B. Lin, Z. Fu, and Y. Jia, “Green luminescent center in undoped zinc oxide films deposited on silicon substrates”, Appl. Phys. Lett. **79**, 943 (2001).

[34] D. B. Laks, C. G. van de Walle, G. F. Neumark, and S. T. Pantelides, “Role of native defects in wide-band-gap semiconductors”, Phys. Rev. Lett. **66**, 648 (1991).

[35] E. C. Lee, Y. S. Kim, Y. G. Jin, and K. J. Chang, “Compensation mechanism for N acceptors in ZnO”, Phys. Rev. B **64**, 085 120 (2001).

[36] C. H. Park, S. B. Zhang, and S. H. Wei, “Origin of p-type doping difficulty in ZnO: The impurity perspective”, Phys. Rev. B **66**, 073 202 (2002).

[37] K.-H. Bang, D.-K. Hwang, M.-C. Park, Y.-D. Ko, I. Yun, and J.-M. Myoung, “Formation of p-type ZnO film on InP substrate by phosphor doping”, Appl. Surf. Sci. **210**, 177 (2003).

[38] K.-K. Kim, H.-S. Kim, D.-K. Hwang, J.-H. Lim, and S.-J. Park, “Realization of p-type ZnO thin films via phosphorus doping and thermal activation of the dopant”, Appl. Phys. Lett. **83**, 63 (2003).

[39] Y. R. Ryu, S. Zhu, D. C. Look, J. M. Wrobel, H. M. Jeong, and H. W. White, “Synthesis of p-type ZnO films”, J. Cryst. Growth **216**, 330 (2000).

[40] Y. R. Ryu, T. S. Lee, and H. W. White, “Properties of arsenic-doped p-type ZnO grown by hybrid beam deposition”, Appl. Phys. Lett. **83**, 87 (2003).

[41] C. Morhain, M. Teisseire, S. Vezian, F. Vigue, F. Raymond, *et al.*, “Spectroscopy of excitons, bound excitons and impurities in h-ZnO epilayers”, Phys. Stat. Sol. (b) **229**, 881 (2002).

[42] V. Vaithianathan, B. T. Lee, and S. S. Kim, “Preparation of As-doped p-type ZnO films using Zn_3As_2/ZnO target with pulsed laser deposition”, Appl. Phys. Lett. **86**, 062 101 (2005).

[43] R. D. Shannon, “Revised effective ionic radii and systematic studies of interatomic distances in halides and chalcogenides”, Acta Crystallographica **A32**, 751 (1976).

[44] C. G. van de Walle and J. Neugebauer, “Universal alignment of hydrogen levels in semiconductors, insulators and solutions”, Nature **423**, 626 (2003).

[45] C. G. van de Walle, “Hydrogen as a cause of doping in zinc oxide”, Phys. Rev. Lett. **85**, 1012 (2000).

[46] S. F. J. Cox, E. A. Davis, S. P. Cottrell, P. J. C. King, J. S. Lord, *et al.*, “Experimental confirmation of the predicted shallow donor hydrogen state in zinc oxide”, Phys. Rev. Lett. **86**, 2601 (2001).

[47] D. M. Hofmann, A. Hofstaetter, F. Leiter, H. Zhou, F. Henecker, *et al.*, “Hydrogen: A relevant shallow donor in zinc oxide”, Phys. Rev. Lett. **88**, 045 504 (2002).

[48] E. V. Lavrov, J. Weber, F. Börrnert, C. G. van de Walle, and R. Helbig, “Hydrogen-related defects in ZnO studied by infrared absorption spectroscopy”, Phys. Rev. B **66**, 165 205 (2002).

[49] D. C. Look, C. Coskun, B. Claflin, and G. C. Farlow, “Electrical and optical properties of defects and impurities in ZnO”, Physica B **340**, 32 (2003).

[50] J. I. Pankove, “Hydrogen in semiconductors”, Academic Press, Boston (1991).

[51] K. Minegishi, Y. Koiwai, Y. Kikuchi, K. Yano, M. Kasuga, and A. Shimizu, “Growth of p-type zinc oxide films by chemical vapor deposition”, Jpn. J. Appl. Phys. **36**, 1453 (1997).

[52] K. Ip, M. E. Overberg, Y. W. Heo, D. P. Norton, S. J. Pearton, *et al.*, “Nitrogen incorporation and diffusivity in plasma-exposed bulk ZnO”, Appl. Phys. Lett. **82**, 385 (2003).

[53] P. H. Kasai, “Electron spin resonance studies of donors and acceptors in ZnO”, Physical Review **130**, 989 (1963).

[54] E. Tomzig and R. Helbig, “Band-edge emission in ZnO”, J. Luminescence **14**, 403 (1976).

[55] M. G. Wardle, J. P. Goss, and P. R. Briddon, “Theory of Li in ZnO: A limitation for Li-based p-type doping”, Phys. Rev. B **71**, 155 205 (2005).

[56] M. Joseph, H. Tabata, and T. Kawai, “p-type electrical conduction in ZnO thin films by Ga and N codoping”, Jpn. J. Appl. Phys. **38**, 1205 (1999).

[57] T. Yamamoto and H. Katayama-Yoshida, “Solution using a codoping method to unipolarity for the fabrication of p-type ZnO”, Jpn. J. Appl. Phys. **38**, 166 (1999).

[58] M. Joseph, H. Tabata, H. Saeki, K. Ueda, and T. Kawai, “Fabrication of low-resistive p-type ZnO by codoping method”, Physica B **302**, 140 (2001).

[59] A. B. M. A. Ashrafi, I. Suemune, H. Kumano, and S. Tanaka, “Nitrogen-doped p-type ZnO layers prepared with H_2O vapor-assisted metalorganic molecular-beam epitaxy”, Jpn. J. Appl. Phys. **41**, 1281 (2002).

[60] D. C. Look, D. C. Reynolds, C. W. Litton, R. L. Jones, D. B. Eason, and G. Cantwell, “Characterization of homoepitaxial p-type ZnO grown by molecular beam epitaxy”, Appl. Phys. Lett. **81**, 1830 (2002).

[61] T. Aoki, Y. Shimizu, A. Miyake, A. Nakamura, Y. Nakanishi, and Y. Hatanaka, “p-type ZnO layer formation by excimer laser doping”, Phys. Stat. Sol. (b) **229**, 911 (2002).

[62] A. V. Singh, R. M. Mehra, A. Wakahara, and A. Yoshida, “p-type conduction in codoped ZnO thin films”, J. Appl. Phys. **93**, 396 (2003).

[63] J. Wang, G. Du, B. Zhao, X. Yang, Y. Zhang, *et al.*, “Epitaxial growth of NH_3-doped ZnO thin films on sapphire substrates”, J. Cryst. Growth **255**, 293 (2003).

[64] A. Kobayashi, O. F. Sankey, and J. D. Dow, “Deep energy levels of defects in the wurtzite semiconductors AlN, CdS, CdSe, ZnS, and ZnO”, Phys. Rev. B **28**, 946 (1983).

[65] W. E. Carlos, E. R. Glaser, and D. C. Look, “Magnetic resonance studies of ZnO”, Physica B **308**, 976 (2001).

[66] N. Y. Garces, N. C. Giles, L. E. Halliburton, G. Cantwell, D. B. Eason, D. C. Reynolds, and D. C. Look, “Production of nitrogen acceptors in ZnO by thermal annealing”, Appl. Phys. Lett. **80**, 1334 (2002).

[67] Y. Yan and S. B. Zhang, “Control of doping by impurity chemical potentials: Predictions for p-type ZnO”, Phys. Rev. Lett. **86**, 5723 (2001).

[68] A. Zeuner, H. Alves, D. M. Hofmann, B. K. Meyer, A. Hoffmann, *et al.*, “Optical properties of the nitrogen acceptor in epitaxial ZnO”, Phys. Stat. Sol. (b) **234**, R7 (2002).

[69] M. Strassburg, U. Haboeck, A. Kaschner, M. Strassburg, A. V. Rodina, *et al.*, Proceedings of the 26th international conference on the physics of semiconductors **171**, 45 (2003).

[70] G. Xiong, K. B. Ucer, R. T. Williams, J. Lee, D. Bhattacharyya, J. Metson, and P. Evans, “Donor-acceptor pair luminescence of nitrogen-implanted ZnO single crystal”, J. Appl. Phys. **97**, 043 528 (2005).

[71] K. Thonke, T. Gruber, N. Teofilov, R. Schönfelder, A. Waag, and R. Sauer, “Donor-acceptor pair transitions in ZnO substrate material”, Physica B **308**, 945 (2001).

[72] S. Limpijumnong, S. B. Zhang, S.-H. Wei, and C. H. Park, “Doping by large-size-mismatched impurities: The microscopic origin of arsenic- or antimony-doped p-type zinc oxide”, Phys. Rev. Lett. **92**, 155 504 (2004).

[73] J. Ewles, "Luminescent spectra of some solids at low temperatures", Proc. Roy. Soc. (London) **A167**, 34 (1938).

[74] C. Solbrig, "Zinkoxydkristalle in Abhängigkeit von Temperatur und uniaxialer Verspannung", Z. Physik **211**, 429 (1968).

[75] I. J. Broser, R. K. F. Germer, H.-J. E. Schulz, and K. P. Wisznewski, "Fine structure and Zeemann effect of the excited state of the green emitting copper centre in zinc oxide", Solid State Electronics **21**, 1597 (1978).

[76] P. J. Dean, D. J. Robbins, S. G. Bishop, J. A. Savage, and P. Porteous, "The optical properties of copper in zinc oxide", J. Phys. C **14**, 2847 (1981).

[77] D. J. Robbins, D. C. Herbert, and P. J. Dean, "The origin of the α, β, γ blue no-phonon transitions in ZnO:Cu-A deep-level problem", J. Phys. C **14**, 2859 (1981).

[78] R. Pappalardo and R. E. Dietz, "Absorption spectra of transition ions in CdS crystals", Physical Review **123**, 1188 (1961).

[79] H. A. Weakliem, "Optical spectra of Ni^{2+}, Co^{2+}, and Cu^{2+} in tetrahedral sites in crystals", J. Chem. Phys. **36**, 2117 (1962).

[80] R. E. Dietz, H. Kamimura, M. D. Sturge, and A. Yariv, "Electronic structure of copper impurities in ZnO", Physical Review **132**, 1559 (1963).

[81] W. R. L. Lambrecht, A. V. Rodina, S. Limpijumnong, B. Segall, and B. K. Meyer, "Valence-band ordering and magneto-optic exciton fine structure in ZnO", Phys. Rev. B **65**, 075 207 (2002).

[82] M. Cardona, "Optical properties of the silver and cuprous halides", Physical Review **129**, 69 (1963).

[83] K. Shindo, A. Morita, and H. Kamimura, "Spin-orbit coupling in ionic crystals with zincblende and wurtzite structures", J. Phys. Soc. Jpn. **20**, 2054 (1965).

[84] J. L. Birman, "Polarization of fluorescence in CdS and ZnS single crystals", Phys. Rev. Lett. **2**, 157 (1959).

[85] J. L. Birman, "Some selection rules for band-band transitions in wurtzite structure", Physical Review **114**, 1490 (1959).

[86] D. C. Reynolds, C. W. Litton, and T. C. Collins, "Zeeman effects in the edge emission and absorption of ZnO", Physical Review **140**, 1726 (1965).

[87] Y. S. Park, C. W. Litton, T. C. Collins, and D. C. Reynolds, “Exciton spectrum of ZnO”, Physical Review **143**, 512 (1966).

[88] P. Hohenberg and W. Kohn, “Inhomogeneous electron gas”, Physical Review **136**, B864 (1964).

[89] R. T. Girard, O. Tjernberg, G. Chiaia, S. Sönderholm, U. O. Karsson, *et al.*, “Electronic structure of ZnO(0001) studied by angle-resolved photoelectron spectroscopy”, Surf. Sci. **373**, 409 (1997).

[90] A. V. Rodina, M. Strassburg, M. Dworzak, U. Haboeck, A. Hoffmann, *et al.*, “Magneto-optical properties of bound excitons in ZnO”, Phys. Rev. B **69**, 125 206 (2004).

[91] D. C. Reynolds, D. C. Look, B. Jogai, R. L. Jones, C. W. Litton, W. Harsch, and G. Cantwell, “Optical properties of ZnO crystals containing internal strains”, J. Luminescence **82**, 173 (1999).

[92] T. Koda and D. W. Langer, “Splitting of exciton lines in wurtzite-type II-VI crystals by uniaxial stress”, Phys. Rev. Lett. **20**, 50 (1968).

[93] O. Akimoto and H. Hasegawa, “Strain-induced splitting and polarization of excitons due to exchange interaction”, Phys. Rev. Lett. **20**, 916 (1968).

[94] B. Gil, A. Lusson, V. Sallet, S.-A. Said-Hassani, R. Triboulet, and P. Bigenwald, “Strain-fields effects and reversal of the nature of the fundamental valence band of ZnO epilayers”, Jpn. J. Appl. Phys. **40**, 1089 (2001).

[95] M. A. Lampert, “Mobile and immobile effective-mass-particle complexes in nonmetallic solids”, Phys. Rev. Lett. **1**, 450 (1958).

[96] J. R. Haynes, “Experimental proof of the existance of a new electronic complex in silicon”, Phys. Rev. Lett. **4**, 361 (1960).

[97] J. J. Hopfield and D. G. Thomas, “On some observable properties of longitudinal excitons”, J. Phys. Chem. Solids **12**, 276 (1960).

[98] J. J. Hopfield, “Fine structure in the optical absorption edge of anisotropic crystals”, J. Phys. Chem. Solids **15**, 97 (1960).

[99] J. S. Prener and F. E. Williams, “Associated donor-acceptor luminescent centers”, Physical Review **101**, 1427 (1956).

[100] F. Williams, “Donor-Acceptor Pairs in Semiconductors”, Phys. Stat. Sol. **25**, 493 (1968).

[101] L. Hedin and B. I. Lundqvist, “Explicit local exchange-correlation potentials”, J. Phys. C **4**, 2064 (1971).

[102] O. Gunnarsson and B. I. Lundqvist, “Exchange and correlation in atoms, molecules and solids by the spin-density-functional formalism”, Phys. Rev. B **13**, 4274 (1976).

[103] P. J. Dean, J. D. Cuthbert, D. G. Thomas, and R. T. Lynch, “Two-electron transitions in the luminescence of excitons bound to neutral donors in gallium phosphide”, Phys. Rev. Lett. **18**, 122 (1967).

[104] D. C. Reynolds and T. C. Collins, “Excited terminal states of a bound exciton-donor complex in ZnO”, Physical Review **185**, 1099 (1969).

[105] D. C. Reynolds, D. C. Look, B. Jogai, C. W. Litton, T. C. Collins, W. Harsch, and G. Cantwell, “Neutral-donor-bound-exciton complexes in ZnO crystals”, Phys. Rev. B **57**, 12 151 (1998).

[106] M. Engineer and N. Tzoar, “Polaron bound in a coulomb potential”, Phys. Rev. B **8**, 702 (1973).

[107] J. Sak, “Perturbation theory for a bound polaron”, Phys. Rev. B **3**, 3356 (1971).

[108] D. M. Larsen, “Approximations for the bound-polaron problem”, Phys. Rev. B **9**, 823 (1973).

[109] R. Sauer and K. Thonke, “Donor related exciton luminescence in wide-bandgap semiconductors: Diamond, zinc oxide, and gallium nitride”, Optics of Semiconductors and Their Nanostructures (Editors: H. Kalt and M. Hetterich, Springer) p. 73 (2004).

[110] D. G. Thomas and J. J. Hopfield, “Bound exciton complexes”, Phys. Rev. Lett. **7**, 316 (1961).

[111] P. Loose, M. Rosenzweig, and M. Wöhlecke, “Zeeman effect of bound exciton complexes in ZnO”, Phys. Stat. Sol. (b) **75**, 137 (1976).

[112] G. Blattner, C. Klingshirn, R. Helbig, and R. Meinl, “The influence of a magnetic field on the ground and excited states of bound exciton complexes in ZnO”, Phys. Stat. Sol. (b) **107**, 105 (1981).

[113] J. Gutowski, N. Presser, and I. Broser, “Acceptor-exciton complexes in ZnO: A comprehensive analysis of their electronic states by high-resolution magnetooptics and excitation spectroscopy”, Phys. Rev. B **38**, 9746 (1988).

[114] H. M. Manasevit, “Single-crystal gallium arsenide on insulating substrates”, Appl. Phys. Lett. **12**, 156 (1968).

[115] W. Richter, “Physics of metal organic chemical vapor deposition”, Festkörperprobleme XXVI, Vieweg & Sohn, Wiesbaden (1986).

[116] G. Stringfellow, “Organometallic vapor-phase epitaxy: Theory and Practice”, Academic Press, San Diego (1989).

[117] P. C. Zalm, “Quantitative sputtering”, Surf. Interface Anal. **11** (1988).

[118] W. O. Hofer, R. Behrisch, and K. Wittmaack, “Angular, energy, and mass distribution of sputtered particles”, Sputtering by Particle Bombardment, Vol. III, Springer-Verlag, Berlin (1991).

[119] S. M. Rossnagel, “Sputter deposition for semiconductor manufacturing”, IBM J. Res. Develop. **43**, 163 (1999).

[120] B. Chapman, “Glow discharge processes”, John Wiley & Sons, Inc., New York p. 150 (1980).

[121] S. H. Bae, S. Y. Lee, H. Y. Kim, and S. Im, “Effects of post-annealing treatment on the light emission properties in ZnO thin films on Si”, Opt. Materials **17**, 327 (2001).

[122] X. Xu, C. Guo, Z. Qi, H. Liu, J. Xu, *et al.*, “Annealing effect for surface morphology and luminescence of ZnO film on silicon”, Chem. Phys. Lett. **364**, 57 (2002).

[123] S.-Y. Chu, W. Water, and J.-T. Liaw, “Influence of postdeposition annealing on the properties of ZnO films prepared by RF magnetron sputtering”, J. Europ. Cer. Soc. **23**, 1593 (2003).

[124] S.-H. Jeong, J.-K. Kim, and B.-T. Lee, “Effects of growth conditions on the emission properties of ZnO films prepared on Si(100) by RF magnetron sputtering”, J. Phys. D: Appl. Phys. **36**, 2017 (2003).

[125] J. Wang, G. Du, Y. Zhang, B. Zhao, X. Yang, and D. Liu, “Luminescence properties of ZnO films annealed in growth ambient and oxygen”, J. Cryst. Growth **263**, 269 (2004).

[126] B. Liesert, “Photoluminescence and optical double resonance studies of selected defects in electronic materials”, Academic Press, London (1992).

[127] S. Perkowitz, “Optical characterization of semiconductors: Infrared, raman, and photoluminescence spectroscopy”, Academic Press, London (1993).

[128] D. B. Holt, B. G. Yacobi, and D. C. Joy, "Cathodoluminescence microcharacterization of semiconductors", SEM Microcharacterization of Semiconductors, Academic Press, London p. 373 (1989).

[129] B. G. Yacobi and D. B. Holt, "Cathodoluminescence microscopy of inorganic solids", Plenum Press, New York and London (1990).

[130] J. W. Steeds, "Cathodoluminescence", Encyclopedia of Applied Physics **3**, 121 (1992).

[131] C. R. Brundle, C. A. E. Jr., and S. Wilson, "Encyclopedia of materials characterization", Butterworth-Heinemann (1992).

[132] J. I. Goldstein, D. E. Newbury, P. Echlin, D. C. Joy, J. A. D. Roming, *et al.*, "Scanning electron microscopy and microanalysis", Plenum Press, New York and London, second edition (1992).

[133] K. Kanaya and S. Okayama, "Penetration and energy-loss theory of electrons in solid targets", J. Phys. D **5**, 43 (1972).

[134] H. K. Ko, Y. F. Chen, S. K. Hong, H. Wenisch, T. Yao, and D. C. Look, "Ga-doped ZnO films grown on GaN templates by plasma-assisted molecular-beam epitaxy", Appl. Phys. Lett. **77**, 3761 (2000).

[135] M. Strassburg, A. Rodina, M. Dworzak, U. Haboeck, I. L. Krestnikov, *et al.*, "Identification of bound exciton complexes in ZnO", Phys. Stat. Sol. (b) **241**, 607 (2004).

[136] D. G. Thomas and J. J. Hopfield, "Optical properties of bound exciton complexes in cadmium sulfide", Physical Review **128**, 2135 (1962).

[137] D. Block, A. Herve, and R. T. Cox, "Optically detected magnetic resonance and optically detected ENDOR of shallow indium donors in ZnO", Phys. Rev. B **25**, 6049 (1982).

[138] H. Alves, D. Pfisterer, A. Zeuner, T. Riemann, J. Christen, D. M. Hofmann, and B. K. Meyer, "Optical investigations on excitons bound to impurities and dislocations in ZnO", Opt. Materials **23**, 33 (2003).

[139] J. M. Calleja and M. Cardona, "Resonant Raman scattering in ZnO", Phys. Rev. B **16**, 3753 (1977).

[140] F. Decremps, J. Pellicer-Porres, A. M. Saitta, J.-C. Chervin, and A. Polian, "High-pressure raman spectroscopy study of wurtzite ZnO", Phys. Rev. B **65**, 092 101 (2002).

[141] N. Ashkenov, B. N. Mbenkum, C. Bundesmann, V. Riede, M. Lorenz, *et al.*, “Infrared dielectric functions and phonon modes of high-quality ZnO films”, J. Appl. Phys. **93**, 126 (2003).

[142] F. Bertram, S. Giemsch, J. Christen, A. Dadgar, A. Krost, M. Wagner, and A. Hoffmann, “Direct observation of As-related (e, A^0)-emission in ZnO”, 12th internation conference on II-VI compounds (2005).

[143] P. J. Dean, “Comparison of MOCVD-grown with conventional II-VI materials parameters for EL thin films”, Phys. Stat. Sol. (a) **81**, 625 (1984).

[144] M. Kutrowski, T. Wojtowicz, G. Cywinski, L. V. Titova, E. Martin, *et al.*, “Observation of photoluminescence related to Lomer-Cottrell-like dislocations in ZnSe epilayers grown on in situ cleaved (110) GaAs surfaces”, J. Appl. Phys. **97**, 013 519 (2005).

[145] A. Naumov, K. Wolf, T. Reisinger, H. Stanzl, and W. Gebhardt, “Luminescence due to lattice-mismatch defects in ZnTe layers grown by metalorganic vapor phase epitaxy”, J. Appl. Phys. **73**, 2581 (1993).

[146] S. Fujii, T. Terada, Y. Fujita, and T. Iuchi, “New deep-level photoluminescence bands of homoepitaxial CdTe films grown by metalorganic chemical vapor deposition”, Jpn. J. Appl. Phys. **28**, 1712 (1989).

[147] A. Hoffmann, J. Christen, and J. Gutowski, “Cathodoluminescence wavelength imaging for spatial mapping of excitons bound to dislocations and structural defects in CdS”, Advanced Materials for Optics and Electronics **1**, 25 (1992).

[148] J. Gutowski and A. Hoffmann, “Magneto-optics of excitons bound to dislocations in CdS”, Materials Science Forum **38**, 1391 (1989).

[149] S. Fischer, G. Steude, D. M. Hofmann, F. Kurth, F. Anders, *et al.*, “On the nature of the 3.41 eV luminescence in hexagonal GaN”, J. Cryst. Growth **189**, 556 (1998).

[150] Y. T. Rebane and Y. G. Shreter, “Polycrystalline semiconductors II”, Springer Proceedings in Physics 54, Editors: J. H. Werner and H. P. Strunk p. 28 (1991).

[151] J. W. Steeds, J. L. Batstone, Y. T. Rebane, and Y. G. Shreter, “Polycrystalline semiconductors II”, Springer Proceedings in Physics 54, Editors: J. H. Werner and H. P. Strunk p. 45 (1991).

[152] Y. T. Rebane, “Gauge properties of mathbfk $\cdot$ **p** Hamiltonians for crystals with linear topological defects”, Phys. Rev. B **52**, 1590 (1995).

[153] Y. T. Rebane and J. W. Steeds, “Topological interaction of coulombic impurity centers with dislocations in semiconductors”, Phys. Rev. Lett. **75**, 3716 (1995).

[154] U. Hilpert, “Defektinduzierte optische und elektronische Eigenschaften von II-VI Halbleiterheterostrukturen (german)”, PhD Thesis (2002).

[155] F. Bertram, D. Forster, J. Christen, N. Oleynik, A. Dadgar, and A. Krost, “Direct evidence for selective impurity incorporation at the crystal domain boundaries in epitaxial ZnO layers”, Appl. Phys. Lett. **85**, 1976 (2004).

[156] H. J. Fan, R. Scholz, M. Zacharias, U. Gösele, F. Bertram, D. Forster, and J. Christen, “Local luminescence of ZnO nanowire-covered surface: A cathodoluminescence microscopy study”, Appl. Phys. Lett. **86**, 023 113 (2005).

[157] M. Lorenz, J. Lenzner, E. M. Kaidashev, H. Hochmuth, and M. Grundmann, “Cathodoluminescence of selected single ZnO nanowires on sapphire”, Ann. Phys. (Leipzig) **13**, 39 (2004).

[158] A. C. Tuan, J. D. Bryan, A. B. Pakhomov, V. Shitthanandan, S. Thevuthasan, *et al.*, “Epitaxial growth and properties of cobalt-doped ZnO on $\alpha - \mathrm{Al_2O_3}$ single-crystal substrates”, Phys. Rev. B **70**, 054 424 (2004).

[159] Z. Jin, M. Murakami, T. Fukumura, Y. Matsumoto, A. Ohtomo, M. Kawasaki, and H. Koinuma, “Combinatorial laser MBE synthesis of 3d ion doped epitaxial ZnO thin films”, J. Cryst. Growth **214**, 55 (2000).

[160] E. Burstein, “Anomalous absorption limit in InSb”, Physical Review **93**, 632 (1954).

[161] T. S. Moss, “The interpretation of the properties of indium antimonide”, Proc. Phys. Soc. (London) **67**, 775 (1954).

[162] A. P. Roth, J. B. Webb, and D. F. Williams, “Absorption edge shift in ZnO thin films at high carrier densities”, Solid State Commun. **39**, 1269 (1981).

[163] M. Zhang, L. M. Cao, F. F. Xu, Y. Bando, and W. K. Wang, “Structural properties of magnetron sputtered ZnO films with incorporated iron”, Thin Solid Films **406**, 40 (2002).

[164] Q. P. Wang, D. H. Zhang, Z. Y. Xue, and X. J. Zhang, “Mechanisms of green emission from ZnO films prepared by rf magnetron sputtering”, Opt. Materials **26**, 23 (2004).

[165] N. Fujimura, T. Nishihara, S. Goto, J. Xu, and T. Ito, “Control of preferred orientation for $\mathrm{ZnO_x}$ films: Control of self-texture”, J. Cryst. Growth **130**, 269 (1993).

[166] "JCPDS file 36-1451", International Center for Diffraction Data (1997).

[167] J. H. Jou, M. Y. Han, and D. J. Cheng, "Substrate dependent internal stress in sputtered zinc oxide thin films", J. Appl. Phys. **71**, 4333 (1992).

[168] V. Gupta and A. Mansingh, "Influence of postdeposition annealing on structural and optical properties of sputtered zinc oxide film", J. Appl. Phys. **80**, 1063 (1996).

[169] A. S. Risbud, N. A. Spaldin, Z. Q. Chen, S. Stemmer, and R. Seshadri, "Magnetism in polycrystalline cobalt-substituted zinc oxide", Phys. Rev. B **68**, 205 202 (2003).

[170] P. Koidl, "Optical absorption of Co^{2+} in ZnO", Phys. Rev. B **15**, 2493 (1977).

[171] H.-J. Schulz and M. Thiede, "Optical spectroscopy of $3d^7$ and $3d^8$ impurity configurations in wide-gap semiconductor (ZnO:Co,Ni,Cu)", Phys. Rev. B **35**, 18 (1987).

[172] S. Ramachandran, A. Tiwari, and J. Narayan, "$Zn_{0.9}Co_{0.1}O$-based diluted magnetic semiconducting thin films", Appl. Phys. Lett. **84**, 5255 (2004).

[173] M. Schilling, R. Helbig, and G. Pensl, "Bound exciton luminescence of Ar- and Al-implanted ZnO", J. Luminescence **33**, 201 (1985).

Erklärung

Die selbständige und eigenhändige Anfertigung
versichere ich an Eides statt.

Berlin, den 18. August 2005

Markus Raphael Wagner